UNIVERSITY OF CANTERBURY

# Shape Optimisation of a 200 mm Axial Fan for Aeroacoustic Noise

*Author:*
Ryan MCKAY

*Supervisor:*
Dr. John PEARSE

*A thesis submitted in fulfilment of the requirements for the degree of Master of Engineering*

*in the*

Acoustics Research Group
Department of Mechanical Engineering

April 29, 2016

# Abstract

Axial flow fans are often the largest contributor to the noise emitted from commercial refrigerator systems. This has driven the demand for quieter, yet higher performance axial flow fans. Turbulent fluid motion and aerodynamic forces interacting with the fan blades generate noise as the fan rotates. The aerodynamic noise emitted from a fan can be modelled with varying degrees of accuracy which are typically proportional to the computational cost. Application of a fan performance model to an optimisation algorithm can be used to develop new and higher performing fan blades. However, there is currently no rapid method to generate an optimal fan design of specified performance.

The method developed in this project was experimentally validated and shown to be able to predict the flow rate accurately; however, the fan noise prediction was unsuccessful. Noise source identification showed that the dominant fan noise source was incident turbulence noise which was neglected in the aeroacoustic modelling and explains the poor noise prediction. Knowing the dominant noise source allows for future modelling to include all relevant physics which will allow for more accurate modelling that will increase the performance of axial flow fans and reduce refrigeration noise. This study also showed that fans with aerofoil blade shapes have superior performance to fans with cambered plate blades, which are commonly used in commercial refrigerators.

# Acknowledgements

I would like to express my gratitude to my supervisor Dr. John Pearse. Throughout this course of study he has allowed this work to be my own. His support and guidance has been much appreciated.

I would like to thank Dr. Brian Donohue for his open door (if being on the other side of a low partition counts). His willingness to share his vast experience and knowledge has been invaluable.

I would also like to thank the various technical support during this project: Julian for his electronics expertise, often at short notice; Dave for his construction of the test rig and making last minute changes; Garry for patience and guidance while I was in the workshop and Dave for his help 3D printing fans.

To my partner, Sophia: Thank you for your support, encouragement and superior grammatical skills. Your company on the late nights while I was testing fans made it much more bearable.

And finally, to my mum: Without your support, this would not have been possible.

# Contents

# List of Figures

All images were created by the author unless otherwise stated.

# List of Tables

# List of Abbreviations

| | |
|---|---|
| **AOA** | **A**ngle **O**f **A**ttack |
| **AR** | **A**spect **R**atio |
| **BEMT** | **B**lade **E**lement **M**omentum **T**heory |
| **BET** | **B**lade **E**lement **T**heory |
| **BPF** | **B**lade **P**assing **F**requency |
| **BPM** | **B**rooks **P**ope **M**arcolini (aeroacoustic model) |
| **CAA** | **C**omputational **A**ero**a**coustics |
| **CFD** | **C**omputational **F**luid **D**ynamics |
| **GA** | **G**enetic **A**lgorithm |
| **ISO** | **I**nternational **S**tandards **O**rganisation |
| **IT** | **I**ncident **T**urbulence |
| **LBL-VS** | **L**aminar **B**oundary **L**ayer - **V**ortex **S**hedding |
| **LES** | **L**arge **E**ddy **S**imulation |
| **MOPSO** | **M**ulti **O**bjective **P**article **S**warm **O**ptimisation |
| **NACA** | **N**ational **A**dvisory **C**ommittee for **A**eronautics |
| **NI** | **N**ational **I**nstruments |
| **OSWL** | **O**verall **S**ound Power **L**evel |
| **PSO** | **P**article **S**warm **O**ptimisation |
| **SPL** | **S**ound **P**ressure **L**evel |
| **S-S** | **S**eparation - **S**tall |
| **SWL** | **S**ound Power **L**evel |
| **TE** | **T**railing **E**dge |
| **TBL-TE** | **T**urbulent **B**oundary **L**ayer - **T**railing **E**dge |
| **TBL-VS** | **T**urbulent **B**oundary **L**ayer - **V**ortex **S**hedding |
| **T-S** | **T**ollmien-**S**chlochting |

# Physical Constants

| | |
|---|---|
| Speed of sound in air | $c = 343\,\mathrm{m\,s^{-1}}$ |

# Nomenclature

| | | |
|---|---|---|
| $A_w$ | shroud expansion factor | |
| $A$ | area | $m^2$ |
| $B$ | number of blades | |
| $B_i$ | control points | |
| $c$ | chord length | m |
| $C_1$ | PSO self confidence factor | |
| $C_2$ | PSO swarm confidence factor | |
| $C_D$ | drag coefficient | |
| $C_L$ | lift coefficient | |
| $d$ | distance | m |
| $D$ | drag force | N |
| $D_h$ | directionality function | |
| $\mathcal{F}$ | feasible region | |
| $f$ | frequency | Hz |
| $F$ | force | N |
| $H$ | boundary layer shape factor | |
| $H_k$ | kinematic shape parameter | |
| $I_{turb}$ | turbulence intensity | |
| $k$ | degree of curvature | |
| $\hat{k}$ | wave number | $m^{-1}$ |
| $K_2$ | room correction factor | dB |
| $L$ | lift force | N |
| $L_p$ | sound pressure level | dB |
| $L_w$ | sound power level | dB |
| $\dot{m}$ | mass flow rate | $kg\,s^{-1}$ |
| $Ma$ | Mach number | |
| $n$ | number of control points | |
| $N$ | rotational velocity | rpm |
| $N_{i,k}(t)$ | basis function | |
| $\mathcal{P}$ | Pareto optimal set | |
| $p$ | pressure | $N\,m^{-2}$ |
| $P$ | power | $J\,s^{-1}$ |
| $P_i$ | PSO best particle solution | |
| $P_G$ | PSO global best solution | |
| $PF$ | Pareto front | |
| $Q$ | flow rate | $m^3\,h^{-1}$ |
| $r$ | distance from hub to element | m |
| $r_e$ | reference distance from sound source | m |
| $R$ | radius of a fan | m |
| $R_{xx}$ | Autocorrelation function | |
| $S$ | surface area | $m^2$ |
| $S(t)$ | b-spline curve | |

| | | |
|---|---|---|
| $t$ | time | s |
| $t$ | knots | |
| $t_e$ | trailing edge thickness | m |
| $T$ | thrust | N |
| $T$ | normalised thickness of cambered plate aerofoil | |
| $T_{i,j}$ | Lighthill stress tensor | |
| $\vec{T}$ | knot vector | |
| $U$ | total velocity | $\mathrm{m\,s^{-1}}$ |
| $v_{i,t}$ | PSO velocity | |
| $v_i$ | velocity in $i$ | $\mathrm{m\,s^{-1}}$ |
| $w$ | PSO inertia factor | |
| $W$ | work | J |
| $x_{i,t}$ | PSO position | |
| $\alpha$ | aerodynamic angle of attack | $^\circ$ |
| $\delta$ | boundary layer thickness | mm |
| $\delta_2$ | boundary layer momentum thickness | mm |
| $\delta^\star$ | boundary layer displacement thickness | mm |
| $\Delta L$ | SWL difference at $f$ | dB |
| $\Delta T$ | period used in the calculation of $R_{xx}$ | s |
| $\eta$ | efficiency | % |
| $\theta$ | geometric angle of attack | $^\circ$ |
| $\lambda$ | wavelength | m |
| $\Lambda$ | turbulence integral length | m |
| $\rho$ | density | $\mathrm{kg\,m^{-3}}$ |
| $\sigma$ | rotor solidity | |
| $\tau$ | torque | N m |
| $\tau$ | lag time | s |
| $\phi$ | angle of induced flow | $^\circ$ |
| $\omega$ | angular frequency | $\mathrm{rad\,s^{-1}}$ |

# Chapter 1

# Introduction

Axial flow fans are commonly used as air moving devices in ventilation and refrigeration systems in many residential, commercial and industrial environments. The primary purpose of a fan is to meet prescribed flow parameters, such as flow rate or total fan pressure, for a specific application with consideration given to the efficiency of the fan. An often secondary, but increasingly common, consideration in the selection of a fan is the aeroacoustic noise generated. Noise as a selection criteria for fans is being driven by people's awareness of noise and demand for quieter environments. This is compounded by the increasing demand for greater fan performance which typically comes at the detriment of noise.

Refrigerator manufacturers are subject to increasing pressure from clients to reduce the noise of their refrigerators. In a commercial refrigerator system, the dominant noise source is usually the fans. Typically, commercial refrigerators have two fans: a condenser fan and an evaporator fan. The airflow from the fans is required for efficient heat transfer by the heat exchangers. Axial flow fans are used in refrigerators, which require high flow rates for cooling but low pressures. The size of componentry in a small commercial refrigerator means that 200 mm fans are typically utilised.

Early research into fan noise was focused on propeller-driven aircraft as the demand for increased thrust began to generate significant noise. With the widespread introduction of civil aircraft in the 1950s, a demand for acoustically designed propellers became apparent [1]. Although on a very different scale, many of the principles used to analyse early civil aircraft are applicable to the analysis of refrigeration fans.

There currently is no rapid method to design a fan suitable for a specific application. The purpose of this work is to develop a method that can rapidly generate a quiet fan for prescribed flow rates and pressures. A test rig was developed to identify the dominant noise sources of a fan and used to identify noise sources of refrigerator fans.

The major body of this work is dedicated to developing a rapid method to predict the aerodynamic and aeroacoustic performance of a fan similar to the methods used by [2], [3] . De Gennaro and Kuehnelt [2] compared their modelled results to experimental results with good correlation; however, they did not use their model for optimisation. Rodrigues [3] used a similar model and applied it to wind turbines with an optimisation process; however, this work did not use any experimental validation. The model in this work was applied with an optimisation algorithm with the intent of developing better blade shapes for axial flow fans. Although the optimisation method was not explicitly designed for refrigerators, the verification of the model and optimisation process was carried out using 200 mm fans to validate the applicability to refrigerator fan design.

The goal of this project was to use a model and optimisation method to develop an axial flow fan with the following attributes at an operating speed of 1800 rpm:

- Airflow rate of at least 550 $m^3\,h^{-1}$ at 25 Pa
- Airflow rate of at least 680 $m^3\,h^{-1}$ at 0 Pa
- Minimum static pressure at stall is 40 Pa
- Less noise than commonly available commercial refrigerator fans

A more desirable fan would have higher flow rates than those above and higher efficiencies than a commonly available refrigerator fan.

A literature review is presented in Chapter 2 of common noise sources and methods to reduce them. Chapter 3 presents the aerodynamic model which is built upon in Chapter 4 which introduces the aeroacoustic model. Chapter 5 furthers this work with the introduction of an optimisation algorithm and the method used to link the aerodynamic and aeroacoustic models to the optimisation process. Chapter 6 presents the results of the optimisation with five different blade shapes, of which three were used for validation purposes. Chapter 7 contains the development of a testing procedure along with the associated experimental methodology. Chapter 8 presents the experimental results of the developed fans with additional work on the identification of noise sources. Conclusions and discussion of future work are presented in Chapter 9.

# Chapter 2

# Literature Review

## 2.1 Fundamentals of aeroacoustics

Although Rayleigh and Strouhal performed some early aeroacoustic work, Lighthill [1] was the first to propose a description for of aerodynamically generated sound. Lighthill rearranged the fundamental equations of an aerodynamic flow to the form of a wave equation

$$\frac{\partial^2 \rho}{\partial t^2} - c^2 \nabla^2 \rho = \frac{\partial^2 T_{ij}}{\partial x_i \partial x_j}, \tag{2.1}$$

where $T_{ij}$ is the Lighthill stress tensor defined by

$$T_{ij} = \rho v_i v_j + p_{ij} - \alpha_0^2 \rho \delta_{ij}, \tag{2.2}$$

or, for small Mach numbers, by

$$T_{ij} \approx \rho_0 v_i v_j. \tag{2.3}$$

Although important in the development of aeroacoustical theory, Lighthill's equations were incomplete. Various developments of this theory have been proposed such as [4]–[6]; however, the most widely used of these is the Ffowcs-Williams and Hawkings equation [7] :

$$\Big(\frac{\partial^2}{\partial t^2} - c^2 \nabla^2\Big)\overline{\rho - \rho_0} = \frac{\partial^2 \overline{T_{ij}}}{\partial x_i \partial x_j} - \frac{\partial}{\partial x_i}\Big(p_{ij}\delta(f)\frac{\partial f}{\partial x_j}\Big) + \frac{\partial}{\partial t}\Big(\rho_0 v_i \delta(f)\frac{\partial f}{\partial x_i}\Big), \tag{2.4}$$

where $c$ is the speed of sound in a uniform medium, $f$ is the external force per unit volume acting on the fluid, $p_{ij}$ is the compressive stress tensor in the $x_{i,j}$ direction, $\rho$ is the density of the medium and the overbar implies that the variable regarded as a generalised function valid throughout the volume of the fluid.

The left side of equation 2.4 is the homogeneous acoustic wave equation. The right side is the source term consisting of volume distributions representing various possible

noise sources in the fluid. The first source term is the distribution of acoustic quadruples throughout the region exterior to the surfaces (the focus of Lighthill's work). The second source term is the surface distributions of acoustic dipoles (the focus of Curle's work). The third source term is the surface distributions of sources representing the volume displacement effect, which is essentially monopole.

It is known [8] that monopoles have a higher acoustic efficiency than dipoles, which respectively have a higher acoustic efficiency than quadrupoles. This carries the assumption that the wavelengths of the sound generated are small relative to the flow distribution, which is typically true for airflows of low Mach number and is the case for the axial fans of interest. Additionally, the sound power of monopole sources varies approximately as $v^4$, dipoles as $v^6$ and quadrupoles as $v^8$ [9].

## 2.2 Noise generation mechanisms in axial flow fans

The aerodynamic noise generated by fans arises from the turbulence generated by the fan and its associated components. Early research into fan noise had a focus on the generation of tonal noise at blade passing frequencies. More recent fan noise research has provided insight into the generation of broadband noise which originate from randomly fluctuating forces. The following overview on noise generation mechanisms of axial flow fans considers tonal and broadband noise mechanisms separately.

### 2.2.1 Tonal noise

Tonal fan noise is generated by periodic fluctuations in aerodynamic forces. The periodic nature of these forces results in the generation of discrete acoustic tones. The earliest research into tonal noise was that of Gutin [10] who investigated the periodic disturbances to air caused by a rotating propeller. The frequency of this disturbance is called the blade passing frequency (BPF) and is defined as

$$BPF = \frac{N}{60}B, \tag{2.5}$$

where $N$ is the rotational speed in rpm and $B$ is the number of blades.

In some of the earliest work on propeller noise, Gutin developed equations that give an order of magnitude prediction of the sound power and the directivity of the sound generated by a propeller. Gutin's method involved replacing the periodic forces of each propeller with dipole sources and relating the acoustic power generated to the thrust, torque and rotational speed of the propeller. Gutin's theory is not applicable to fans as the assumption of low blade numbers, which is a result of the theory not considering how blades interact with each other, is violated. The close spacing of blades

in a fan makes interaction between blade pressure fields and wakes more likely than in a propeller [8].

Another key difference between propellers and refrigerator fans is that fans typically have shrouds and support structures which introduce an additional noise generation mechanisms. A common interaction effect of fans is the rotor-stator interaction which can cause a periodic fluctuating force on the blade. In this interaction, the stators create a velocity difference at the inlet on the fan's blades. The variation in velocity causes a periodic variation in lift forces on the blade, generating a tonal noise. In the case of refrigerator fans, stators are typically not used; however, the physical explanation for rotor-stator interaction extends to any object in the flow that causes a fluctuation in velocity, such as the fan support structure. In summary, propeller noise periodically excites an elemental area of air; whereas, rotor-stator interaction causes a periodic variation in velocity leading to varying lift forces.

Mugridge and Morfey [11] showed for axial flow fans if $\sigma C_L^2 \sim 1$, then quadrupole noise can be significant, However, if $\sigma C_L^2 \ll 1$, then dipole noise dominates. In the previous equations, $\sigma$ is the fan solidity, and $C_L$ is the lift coefficient of the blade. The dipole sources are created by propeller noise; whereas, the quadrupole sources are from the fluctuating velocity fields. For the case of refrigerator fans, there is typically a moderate degree of rotor solidity and moderate lift coefficients; hence, quadrupole noise is expected to dominate.

An additional noise source discussed by Mugridge and Morfey [11] is the interaction effect of adjacent blades, which induce velocity fluctuations on the potential flow of the following blades, in turn, inducing varying lift forces and noise. Due to the regular nature of the forces generated by the blade interaction, a tonal noise results.

A potentially strong source of noise comes from vortex shedding [12] caused by pressure fluctuations in the laminar boundary layer. The fluctuations occur due to a streamwise instability that occurs as the laminar boundary layer transitions to a turbulent boundary layer called Tollmien-Schlochting waves (T-S waves). In the situation where one or both sides of the blade do not transition to turbulence before the trailing edge, the trailing edge will be in the region where T-S waves are present, which results in scattering at the trailing edge and, hence, generation of sound. The acoustic waves then travel upstream to the point of instability on the blade. If the acoustic waves and the T-S waves are in phase, a feedback loop occurs that creates resonance and generates a tonal noise.

Tip vortices are a common broadband noise source; however when a periodic variance in the vortex generation occurs, tip vortices can generate a tonal noise [11], [13]. A periodic variance in the tip vortices can be caused by a circumferential variation in the rotor tip clearance resulting from poor circularity of the shroud or eccentric mounting

of the fan. The tones generated by the variation in tip clearance will be at the blade passing frequency.

### 2.2.2 Broadband noise

Whereas tonal noise is the generation of sound through periodically fluctuating forces, broadband noise originates from randomly fluctuating forces. Sharland [8] proposed three mechanisms through which broadband noise can be generated: turbulent boundary layers, vortex shedding and turbulent inlet flow. The turbulent boundary layer on the surface of the fan blades generates randomly fluctuating forces, which act as a surface of noise.

Although it was discussed in section 2.2.1 that vortex shedding under certain circumstances could produce a tonal noise, vortex shedding can also generate broadband noise. As a fan rotates, random fluctuations from vortices being shed at the blade's trailing edge will produce local variations in lift force. This generates irregular lift variations and, hence, broadband noise. The two circumstances where vortex shedding generates a tonal noise are when a feedback loop is created, as discussed in section 2.2.1, or when the fan blade is at a high angle of incidence. In the case of high angles of incidence, periodic vortex shedding, such as a Karman street, can occur.

The third noise source discussed by Sharland occurs due to turbulence at the intake of the fan. This mechanism is caused by an upstream disturbance which induces turbulence in the inflow. The irregular inflow velocity causes random lift fluctuations which generate broadband noise. Turbulence requires spatial and temporal variations; hence, it differs from effects like rotor-stator interaction which generate periodically varying lift fluctuations.

The generation of vortices at the blade tip is another broadband noise source in axial flow fans. As the fluid passes over the blades, a pressure differential is formed which causes the flow to roll up in a vortex. The vortex then has the potential to interact with the trailing edge of that blade or with a following blade [14]. Due to the random nature of the vorticity, broadband noise is generated. A secondary flow effect is the generation of a blade-passage vortex by the deflection of the flow streamlines within the annulus wall boundary layer [11]. The blade-passage vortex has an opposing effect on the tip vortex, which Mugridge and Morfey suggested allows for the tip clearance to be controlled to provide minimal sound generation. Their suggested value for tip clearance is 0.05 of the blade chord.

Ffowcs Williams and Hall [15] modelled a turbulent eddy as a quadrupole source near the edge of a half plane. The effect of trailing edge scattering is a potentially strong noise source, with the sound intensity having a dependence on $v^5$ and $d^3$ where $d$ is the distance from the eddy to the edge. This reinforces the previously discussed notion

that velocity has a strong effect on noise; however, it is also important to recognise that an eddy's proximity to an edge has a strong effect on the noise. Ffowcs Williams and Hall also stated that smaller surfaces will be dominated by edge noise; however, surfaces with lengths normal to the edge larger than the critical size of $(\frac{8}{\pi^5})Ma^{-2}\lambda$ will be essentially unaffected by edge noise. Because of the very strong dependence on the speed of the fan, the critical size is typically larger than the chord of a 200mm axial flow fan. Hence, trailing edge noise is likely the dominant self-noise source in a 200 mm axial flow fan. This theory has been shown experimentally to give good directivity results and order of magnitude intensity levels [16].

When blades have high angles of attack or the fan is under a high load, the boundary layer can separate from the fan blade which results in stall. Fans with stalled flows are known to be strong generators of broadband noise [8]. The degree of stall effects the noise generated; as the flow starts to separate, the dominant noise is emitted from the trailing edge. However, under severe stall, the noise is emitted from the entire chord [17].

## 2.3 Management of noise mechanisms

There are many complex noise generation mechanisms in axial flow fans, as discussed above. This section continues the discussion of axial flow fans by looking at methods to reduce the noise generated by axial flow fans through modifications to different components of the fan assembly.

### 2.3.1 Impeller noise

The strong dependence of sound power on the velocity of fans means that a small reduction in fan speed can have moderate reductions in the sound power of the fan. This technique was utilised in the early noise reduction of turbojet engines [18]. Reducing the velocity of a fan results in lower flow rates; however, correct design of the system or redesign of the fan could make this a plausible option for noise reduction. For example, by increasing the efficiency of the fan, equivalent flow rates could be achieved at lower speeds. Alternatively, the system in which the fan is being installed could be designed to operate with lower flow rates, for example, by increasing the efficiency of a heat exchanger.

Ffowcs Williams and Hall [15] proposed that the noise from a sharp edge surface could be reduced by giving the blade a swept wing characteristic. They proposed that a propeller with greater curvature in the span-wise direction would generate less noise than one with a radial span-wise direction. Additional studies have shown experimentally

that forward swept blades can reduce the noise produced by fans by up to 10 dBA, but backward swept blades can increase noise [19], [20].

Boundary layer tripping can be used to prevent separation and laminar vortex shedding at the trailing edge. A method of tripping the boundary layer in fans is to use a serrated leading edge [14] which creates a turbulent boundary layer before the trailing edge which significantly reduces the vortex shedding. Longhouse states that this provides a 20-30 dB reduction in broadband noise; however, his investigations were on 400 mm axial flow fans operating at speeds up to 6000 rpm. It has been shown in [21] that 200 mm axial flow fans with leading edge serrations have reduced noise levels. Tripping the boundary layer has the additional benefit of removing one of the conditions required for the acoustic feedback loop discussed previously. Howe [22], [23] proposed that serrations on the trailing edge perform better than leading edge serrations, as leading edge serrations are known to reduce aerodynamic efficiency of fans. Trailing edge serrations are expected to reduce noise by reducing the span-wise length of the trailing edge that contributes to sound generation. Howe estimated that the trailing edge serrations reduce sound levels by up to 8 dB; however, this has not been experimentally validated.

Unevenly spaced blades have been proposed as a method of reducing tonal noise in fans [24], [25]. The dominant tones in axial flow fans are at the BPF and its subsequent harmonics. By unevenly spacing the blades, the noise will be generated over a range of frequencies, instead of just the BPF. Unevenly spaced blades are shown [24], [25] to be more broadband in nature; however, the total sound power is not reduced. Therefore, this method is useful for improving the quality of sound rather than the total sound emitted.

### 2.3.2 Shroud noise

Shrouds are an important component of a fan assembly as they substantially improve the aerodynamic efficiency of the fan. There are also important acoustic properties of shrouds which should be accounted for. The tip clearance between the fan and the shroud is one of the most important properties of the shroud. The shroud reduces the tip vortices generated by the fan with a smaller gap resulting in a weaker tip vortex being generated. This has the dual purpose of reducing noise and improving the aerodynamic efficiency of the fan.

Fukano et al. [13], [26] experimentally investigated the acoustic effects of tip clearance on 600 mm fans at speeds of 1000-2000 rpm. A strong relationship was found between smaller tip clearances and improved acoustic and aerodynamic performance. At the maximum efficiency operating point, reduction in tip size resulted in an increase in efficiency of 7-9% and a reduction in sound power of 3-4dB. Similar increases were found at off-peak efficiency operating conditions. The limit on tip clearance is constrained by

manufacturing tolerances, including the circularity of the shroud as any radial variations in the shroud result in tonal noise generation.

Longhouse [14] proposed the use of rotating shrouds as a method to reduce tip clearance noise without reducing tip clearances. In Longhouse's study, 356 mm diameter fans were used at 3900 rpm which achieved up to 12 dB noise reduction with the addition of a ring-shroud. The addition of the ring-shroud had minimal impact on aerodynamic performance. However, the ring did introduce additional viscous losses; therefore, some reduction in performance can be expected. Longhouse observed that the addition of the ring-shroud moved the minimum noise and peak operating points closer; however, this effect is likely dependent on the fan geometry.

### 2.3.3 Support structure noise

The support structure is required to position and support the fan and motor during operation. A secondary purpose of the support structure is for routing cables to the motor. As discussed in section 2.1, the supports are a source of tonal noise; however, correct design of supports can mitigate this noise generation mechanism.

Huang [27] developed a model of the sound power generated by the interaction between the blades and supports. It was shown that the sound power has a dependence on the fourth power of the number of struts. Although fewer supports will result in a lower sound power, the model considers the interaction between the number of blades and the number of supports and the effects on the harmonic frequency. The model is limited in that it does not consider of the size of the supports. Using only two supports is likely to cause a structural weakness which would require larger supports to provide adequate strength; however, the larger supports are likely to generate more noise.

Fitzgerald and Lauchle [21] modified the shape of the supports to reduce the noise generated. Each of the existing struts was filed into a slim streamline shape to reduce their wake. One of the struts was larger than the others due to a conduit for the electrical wires which was filed down to the same size as the other struts. They introduced an additional four small, hollow aerofoil shaped struts to house the wires without interfering with the fan. Depending on the type of fan used, these simple modifications to the struts provided a 7-17 dB reduction in sound power at the lowest BPF. In some cases the sound power increased for harmonics of the blade passing frequency; however, there was an overall reduction in sound power for all cases.

# Chapter 3

# Aerodynamic Model

The performance of a fan is largely determined by its size, rotational speed and blade characteristics and is measured by flow rate, total fan pressure, power and efficiency. When designing a fan, it is important to be able to predict the fan's performance; this can be done using aerodynamic modelling. Computational fluid dynamics (CFD) is a state of the art method; however, CFD is computationally expensive and implausible for optimisation without supercomputing [28].

This chapter presents a formulation of blade element momentum theory relevant to the design of a fan. Blade element theory (BET) has its origins in the work of William Froude in 1878 with significant extensions by Stefan Drzewiecki between 1892 and 1920. Many further developments were made to BET during the early 20th century; however, the two major developments to the theory were the connection to momentum theory and the Prandtl lifting-line theory [29]. The theory presented below combines BET with momentum theory and is called blade element momentum theory (BEMT). Due to the complete development of this theory, there are many textbooks within the aerospace, fan, helicopter and wind turbine fields that cover this topic. The core resources used in the presentation of this theory are [29]–[31]; however, many alternative sources could be used.

BET makes the assumption that the blade can be discretised into small elements of size $dr$. Each of these elements is assumed to be independent of the other elements and operate as 2D aerofoils whose properties can be calculated from local flow conditions. The total force and torque applied by the rotating blade can be calculated by integrating the elements across the entire blade. BET can be coupled with momentum theory which assumes that the change in pressure and momentum across the fan is caused by the work done by the fan. This allows for the velocities induced by the fan to be calculated.

## 3.1 Momentum theory

Momentum theory was first proposed by Rankine [32] as a method for analysing marine propellers. It treats the fan as an infinitesimally thin actuator disk that creates a pressure increase as shown in Figure 3.1. Momentum theory assumes the flow is one-dimensional, quasi-steady, incompressible and inviscid. Let the control volume

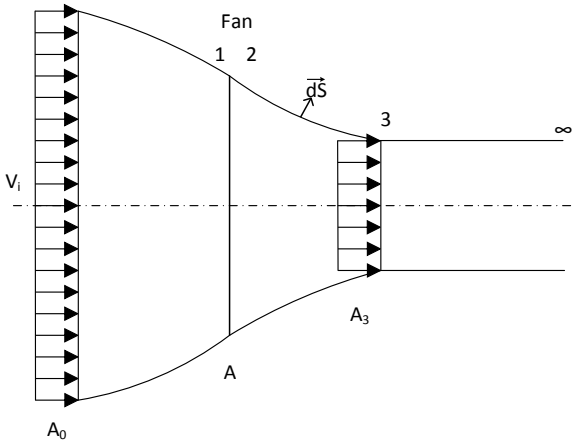


FIGURE 3.1: Flow model for momentum theory analysis of an unducted fan, where $V_i$ is the inlet velocity, $d\vec{S}$ is the outward facing unit normal area vector and $A$ is the cross sectional area.

surrounding the rotor and its wake, as shown in Figure 3.1, have surface area $S$ and the outward facing unit normal area vector, $d\vec{S}$. Applying the conservation of mass to Figure 3.1 gives

$$\iint_S \rho\vec{V} \cdot d\vec{S} = 0, \tag{3.1}$$

where $\vec{V}$ is the local velocity. The continuity equation states that the mass flow into the control volume is equal to the mass exiting the control volume. Similarly, the conservation of momentum can be written as

$$\vec{F} = \iint_S p d\vec{S} + \iint_S (\rho\vec{V} \cdot d\vec{S})\vec{V}. \tag{3.2}$$

The net pressure on the fluid side (the inner region) of the control volume is zero for unconstrained flow. Therefore, the first term of equation 3.2 is zero, thus, simplifying $\vec{F}$ to be equal to the rate of change with time of the fluid momentum across the control surface, S . The final governing equation is the conservation of energy which shows that the work done by the rotor on the fluid results in an increase in kinetic energy of the fluid in the rotor slipstream.

$$W = \iint_S \frac{1}{2}(\rho\vec{V} \cdot d\vec{S})|\vec{V}|^2 \tag{3.3}$$

From these governing equations, the previously stated assumptions can be applied to give more appropriate forms of the equations to the application of fan performance. It is important to note that the inlet flow is quiescent ($v_0 = 0$). The induced velocity at the plane of the fan is defined as $v_i$, and the far field velocity is defined as $v_\infty$. The fan area is defined as $A$.

From equation 3.1 and the assumption of quasi-steady flow, it is known that the mass flow rate within the boundaries of the control volume must be constant.

$$\dot{m} = \iint_2 \rho\vec{V} \cdot d\vec{S} = \iint_\infty \rho\vec{V} \cdot d\vec{S} \tag{3.4}$$

With the assumption of a one dimensional incompressible flow, this reduces to

$$\dot{m} = \rho A_2 v_i = \rho A_\infty v_\infty = \rho A v_i. \tag{3.5}$$

Due to the effect of the shroud, as shown in Figure 3.2, $A_\infty$ cannot easily be determined. Introducing the shroud expansion factor $a_w$, which is defined as $a_w = \frac{v_i}{v_\infty}$, makes estimation of $A_\infty$ possible as $A_\infty = a_\infty A$. Without a shroud or duct, it has been shown that $a_\infty = 0.5$; however, with a shroud or duct, this increases. The shroud expansion factor used in this project is $a_w = 1.25$ as recommended by Leishman [29].

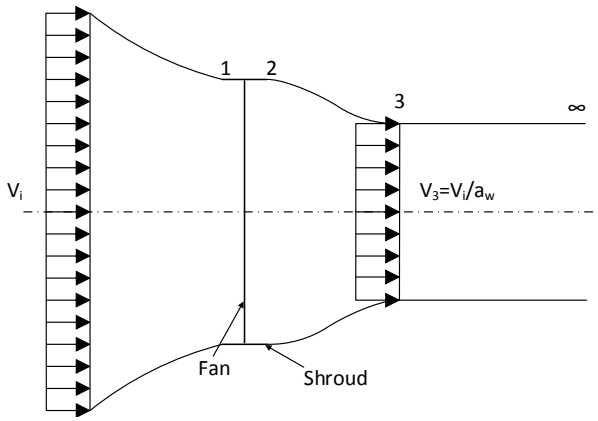


FIGURE 3.2: Flow model for momentum theory analysis of a ducted fan, where $V_3$ is the velocity at point 3, $V_i$ is the velocity at the inlet, and $a_w$ is the shroud expansion factor.

From equation 3.2 and the assumption of quiescent flow at the inlet, the thrust is

$$\vec{T} = -\iint_\infty (\rho\vec{V} \cdot d\vec{S})\vec{V} = -\dot{m}v_\infty. \tag{3.6}$$

Similarly, equation 3.3 yields the following relationship for the work done per unit time (power) of the fan on the fluid.

$$Tv_i = \iint_0 \frac{1}{2}(\rho\vec{V} \cdot d\vec{S})|\vec{V}^2| - \iint_2 \frac{1}{2}(\rho\vec{V} \cdot d\vec{S})|\vec{V}|^2, \tag{3.7}$$

where the first term is zero as the inlet flow is quiescent, hence

$$Tv_i = -\iint_2 \frac{1}{2}(\rho\vec{(V)} \cdot d\vec{S})|\vec{V}|^2 = \frac{1}{2}\dot{m}v_\infty^2. \tag{3.8}$$

Rearranging equations 3.5, 3.7 and 3.8 gives the final result of

$$T = \dot{m}(2v_i) = \frac{1}{a_w}\rho A v_i^2. \tag{3.9}$$

## 3.2 Blade element theory

Blade element theory discretises a blade into many two dimensional elements of size $dr$. Each of these elements is assumed to act as a two dimensional aerofoil that generates aerodynamic forces. Unlike momentum theory, BET uses the blade geometry to estimate aerodynamic performance. The main limitation of BET is that three dimensional effects, such as blade interaction effects or tip effects, are not modelled.

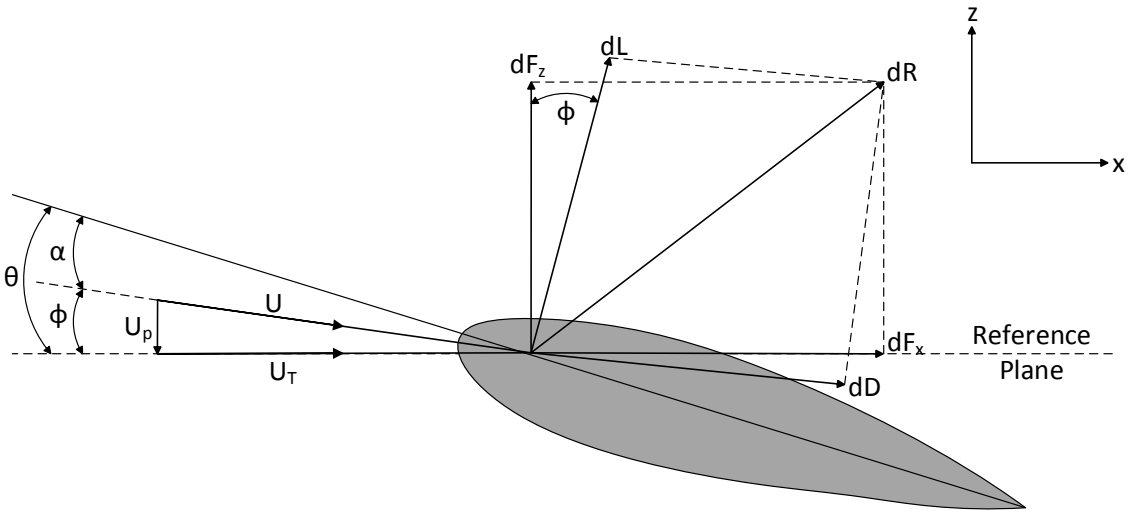


FIGURE 3.3: Incident velocities at a typical blade element. $\theta$ is the geometric angle of attack. $\alpha$ is the aerodynamic angle of attack. $\phi$ is the angle of the flow over the blade. $dF_z$ and $dF_x$ are the forces on the blade element in the $z$ and $x$ directions respectively. $dL$ and $dD$ are the elemental lift and drag forces respectively, and $dR$ is the resultant force on the blade element.

From Figure 3.3, the resultant velocity and inflow angles at a blade element are

$$U = \sqrt{U_T^2 + U_P^2} \tag{3.10}$$

$$\phi = \tan^{-1}\left(\frac{U_P}{U_T}\right). \tag{3.11}$$

If the geometric angle of attack is $\theta$, then the effective angle of attack is

$$\alpha = \theta - \phi = \theta - \tan^{-1}\left(\frac{U_P}{U_T}\right). \tag{3.12}$$

The elemental lift and drag on a blade element are

$$dL = \frac{1}{2}\rho U^2 c C_L dy \tag{3.13a}$$

$$dD = \frac{1}{2}\rho U^2 c C_D dy, \tag{3.13b}$$

where $C_L$ and $C_D$ are the lift and drag coefficients of the two dimensional cross section, respectively, and $c$ is the local blade chord. The lift and drag forces act perpendicular and parallel to the flow velocity, respectively, so the elemental forces defined in the $z$-$x$ coordinate system are

$$dF_z = dL\cos\phi - dD\sin\phi \tag{3.14a}$$

$$dF_x = dL\sin\phi + dD\cos\phi. \tag{3.14b}$$

The thrust, power and torque provided by the blade element are

$$dT = F_z \tag{3.15a}$$

$$dP = dF_x N r \tag{3.15b}$$

$$d\tau = F_x r. \tag{3.15c}$$

The total thrust, power and torque can be found by integration of equations 3.15a, 3.15b and 3.15c, respectively, over the entire blade.

## 3.3 Blade element momentum theory

Blade element momentum theory is a hybrid method that combines momentum theory and BET and that overcomes the disadvantage that both momentum theory and BET treat the induced velocity as an unknown. At the correct induced velocity, both momentum theory and BET will have equal values for thrust, hence, allowing for a more generalised method of approximating fan performance. By considering the annulus of a fan disk, shown in Figure 3.4, at distance $y$ with thickness $dy$, the area of the annulus is

$$dA = 2\pi y dy. \tag{3.16}$$

By applying equation 3.16 to momentum theory as discussed in section 3.1, the elemental thrust on the fan annulus from flow rate can be calculated as

$$d\dot{m} = \rho dA v_i = \left(\frac{1}{a_w}\right)\pi v_i y dy. \tag{3.17}$$

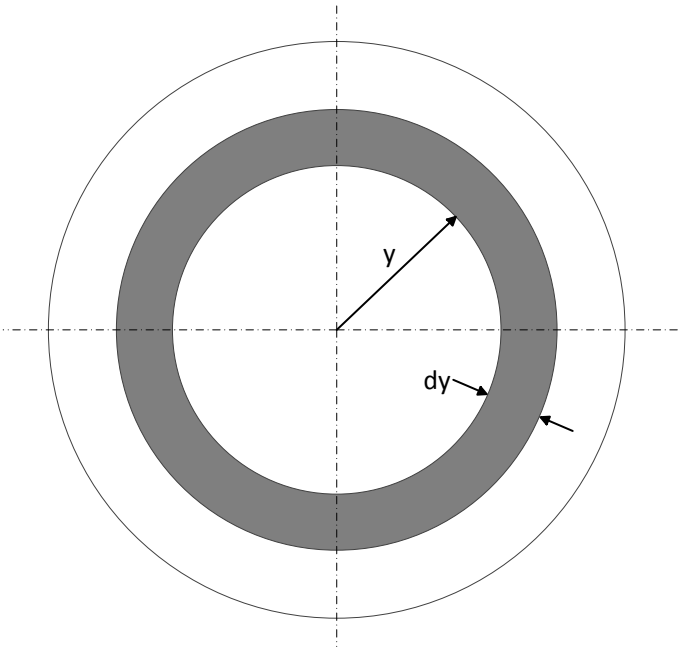


FIGURE 3.4: Annulus of a disk as used for a local momentum analysis of a fan, where $y$ is the distance to the annulus from the centre of the fan and $dy$ is the thickness of the annulus.

Therefore, the elemental thrust applied by the fan is

$$dT = \Big(\frac{1}{a_w}\Big)\rho v_i^2 dA = \Big(\frac{2}{a_w}\Big)\pi v_i^2 dy. \tag{3.18}$$

The fan performance can be found using BEMT by iterating both momentum theory and BET until the induced velocity converges. When the induced velocity has converged

$$dT_{BET} = dT_{momentum}, \tag{3.19}$$

which is equivalent to

$$\Big(\frac{2}{a_w}\Big)\pi v_i^2 dy = dL\cos\phi - dD\sin\phi. \tag{3.20}$$

Recalling that $\phi = f(v_i)$, it can be seen that equation 3.20 is an implicit equation of a single variable and can be solved accordingly.

### 3.3.1 Modification factors

Blade element momentum theory has several common modification factors that are used to correct for three dimensional effects including:

- Tip losses [33], [34]
- Hub losses (similar theory to tip losses)

- High solidity [35]

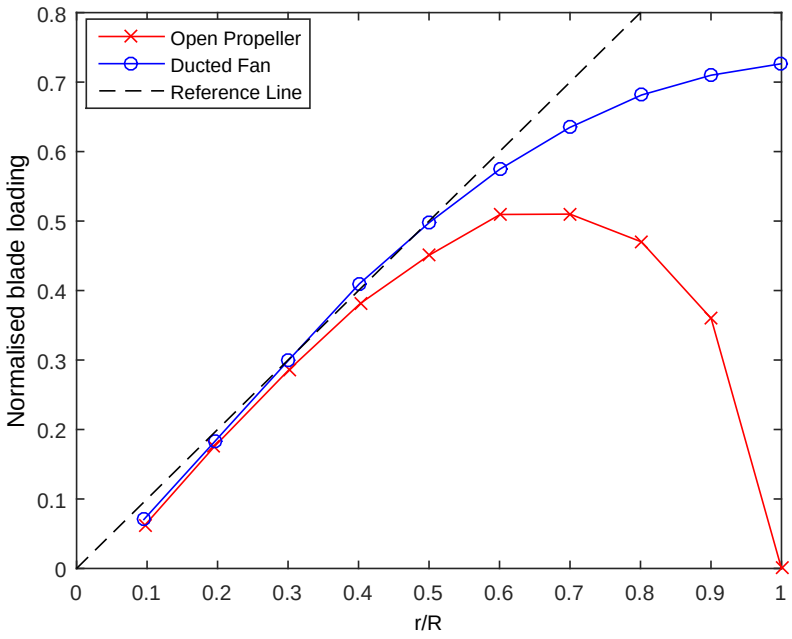


FIGURE 3.5: Comparison of the load distribution of a ducted fan and an open propeller. Modified from [35].

Shrouded fans have reduced tip losses. Figure 3.5 shows that the blade loadings normalised against the theoretical loading. If there were no losses, then Figure 3.5 would be linear. Although the ducted fan has tip losses, they are significantly lower than the tip losses from an open propeller, so a common tip loss model would not be valid. Furthermore, the minor deviation from the reference line at small radial values in Figure 3.5 shows that hub losses are insignificant, so a hub loss model is not required. The inaccuracies introduced due to not accounting for tip and hub losses will result in a small overprediction of the performance of the fan.

The design constraints imposed by manufacturing methods (see section 5.5.2) limit the solidity of the fan to 1, so there is a possibility of blade interaction effects. However, these interaction effects will not be as strong as in a very high solidity ($\sigma > 1$) fan. When blades interact with one another, each blade has reduced lift and increased drag; hence, BEMT will underpredict performance. To account for high solidity effects, it is possible to use lift and drag coefficient data from blade rows; however, this limits the designer to using empirical data rather than data generated using fast computational methods, such as panel methods. The model by Borst [35] provides an analytical method to modify the two dimensional lift and drag coefficients to match the empirical results from blade rows. Although potentially very useful, this model does not appear to have been employed in literature, so it would have to be verified before use, which is outside the scope of this project.

## 3.4 Aerofoil aerodynamic data

Blade element momentum theory requires accurate aerodynamic data for the two dimensional aerofoil shapes used in the discretisation of the blade. The lift and drag coefficients can come from experimental data or from computational results. The two most common computational methods are panel methods and complete CFD analyses.

### 3.4.1 XFOIL

A widely used panel method code is XFOIL [36], which is capable of generating lift and drag data for aerofoils in low Reynolds number, viscid flows. To use BEMT, aerodynamic data is needed for each blade element. A 200 mm fan satisfies the criteria of a low Reynolds number flow; therefore, XFOIL is a suitable solver for this project. In addition to the lift and drag data, XFOIL generates some boundary layer data such as boundary layer displacement thickness ($\delta^\star$) and momentum thickness ($\delta_2$) which are required to solve the aeroacoustic equations discussed in Section 4. In the optimisation, generation of aerodynamic data is the largest contributor to the overall solution time. The advantage of XFOIL over a full, high-fidelity CFD simulation is that XFOIL's solution times are on the order of seconds; whereas, a CFD simulation would be of order of magnitude of minutes.

### 3.4.2 Boundary layer thickness

As previously discussed, the XFOIL results include boundary layer displacement thickness and momentum thickness; however, the boundary layer thickness is not included. Drela and Giles [37] proposed the following method to predict the displacement thickness.

$$\delta = \delta_2\Big(3.15 + \frac{1.72}{H_k - 1}\Big) + \delta^\star, \tag{3.21}$$

where $H_k$ is the kinematic shape parameter which is defined as

$$H_k = \frac{H - 0.290Ma^2}{1 + 0.113Ma^2}, \tag{3.22}$$

where $H$ is the boundary layer shape factor, which is an output of XFOIL.

### 3.4.3 Data assessment

To ensure that the results generated by XFOIL are reliable, it is important to assess the generated data. The optimisation will generate a wide variety of blade shapes. For some blade sections, XFOIL will not generate adequate data, resulting in truncated data sets or data sets with holes in them. Holes in the data are only problematic if there

is a risk that the hole is in the stall region. It is important to use a conservative approach when assessing the suitability of the data as the optimisation has the potential to exploit any weakness in the approach. If there is a gap in the data larger than $2^\circ$, then the data set will be discarded, reducing the risk of identifying the wrong peak in the data as the stall point. Truncated data sets are those which do not contain data beyond stall. All truncated data sets will be discarded. To apply a post-stall model to the data, it is important to identify the stall point in the data set. Identifying the stall point can be problematic as XFOIL's data is often noisy. Furthermore, XFOIL's limited post-stall prediction often means that the peak $C_L$ value is not at stall.

A double moving average filter was applied to the $C_L$ data to remove most of the noise. Next, the inflection points and gradients of the data were calculated, and the data was truncated after the first large negative gradient if one existed. This usually removed the post-stall data. The next step was to identify the peaks using a derivative-based peak finding method with a threshold to filter any irregular peaks. The next check ensured that a gradient of 30% of the data either side of the stall point had a positive and then a negative gradient. Furthermore, checks were performed to ensure that the stall point was not within the first $2^\circ$ or final $1^\circ$ of the data set. Many of these checks perform similar tasks; however, they were all required to prevent the optimisation process from exploiting irregularities in the XFOIL data sets. The full process is shown in Figure 3.6.

### 3.4.4 Post-stall model

During the BEMT solution, the angle of attack varied as the solution iterated. This can result in evaluations at high angles of attack that are beyond the predictive capabilities of XFOIL. Viterna and Janetzke [38] proposed a method of extrapolating aerofoil data in post-stall conditions based on a flat plate model. The method starts by defining the lift and drag coefficients as functions of the angle of attack ($C_L = f(\alpha)$ and $C_D = f(\alpha)$).

$$C_L = A_1 \sin 2\alpha + A_2 \frac{\cos^2 \alpha}{\sin \alpha} \tag{3.23}$$

and

$$C_D = B_1 \sin^2 \alpha + B_2 \cos \alpha, \tag{3.24}$$

where $A_1$, $A_2$, $B_1$ and $B_2$ are all constants that provide scaling to the curve and continuity to the pre-stall data which are defined by

$$A_1 = \frac{B_1}{2}, \tag{3.25}$$

$$B_2 = C_{DMAX}, \tag{3.26}$$

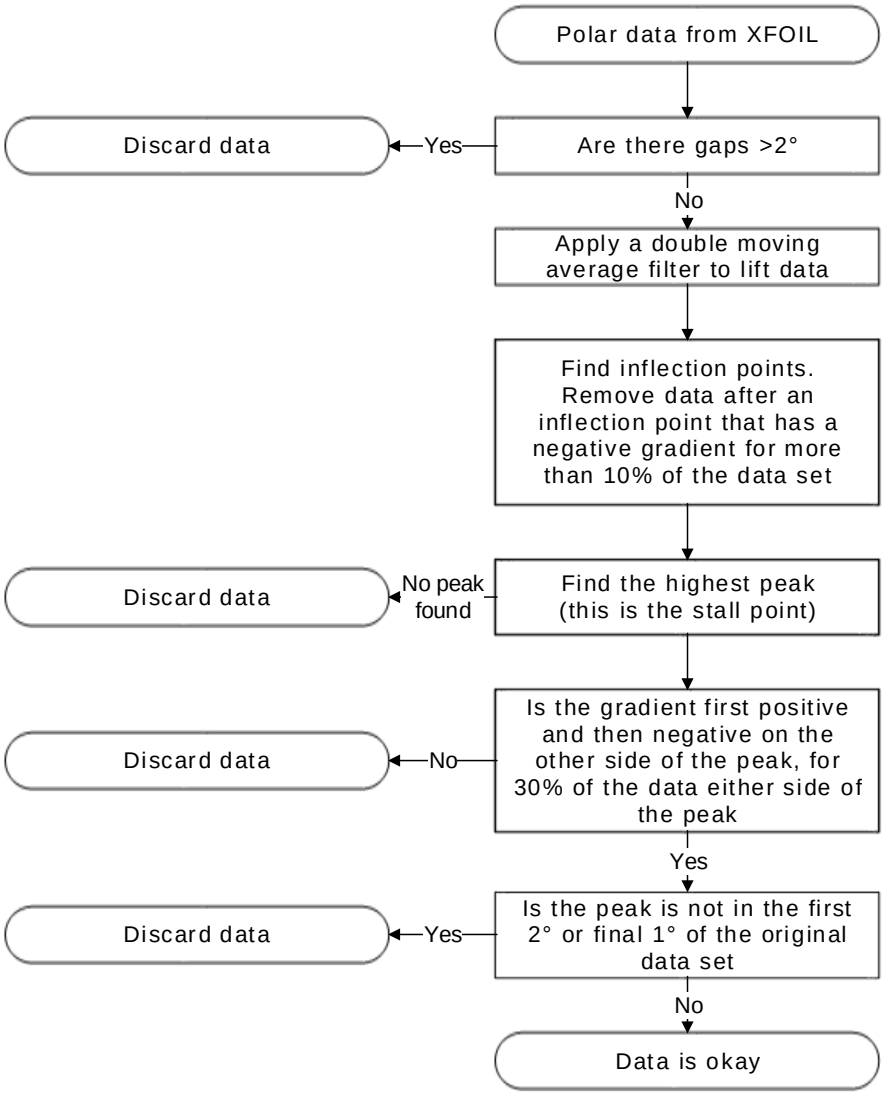


FIGURE 3.6: Aerodynamic data assessment flow chart.

$$A_2 = C_{Ls} - C_{DMAX} \sin\alpha_s \cos\left(\alpha_s \frac{\sin\alpha_s}{\cos^2\alpha_s}\right), \tag{3.27}$$

and

$$B_2 = \frac{C_{Ds} - C_{DMAX} \sin^2\alpha_s}{\cos\alpha_s}, \tag{3.28}$$

where

$$C_{DMAX} \simeq 1.11 + 0.18AR \tag{3.29}$$

and is used to estimate the maximum drag coefficient at $\alpha = 90°$ based on empirical data. For the purpose of this project, the aspect ratio ($AR$) is small and variable. The subscript $s$ is used to define values at stall. To simplify the solution process, it was assumed that $AR \approx 0$, hence,

$$C_{DMAX} \simeq 1.11. \tag{3.30}$$

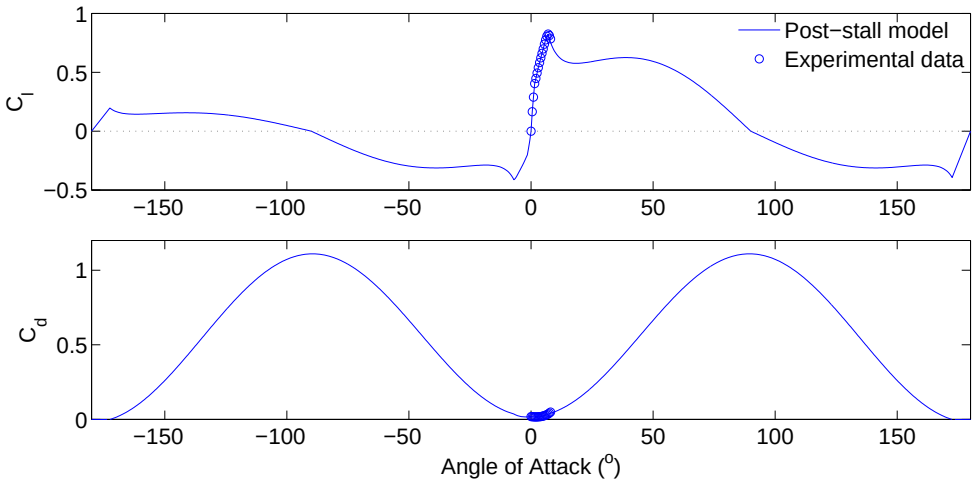


FIGURE 3.7: Example of lift and drag data from XFOIL with post-stall model for NACA0012 aerofoil.

To provide aerodynamic data over the full range of physically possible aerofoils, the data was mirrored and scaled by a factor of 0.5. This factor was loosely based on wind tunnel data [39] and mostly served to prevent an optimal solution being unrealistic.

Figure 3.7 shows the original aerodynamic data for NACA0012 aerofoil and the corresponding extrapolated data.

## 3.5 Element size

The optimal element size is the largest value of $dr$ that obtains convergence as this will reduce the required computation yet still provide an accurate answer. A convergence study was performed with results presented in Figure 3.8. From the convergence study, it can be seen that smaller element sizes give more accurate answers. The two horizontal lines drawn on Figure 3.8 indicate the approximate asymptote and a 5% variation from this line. By assuming that a 5% difference is satisfactory for convergence, the 5% variation line intersects with the flow rate line at 35 elements; therefore, 35 elements should provide adequate precision for the model and has been chosen as the optimal value.

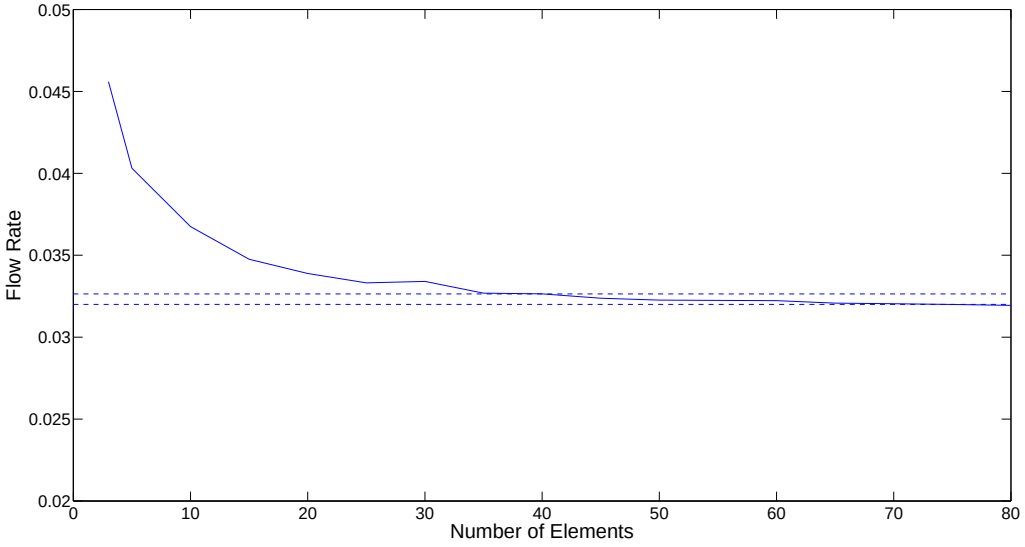


FIGURE 3.8: Convergence study on the blade element size. The two dashed lines represent the approximate asymptote and a 5% deviation from the asymptote.

# Chapter 4

# Aeroacoustic Model

There are three main noise sources in axial flow fans: self-noise, turbulent inlet noise and thickness noise as discussed in Chapter 2. In this chapter, the prediction and modelling of each of these noise sources is addressed. Similar to the aerodynamic modelling in Chapter 3, a fast solution is preferred over a slow but more accurate solution.

## 4.1 Noise models

As with the aerodynamic modelling discussed in Chapter 3, aeroacoustic modelling has a large variety of models ranging from simple order of magnitude estimates to high accuracy computational models. Lowson [40] proposed the following classification of aeroacoustic methods for wind turbines. The same classification is appropriate for axial flow fans.

- Class I: Predictions giving an estimate of the overall level as a simple algebraic function of basic machine parameters
- Class II: Predictions based on separate consideration of the various mechanisms causing fan noise using fan parameters
- Class III: Predictions utilising full information about the noise mechanisms related to a detailed description of geometry and aerodynamics, eg. they require computation of local blade element velocities and angles of attack

Class I models are simple models based on basic parameters such as fan type, diameter or speed. This type of model does not consider the geometry of the blade, so this method is not appropriate for this project.

Class II models typically model specific noise generation mechanisms separately and often apply simplifications to geometry. These methods are often able to provide reasonable predictions without extreme computational costs and are considered most suitable for this project.

Class III models utilise detailed fan geometry and flow fields, usually from CFD simulations. The most common class III methods are computational aeroacoustic (CAA) methods, which are capable of providing accurate solutions for fan noise [41]. However, the CAA analysis of fans typically requires a high fidelity large eddy simulation (LES) [42][43] which is computationally expensive and excludes its use as a design tool with the exception of well resourced research applications.

## 4.2 Strip Theory

The models presented below are for homogeneous flows over aerofoils; however, the flow over a fan blade varies radially. If the blade is split into small elements, similar to blade element theory, the flow over an element can be assumed to be in homogeneous rectilinear motion. This allows for aerofoil acoustic models to be applied to a fan. Each element is then treated as a separate sound source which can be summed using strip theory, as shown in Figure 4.1, to give the total sound pressure generated by the blade.

In some applications, an increase in the number of strips results in poor low frequency prediction. However, in the models presented below, length and sound pressure are directly proportional which means this behaviour is not observed, so a higher element count better captures the flow over the blade. Additionally, some strip theory models consider Doppler effects; however, due to the low Mach numbers of the fans in this project, Doppler effects were considered insignificant. For simplicity, the same 35 elements used in the aerodynamic predictions were also used for acoustic prediction as more elements provided little benefit but increased computational time.

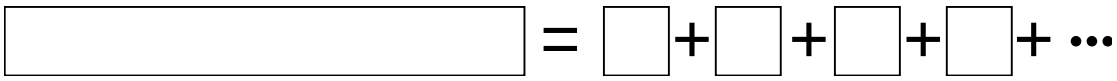

FIGURE 4.1: A graphical illustration of strip theory. The overall sound pressure is calculated by splitting the blade into many small strips to make prediction possible and then summing all contributions.

## 4.3 Self-noise

Self-noise is the total noise produced by a fan when the blade encounters a smooth, non-turbulent inflow, as discussed in Chapter 2. Self-noise can be separated into the following forms:

- Turbulent boundary layer trailing - edge noise (TBL-TE)
- Laminar boundary layer - vortex shedding noise (LBL-VS)
- Separation stall noise (S-S)
- Trailing edge bluntness - vortex shedding noise (TEB-VS)
- Tip vortex formation

In the current application of a shrouded axial flow fan, the first four are relevant noise sources. Similarly to the aerodynamic model, it is expected that the shroud will significantly reduce the generation of tip vortices, limiting tip vortex noise generation.

### 4.3.1 Self-noise mechanisms

#### 4.3.1.1 Turbulent boundary layer trailing edge noise

At high Reynolds numbers, turbulent boundary layers are able to develop over most of the aerofoil. TBL-TE noise occurs as a result of the turbulent boundary layer interacting with the trailing edge as shown in Figure 4.2.

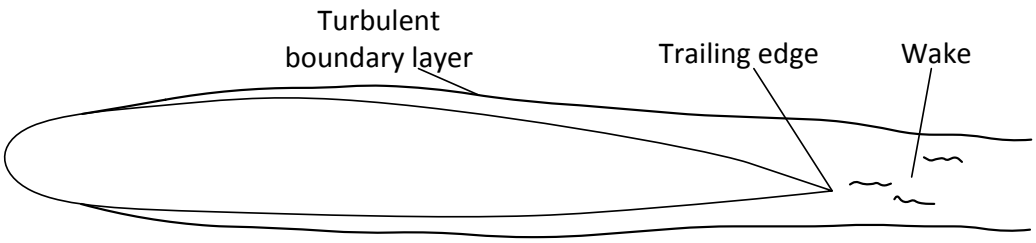


FIGURE 4.2: Representation of turbulent boundary layer - trailing edge noise.

#### 4.3.1.2 Laminar boundary layer vortex shedding noise

At low Reynolds numbers, laminar boundary layers tend to dominate over the blade. The laminar boundary layer has instabilities which interact with the trailing edge to generate noise, as shown in Figure 4.3.

#### 4.3.1.3 Separation stall noise

For a non-zero angle of attack, the flow can separate near the trailing edge on the suction side, which sheds turbulent vortices and acts as a noise source, as shown in Figure 4.4A. At high angle of attacks, the flow can become highly separated which generates a

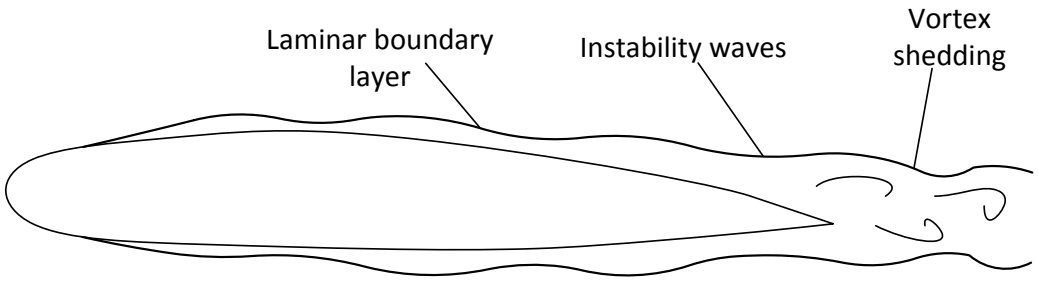


FIGURE 4.3: Representation of laminar boundary layer - trailing edge noise.

strong low frequency noise source, similar to a bluff body in a flow, as shown in Figure 4.4B.

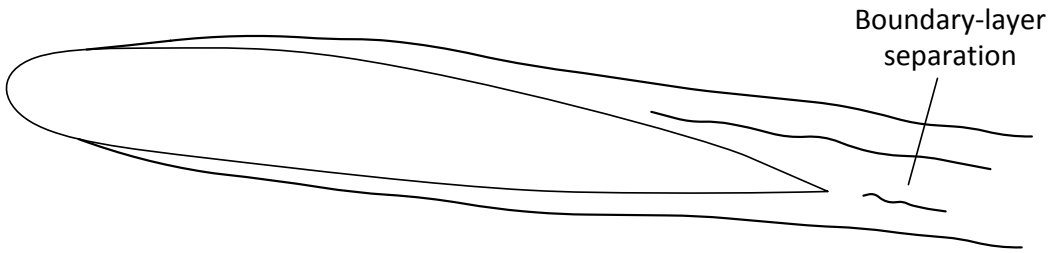


(A) Low-moderate angle of attack.

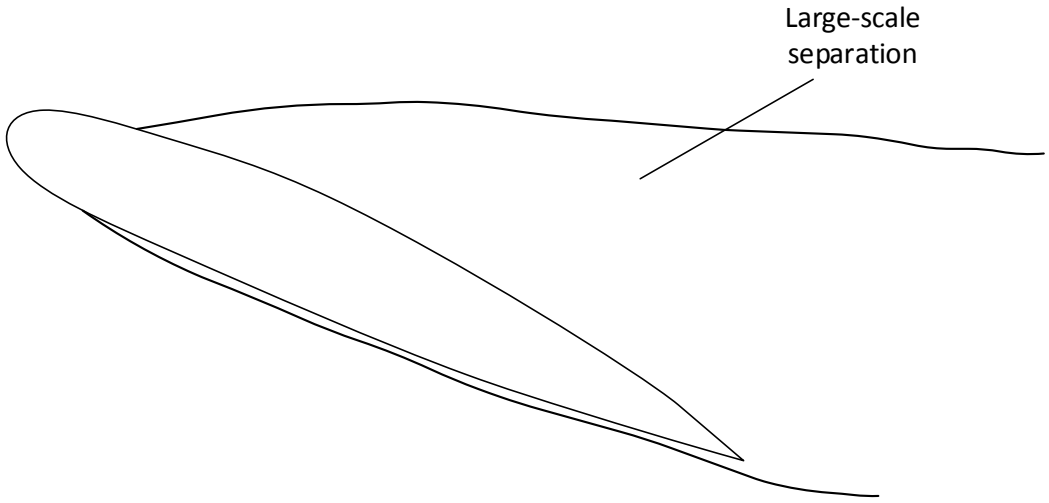


(B) High angle of attack.

FIGURE 4.4: Representation of separation stall noise.

#### 4.3.1.4 Trailing edge bluntness vortex shedding noise

Blunt trailing edges can generate vortices behind the trailing edge, as shown in Figure 4.5. The degree of bluntness results in an increase in noise generation.

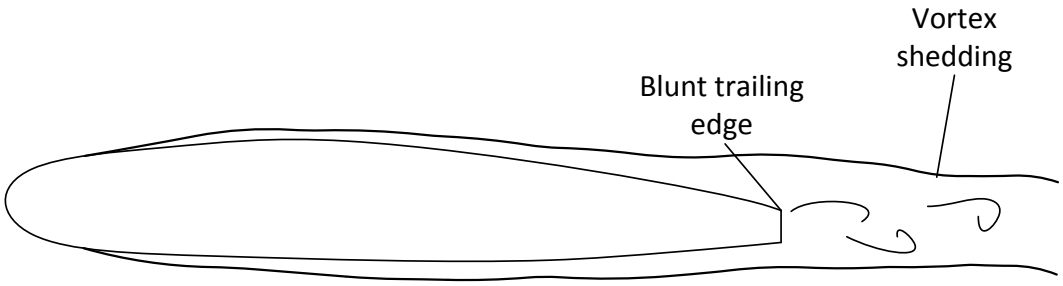


FIGURE 4.5: Representation of trailing edge bluntness vortex shedding noise.

### 4.3.2 Self-noise modelling

The self-noise prediction model used in this study was the Brooks, Pope and Marcolini (BPM) prediction method [17]. This is a semi-empirical method that is based on the normalisation and spectral scaling of empirical data from various chord length NACA0012 aerofoils. The BPM method estimates the sound pressure level (SPL) of each noise mechanism in 1/3-octave bands for each blade element. The sound pressure levels of the elements can be summed using strip theory and the total sound pressure can be calculated as

$$L_{p,total} = 10\log\left(10^{\frac{L_{p,\alpha}}{10}} + 10^{\frac{L_{p,s}}{10}} + 10^{\frac{L_{p,p}}{10}} + 10^{\frac{L_{p,LBL-VS}}{10}} + 10^{\frac{L_{p,TEB-VS}}{10}}\right), \tag{4.1}$$

from which the sound power level (SWL) can be calculated by

$$L_w = L_{p,total} + 10\log\frac{1}{4\pi r_e^2}. \tag{4.2}$$

For convenience, the reference distance ($r_e$) is set to unity. The method to calculate the sound pressure level for each source is presented below.

#### 4.3.2.1 Turbulent boundary layer - trailing edge noise and separated flow noise

The pressure and suction side of the trailing edge each generate noise independently of the other so their individual contributions are calculated separately. The pressure side contribution is given by

$$L_{p,p} = 10\log\left(\frac{\delta_p^\star Ma^5 L\bar{D}_h}{r_e^2}\right) + A + (K_1 - 3) + \Delta K_1, \tag{4.3}$$

the suction side by

$$L_{p,s} = 10\log\left(\frac{\delta_s^\star Ma^5 L\bar{D}_h}{r_e^2}\right) + A + (K_1 - 3), \tag{4.4}$$

and separation noise by

$$L_{p,\alpha} = 10 \log \left( \frac{\delta_s^\star M a^5 L \bar{D}_h}{r_e^2} \right) + B + K_2, \tag{4.5}$$

where $A$ and $B$ are empirical shape functions, and $K_1$, $\Delta K_1$ and $K_2$ are scaling functions which are defined in Appendix A. $\bar{D}_h$ is a directionality function, which for the purpose of this project is unity as the overall sound power is the desired result.

#### 4.3.2.2 Laminar boundary layer - vortex shedding noise

The LBL-VS noise spectrum is predicted by

$$L_{p,LBL-VS} = 10 \log \left( \frac{\delta_p M a^5 L \bar{D}_h}{r_e^2} \right) + G_1 + G_2 + G_3, \tag{4.6}$$

where $G_1$, $G_2$ and $G_3$ are functions defined in Appendix A.

#### 4.3.2.3 Trailing edge bluntness - vortex shedding noise

The TEB-VS noise is predicted by

$$L_{p,TEB-VS} = 10 \log \left( \frac{h M a^{5.5} L \bar{D}_h}{r_e^2} \right) + G_4 + G_5, \tag{4.7}$$

where $G_4$ and $G_5$ are functions defined in Appendix A, and $h$ is the is the trailing edge thickness.

## 4.4 Turbulent inlet noise

Another noise source from axial flow fans are the pressure fluctuations caused by incident turbulence (IT). The IT causes a variation in the flow velocity which, in turn, results in a fluctuation in the lift force, which ultimately results in an acoustic pressure. The level of IT noise is strongly related to the intensity and length of the IT, which is application dependent. Often the best method to mitigate IT noise is to reduce the turbulence by limiting upstream obstructions and using bellmouths. A brief experimental investigation on a 200 mm, 26°, plastic, cambered-plate fan was undertaken following the method described in Chapter 8. A grid with 25 mm thick bar and 90 mm spacing between bars was used. Turbulent flow from the grating was confirmed by using thread on a rod.

The results of the investigation are recorded in Figure 4.6 which shows the effect of turbulence. It is known that both the self-noise and IT noise vary with $SWL \propto v^5$,

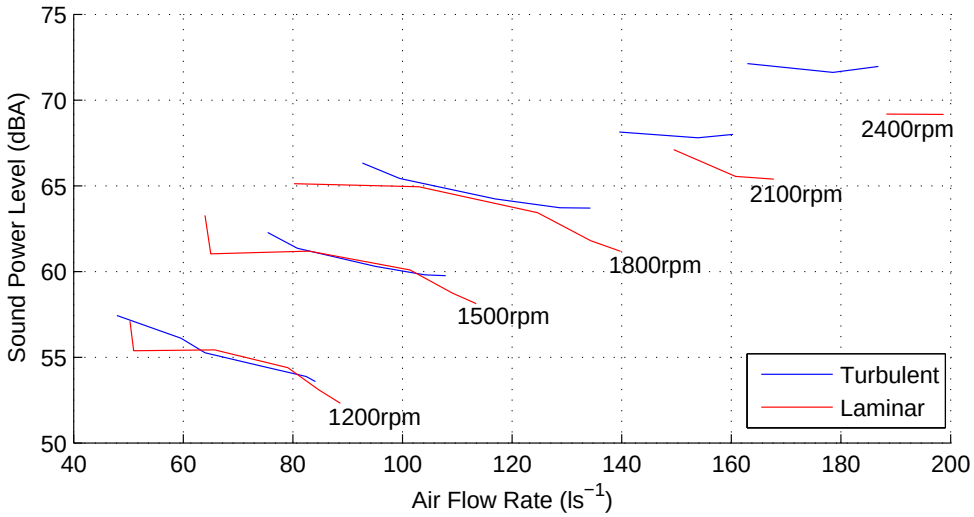


FIGURE 4.6: Comparision of fan noise with and without incident turbulence in a 200 mm, 26°, plastic, cambered-plate fan.

| Description | $\Lambda$ (mm) | $I$ |
|---|---|---|
| Natural inflow through bellmouth | 12-35 | 0.006-0.142 |
| 10x10 mesh with 65x65 spaces | 9-16 | 0.125-0.209 |
| 15x15 mesh with 60x60 spaces | 10-18 | 0.167-0.213 |

TABLE 4.1: Values of turbulence intensity and length for various meshes, reproduced from [44].

so the influence of turbulence on the sound power should be constant for constant IT. However, this is not what was experienced. As the velocity increased, the turbulence caused by the grid also increased. The increase in turbulence increased the noise generated by the turbulence. This implies that IT noise does not need to be considered for rotational velocities under 1800rpm. For higher rotational velocities, IT noise should be considered.

The narrowband spectra for a test with a increase in overall SWL is presented in Figure 4.7. The spectra shows that IT produces an increase in broadband noise, particularly at frequencies below 2 kHz. This is important as this frequency range allows for IT noise to be treated as compact, which simplifies the modelling of IT noise.

### 4.4.1 Modelling of incident turbulence noise

Incident turbulence noise is more challenging to model than self-noise as the phenomenon is more complex and is affected by application dependant factors and fan geometry. To model the IT noise, a Class II prediction method will be used in this

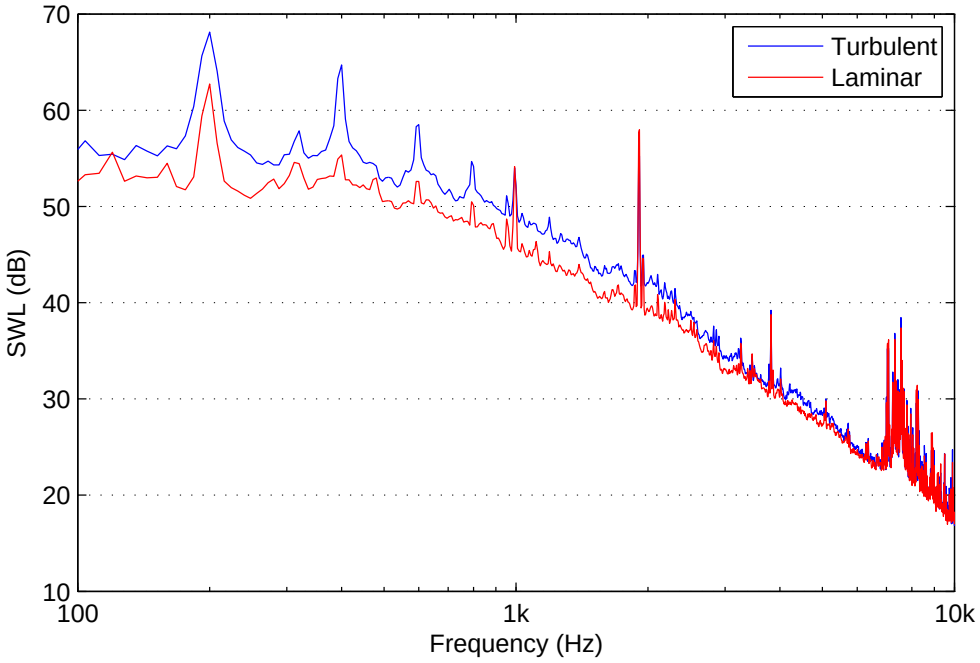


FIGURE 4.7: Comparision of sound power spectra of a 200 mm, 26°, plastic, cambered plate fan at 2100 rpm with and without incident turbulence.

study. Although there are several simple semi-empirical models [8], [44] that give a reasonable approximation, the model used in this project is the analytical model of Amiet [45]. Unfortunately, none of the aforementioned IT models consider the effects of blade geometry on IT noise since IT models that utilise blade geometry require the use of computationally expensive CAA methods. The form of Amiet's model used in this project was

$$L_{p,IT} = 10 \log \left( \frac{\Lambda d r}{{r_e}^2} M a^5 I \frac{\hat{k}^3}{(1+\hat{k}^2)^{\frac{7}{3}}} \right) + 181.3 \tag{4.8}$$

which is consistent with the self-noise model described in Section 4.3 by providing results in 1/3 octave bands. $\hat{k}$ is the wave number defined as $\hat{k} = \frac{2\pi f}{U}$. The turbulence integral length ($\Lambda$) and intensity ($I_{turb} = \frac{\bar{u}^2}{U^2}$) is highly dependant on the size and shape of the obstruction as well as the velocity of the air. Carolus et al. [44] took a series of hot wire measurements with various gratings to determine the turbulence properties for which the results relevant to this study are reproduced in Table 4.1.

# Chapter 5

# Optimisation and Parameterisation

The aim of optimisation was to determine the ideal design for a blade that provides high aerodynamic performance and minimal noise generation. This was done by using the aerodynamic and acoustic models presented in Chapter 4 in conjunction with an optimisation method. Using conventional notation, the optimisation process is: given a set $X$ and the objective function, $f : X \to \mathbb{R}$, we want to find $x^\star \in X$ such that for all $x \in X$, there holds $f(x) \geq f(x^\star)$. The variable $x$ is the control variable that defines the shape of the blade, and $f$ is the objective function which will be defined in this chapter. This chapter also presents the parameterisation of the blade, optimisation algorithm used and the constraints imposed on the optimisation.

## 5.1 Parameterisation

The objective of the optimisation is to determine the blade geometry that generates high flow rate, low noise and meets all imposed constraints. In order to do this, the fan performance models must evaluate the geometry in the form in which it is output from the optimisation code. The model discussed in Chapters 3 and 4 discretises a blade into elements which are separately analysed and then integrated over the entire blade to find the total fan performance. Blades are commonly discretised by defining an aerofoil at the root, midpoints and tip and interpolating between these aerofoils to define the blade shape [28], [46]. Attempts to discretise the blade into three sections using the model in Chapter 3 resulted in a high failure rate. This occurred because because XFOIL is unable to solve for non-typical aerofoil shapes, and if only one of the defined aerofoils could not solve, a result for the fan could not be generated. The parameterisation method used in this work defines one aerofoil cross-section for the fan blade. This reduction in generality is justified by the significant increase in solver stability, which increases the rate of convergence and reduces solver times.

To be compatible with XFOIL, the aerofoil for each element must be defined in two columns containing $x$ and $y$ shape data. This list of data points should have a high resolution with 100-200 data points per aerofoil so that the panel method employed by XFOIL is able to predict the flow over the aerofoil accurately. It would be possible to set the $x$ and $y$ points of the aerofoil to be variables in the optimisation; however, the high number of variables would result in an overly complex problem which would have high computational time and poor convergence. A better method is to parameterise the aerofoil.

Early methods of aerofoil shape definition include the well known NACA 4 and 5 series aerofoils [47] which define the shape of the aerofoil using maximum camber, the distance from the leading edge to the point of maximum camber and the maximum thickness of the aerofoil. This definition defined a large and popular set of aerofoils; however, the shape of the NACA aerofoils are more limited compared to other shape parameterisation methods. Sobieczky proposed a new method for defining the shape of aerofoils known as the PARSEC method [48]. The PARSEC method uses 11 basic parameters to define the shape of an aerofoil giving greater control over curvature compared to the NACA aerofoils. Although PARASEC has been used in aerofoil optimisation [49], it has been shown that the PARASEC method provides less accurate results than splines [50]. The most popular method for aerofoil parameterisation in aerofoil optimisation [51], [52] and fan blade optimisation [28] are B-splines. Other methods, such as Bézier curves [46] and Fourier sine series [53], have been used in optimisation with varying degrees of success. B-splines are advantageous as free-form geometry can be accommodated with fewer variables. However, there are difficulties controlling the positions of the B-spline control points. In an optimisation problem, this can result in complicated constraints and the potential for unsuitable aerofoil geometry.

### 5.1.1 B-splines

Basis splines, more commonly known as B-splines, are essentially Bézier curves aligned end on end. Although B-splines require additional information and are more complex than Bézier curves, they have several advantages. The most important advantage in this study is that, unlike Bézier curves, the degree of a B-spline is independent of the number of control points. This allows for better control over the shape; by changing a B-spline's control point, the shape of the curve will locally change; whereas, a Bézier curve will globally change. This property is called the local modification property and will improve the optimisation's rate of convergence.

B-splines are defined similarly to Bézier curves as shown in equation 5.1. The following definitions of B-splines are from [54], [55].

$$S(t) = \sum_{i=0}^{n} N_{i,k}(t) B_i. \tag{5.1}$$

where $S$ is the B-spline curve, $t$ are the knots, $n$ is the number of control points, $N$ is the basis function and $B$ are the control points. The basis function is defined as the de Boor algorithm shown in equation 5.2.

$$N_{i,j}(t) = \frac{t - t_i}{t_{i+j} - t_i} N_{i,j-1}(t) + \frac{t_{i+j+1} - t}{t_{i+j+1} - t_{i-1}} N_{i+1,j-1}(t) \tag{5.2a}$$

$$N_{i,0}(t) = \begin{cases} 1 & \text{if } t_i \leq t < t_{i+1} \\ 0 & \text{if otherwise} \end{cases} \tag{5.2b}$$

The basis functions can be written in the following triangular scheme,

$$\begin{array}{ccccccc} N_{0,0}(t) & \rightarrow & N_{0,1}(t) & \dots & N_{0,k-1}(t) & \rightarrow & N_{0,k}(t) \\ & \nearrow & & & & \nearrow & \\ N_{1,0}(t) & \rightarrow & N_{1,1}(t) & \dots & N_{1,k-1}(t) & & \\ \vdots & & \vdots & & & & \\ N_{n-1,0}(t) & \rightarrow & N_{n-1,1}(t) & & & & \\ & \nearrow & & & & & \\ N_{n,0}(t) & & & & & & \end{array} \tag{5.3}$$

which more clearly shows the process through which the basis function is solved. The first column, for which $j = 0$, can be solved using equation 5.2b. The remaining values of the basis function are solved for using equation 5.2a which, as shown by the triangular scheme, requires multiple other values of the basis function. In application, the basis function can be solved recursively, as shown in the triangular scheme, or through an algebraic approach which allows for solving using matrix multiplication. The algebraic approach was used in this project (see [55] for details) because it is computationally more efficient.

Knots are defined in a knot vector ($\overrightarrow{T}$). The knot vector determines which basis function has an effect on the curve at that point and is defined as

$$\overrightarrow{T} = (t_0, t_1, \dots, t_m) \tag{5.4}$$

where

$$t \in [t_0, t_m]. \tag{5.5}$$

Consideration of equation 5.2 with this in mind shows that the knots that $t$ lies between determine the basis function, which affects the shape of the B-spline. The length of $\overrightarrow{T}$

is $m + 1$, where

$$m = k + n + 1, \tag{5.6}$$

$k$ is the degree of the curve, and $n$ is the number of control points. The values of the knots can be any rational number that monotonically increases.

Depending on the knot vector, open, clamped or closed b-splines can be formed, as shown in Figure 5.1. Aerofoils are typically specified with a trailing edge gap, which renders open and closed b-splines unsuitable; therefore, a clamped B-spline is most suitable for parameterisation of an aerofoil.

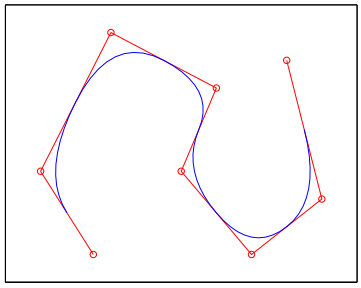

(A) Open B-spline.

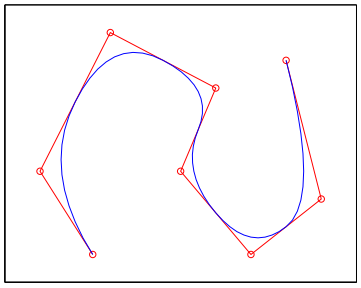

(B) Clamped B-spline.

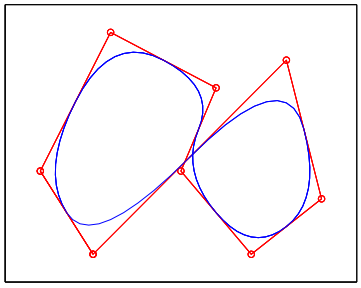

(C) Closed B-spline.

FIGURE 5.1: Comparison of B-spline curves. Blue lines show the B-spline, and red lines show the control points.

### 5.1.2 Aerofoil representation by B-splines

The chosen method of aerofoil definition is obtained by joining two B-spline curves together with one for the upper surface and one for the lower surface. Each curve is defined by seven control points and a knot vector, $\overrightarrow{T}$=(0, 0, 0, 0, 0.25, 0.5, 0.75, 1, 1, 1, 1). The leading edge control point will be set to (0,0), the second control point set to (0,$y_1$) and the trailing edge control point set to (1, $t_{te}/2$) where $y_1$ is a variable position and $t_{te}$ is the trailing edge thickness. Figure 5.2 provides a graphical representation of the control points.

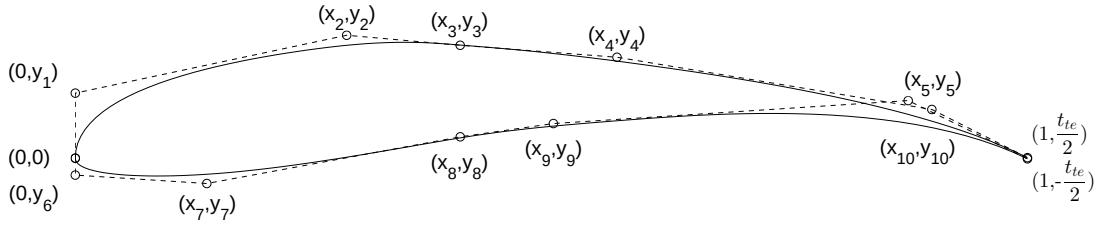


FIGURE 5.2: Control points used to specify the B-spline that parameterises an aerofoil.

Figure 5.3 show that B-splines successfully capture the geometry of a variety of common aerofoils. The curves were matched through a minimisation of the least square error between the known aerofoil and the B-spline using particle swarm optimisation (see section 5.2). This shows that the method detailed in this section is suitable for use in optimisation.

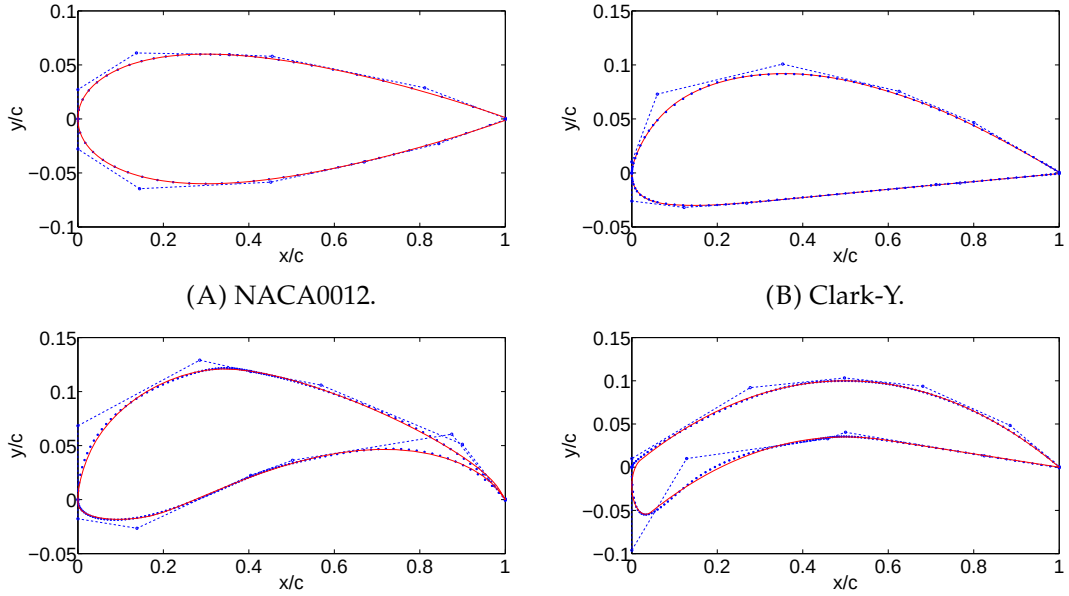


(A) NACA0012.

(B) Clark-Y.

(C) Selig 1210.

(D) Cambered plate C=10% T=5% R=1.3.

FIGURE 5.3: Fitting B-splines to known aerofoils. The control points and splines are overlain on common aerofoils.

### 5.1.3 Uniform thickness blade

Fans are often made with uniform thickness to simplify the manufacturing process. This is the case for pressed-aluminium fans where a sheet of aluminium is pressed to make a fan or for cheaper injection-moulded fans than fans with aerofoil cross-sections. The shape of uniform thickness blades are typically cambered plates. To allow for the optimisation of a uniform thickness fan, a cambered-plate cross-section must be parameterised.

Cambered plates are defined by their median camber line and blade thickness. A Bézier curve adequately describes the median camber line, and a 2 mm thickness will be used. Pelletier and Mueller [56] showed empirically that the leading edge and trailing edge geometries have negligible effects on the lift and drag of a cambered plate. However, Reid [57] showed that the leading and trailing edges have an effect in the numerical prediction of lift and drag in XFOIL. This means that the leading edge and trailing edge geometries in the model can be different to the tested geometry, yet still generate the same results. This study used the circular leading edge and parabolic trailing edge that Reid proposed.

The circular leading edge has a radius of $0.5T$ where $T$ is the normalised thickness of the aerofoil. To achieve tangency and maintain the leading edge at the origin, the median camber line starts at $x = 0.5T$. A parabolic trailing edge was used instead of a circular trailing edge as this better fulfils the Kutta condition which aids in convergence. The parabolic trailing edge starts at $0.9c$ and gradually reduces to the trailing edge thickness at $1c$. The parabolic trailing edge also maintains tangency. An example of a cambered-plate cross-section is in Figure 5.4.

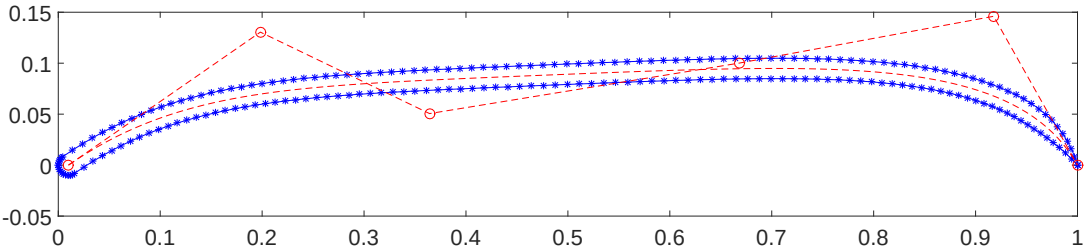


FIGURE 5.4: Example of a cambered-plate with a Bézier curve mean camber line, circular leading edge and parabolic trailing edge.

The cambered plate is parametrically defined by a single Bézier curve with the first control point fixed at $(0.5T, 0)$, and the final control point at $(1, 0)$. Four control points between the leading and trailing edges were each controlled through their $x$ and $y$ coordinates. This resulted in 8 variables controlling the shape of the cambered plate in the optimisation.

### 5.1.4 Chord and angle of attack

The earlier discussion on the definition of an aerofoil produces a normalised aerofoil with a zero twist angle. Therefore, each element must be scaled by the chord length and angled according to the twist angle. Because each of these parameters is accounted for in the methods described in Chapters 3 and 4, the chord and twist angle simply have to be parameterised so that the optimisation process can vary them. This is done using Bézier curves, which define the chord and twist angle against normalised radial position as shown in Figure 5.5.

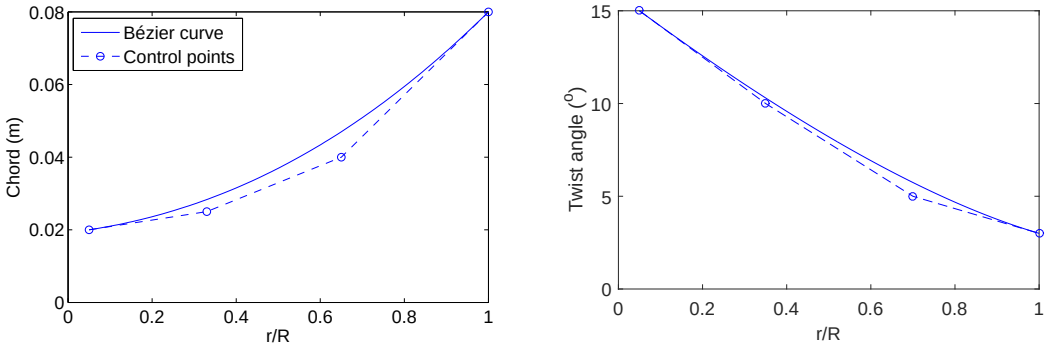


(A) Chord. (B) Twist angle.

FIGURE 5.5: Bézier curve definition of chord and twist angle for fan parameterisation.

## 5.2 Optimisation

The optimisation process aims to find the fan blade shape that minimises the objective function and meets the imposed constraints, which are described in Section 5.5. The complications in this optimisation arise from the high number of parameters required to achieve adequate generality (up to 34 parameters), the non-smoothness of the solutions (this is further exacerbated by XFOIL's inability to solve for non-aerofoil shapes.) and the objective function being non-differentiable. Although the gradient could be approximated using finite differences, this would require additional calls to the solver, which would significantly increase computation time.

The most suitable optimisation class for this problem is metaheuristics. Metaheuristic optimisation is more suitable for solving large size problems in a reasonable amount of time than conventional exact methods [58]. In fan optimisation, it is common to use metaheuristic optimisation with studies using genetic algorithms (GA) [28], [46]. However, studies into the quality and speed of various metaheuristic methods have shown particle swarm optimisation (PSO) to outperform GA and other methods [59], [60]. Furthermore, PSO is suitable for this project as it is designed for continuous problems, and like other population-based metaheuristic methods, PSO easily interacts with existing solvers and can be parallelised in an efficient manner.

## 5.3 Particle swarm optimisation

Particle swarm optimisation is a nature-inspired metaheuristic optimisation method. PSO was first proposed by Kennedy and Eberhart in 1995 [61] whom were inspired by the concept of a flock of birds searching for food. PSO is based on a system of particles initialised at random positions with random velocities which fly around in the search

space. At each time step, the particles' positions are updated based on their velocity,

$$v_{i,t+1} = wv_{i,t} + C_1 r_1(P_i - x_{i,t}) + C_2 r_2(P_G - x_{i,t}), \tag{5.7}$$

where subscripts $i$ and $t$ denote the particle number and the 'time' (iteration number), respectively. $P_i$ is the best solution known to a particle, $P_G$ is the best solution found by any particle in the swarm and $r_1, r_2 \in [0, 1]$ are random numbers. The position of each particle is defined by $x_{i,t}$ and is updated each iteration by

$$x_{i,t+1} = x_{i,t} + v_{i,t+1}. \tag{5.8}$$

The accuracy and rate of convergence is strongly related to three weightings: $w$ the inertia factor, $C_1$ the self confidence factor and $C_2$ the swarm confidence factor. An additional factor that is commonly used is $V_{max}$ which serves as a constraint that controls global exploration, preventing the system diversifying too rapidly into an unrealistically large search space. $V_{max}$ should be set to a value that restricts a particle from transcending the entire search space in one iteration. The confidence factors for this study were both set to 1.5 which is recommended in [59]. The inertial weight was more complicated and deserves a more thorough discussion, below. The only potential issue with this algorithm occurs when $P_i$ and $P_G$ move apart. This causes the particles to oscillate between $P_i$ and $P_G$ without converging; however, with the careful selection of the coefficients, this can be avoided.

### 5.3.1 Inertia factor

It is well known that for a large value of $w$ the particles provide a more global search; whereas, for a small value of $w$, the particles do a local search. Because of this, it is ideal that the search starts with a large value of $w$ and decreases to a smaller value as the search progresses and the search region narrows. Bansal et al. [62] compared 15 different inertial weight methods' errors and the number of iterations in five different optimisation problems. From this research, it was shown that chaotic inertial weights provide small errors at the expense of high iterations, and random inertial weights provide the best efficiency with a trade-off of higher errors. A logarithmically decreasing method provided good efficiency with low errors and was chosen for this project. The logarithm decreasing method [63] varies the inertia weight as

$$w = w_{max} + (w_{min} - w_{max}) \times \log\left(1 + \frac{10t}{maxiter}\right), \tag{5.9}$$

where $w_{max}$ is the maximum inertia factor, $w_{min}$ is the minimum inertia factor, $t$ is the current iteration and $maxiter$ is the maximum iterations for the problem. In this project, $w_{max} = 0.9$ and $w_{min} = 0.4$. The shape of the curve is given by equation 5.9 and is shown in Figure 5.6.

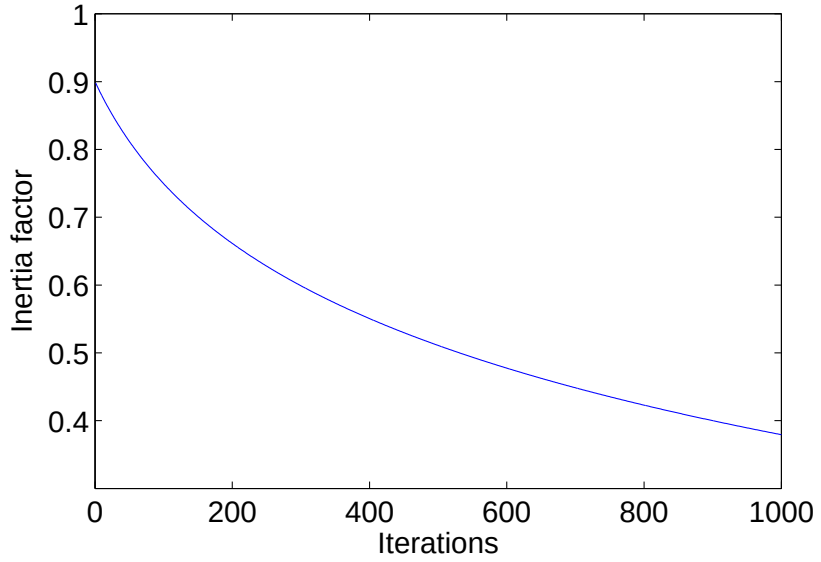


FIGURE 5.6: Logarithm decreasing inertial weight with $W_{max} = 0.9$ and $W_{min} = 0.4$ and $maxiter = 1000$.

## 5.4 Multi-objective particle swarm optimisation

Until this point, the discussion of PSO has been deliberately left broad as there are several potential properties of the fan to optimise for. In this project, it was desirable to find an optimal design that balanced both flow rate and noise; this required the use of multi-objective optimisation. Multi-objective particle swarm optimisation (MOPSO) was used to find an optimal trade-off between flow rate and noise subject to a set of constraints such as

$$\text{minimise } \vec{f}(\vec{x}) := [f_1(\vec{x}), f_2(\vec{x})] \tag{5.10}$$

subject to the inequality constraints,

$$g_i(\vec{x}) \leq 0 \quad i = 1, 2, ..., m, \tag{5.11}$$

and the equality constraints,

$$h_j(\vec{x}) \leq 0 \quad j = 1, 2, ..., p, \tag{5.12}$$

where $\vec{x} = [x_1, x_2, ..., x_n]^T$ is the vector of decision variables, $f_i : \mathbb{R}^n \to \mathbb{R}, i = 1, 2$ are the objective functions and $g_i, h_i : \mathbb{R}^n \to \mathbb{R}, i = 1, ..., m, j = 1, ..., p$ are the constraint functions. To further the discussion of MOPSO, the following definitions related to multiple objective optimisation from [64], [65] are defined:

**Definition 1** Given two vectors where $\vec{x}, \vec{y} \in \mathbb{R}^k$, it can then be said $\vec{x} \leq \vec{y}$ if $x_i \leq y_i$ for $i = 1, \ldots, k$. It is then said that $\vec{x}$ **dominates** $\vec{y}$ (denoted as $\vec{x} \prec \vec{y}$) if $\vec{x} \leq \vec{y}$ and $\vec{x} \neq \vec{y}$. Figure 5.7 shows the dominance relation for two objective functions.

**Definition 2** It is said that a vector, $\vec{x}$ is **nondominated** if there is no other vector, $\vec{y}$ such that $f(\vec{x}) \prec (\vec{y})$. For MOPSO, this relates to the position vector defined by each particle.

**Definition 3** It is said that a vector of decision variables $\vec{x} \in \mathcal{F} \subset \mathbb{R}^n$ ($\mathcal{F}$ is the feasible region) is **Pareto-optimal** if it is non dominated with respect to $\mathcal{F}$.

**Definition 4** The **Pareto optimal set** ($\mathcal{P}$) is defined by $\mathcal{P} = \{\vec{x} \in \mathcal{F} | \vec{x} \text{ is Pareto-optimal}\}$.

**Definition 5** The **Pareto front** ($PF$) is defined by $PF = \{\vec{f}(\vec{x}) \in \mathbb{R}^k | \vec{x} \in \mathcal{P}\}$. A Pareto front is shown in Figure 5.8.

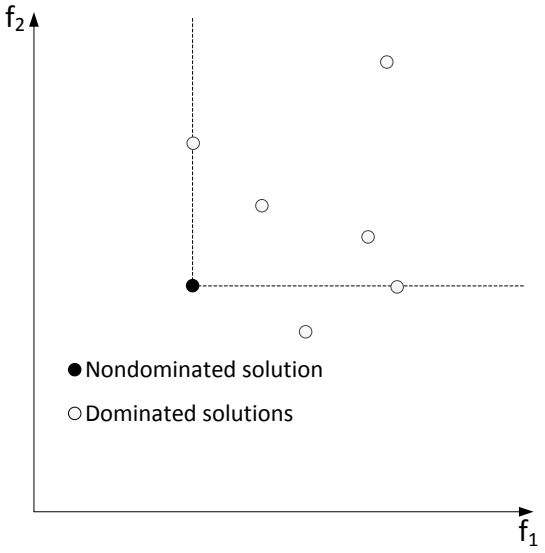


FIGURE 5.7: Example of dominance in multi-objective optimisation of two objectives.

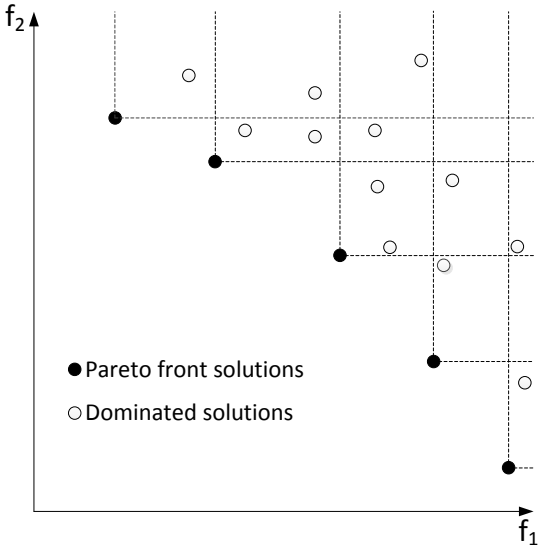


FIGURE 5.8: An example of a Pareto front in the multi-objective optimisation of two objectives.

As discussed in [64], there are a wide variety of proposed MOPSO methods. However, there does not seem to be consensus on which method is the best. In this project, the popular method by Coello Coello et al.[65] was used, which was shown to outperform multi-objective GA methods in accuracy and speed for all test cases.

### 5.4.1 Algorithm

The MOPSO algorithm used in this project is from [65] and utilises a repository and mutation in order to achieve a wide Pareto front with uniform spacing without premature convergence. The repository and mutation are discussed in sections 5.4.2 and 5.4.3, respectively. The MOPSO algorithm is defined below with supplementary text describing areas that require elaboration.

**Algorithm 1** MOPSO algorithm

**procedure** MOPSO($f, g, h$) ▷ Minimise $f$ subject to $g$ and $h$
    Initilise position of population
    Initilise velocity of population
    Evaluate population against objective functions
    Store positions of nondominated particles in repository
    Initilise the memory of each particle (set local best position)
    **while** iter<maxiter **do**
        Calculate $REP(h)$ ▷ h is chosen so that diversity is increased
        Calculate velocity using equation 5.13
        Calculate the new positions of the particles
        Impose boundary constraints
        Evaluate the objective functions for each of the particles
        Update the repository
        **if** repository is full **then**
            Replace less suitable positions
        **end if**
        **if** $x_i > P_i$ **then**
            update $P_i$
        **end if**
        Increment the loop counter
    **end while**
**end procedure**

$$V_i = wv_i + r_1(P_i - x_i) + r_2(REP(h) - x_i) \tag{5.13}$$

The optimal coefficients and population sizes for MOPSO differ from PSO. Coello Coello [65] suggested optimal values, based on a series of simulations, which are summarised in Table 5.1.

| Variable | Value |
|---|---|
| Momentum factor | 0.4 |
| Number of particles | 100 |
| Number of cycles | 80 to 120 |
| Number of hypercube divisions | 30 |
| Size of repository | 250 |

TABLE 5.1: Values for the constants in MOPSO suggested by Coello Coello[65].

### 5.4.2 Repository

The repository is an external record of the non-dominated vectors found throughout the optimisation process. The repository consists of an archive controller and a grid, which are both explained below. The archive controller decides if a vector should be moved to the repository based on the following criteria:

- If the archive is empty, then the current vector is accepted.
- If the current vector is dominated by one in the repository, then it is discarded.
- If the current vector is non-dominated by the repository, then it is added to the repository.
- If a solution in the repository is dominated by the current vector, then the solution in the repository is removed.
- If the repository reaches is maximum size, then items are discarded using the grid method described below.

The grid is a method which aims to generate equal spacing in the Pareto front. The solution space of the repository is divided into a grid using equispaced hypercubes with each particle placed within a region in the grid. If a new particle lies outside of the current grid, then the grid is regenerated to include all particles. When the repository reaches its maximum number of values, points are removed from the grid based on the number of particles in each cube. This is done by removing one particle from the region that contains the greatest number of particles (or one from each region if more than one region contains the same number of particles).

The repository interacts with the swarm through the factor $REP(h)$ in equation 5.13. If any region in the grid contains more than one particle, then the particles in the grid are assigned a fitness value of $f = \frac{a}{N}$, where $a$ is taken to be 10 and $N$ is the number of particles in the region. This encourages the optimiser to find solutions in regions with fewer particles, which increases the spread of the Pareto front. Once fitness values have been assigned, a roulette-wheel selection is performed which uses these fitness values to select a region from which a particle is then randomly selected to be is used as $REP(h)$.

### 5.4.3 Mutation

As the optimisation progresses, sometimes particle velocities will become too low to generate new and useful solutions as they get stuck in a local minima. Mutations can be used to increase the diversity of a swarm by allowing particles to escape local minima. Initially, there is a high degree of mutation which increases the swarm's exploitative nature; however, this decreases over time in favour of being exploitative as shown in Figure 5.9. The details of the method used can be found in [65].

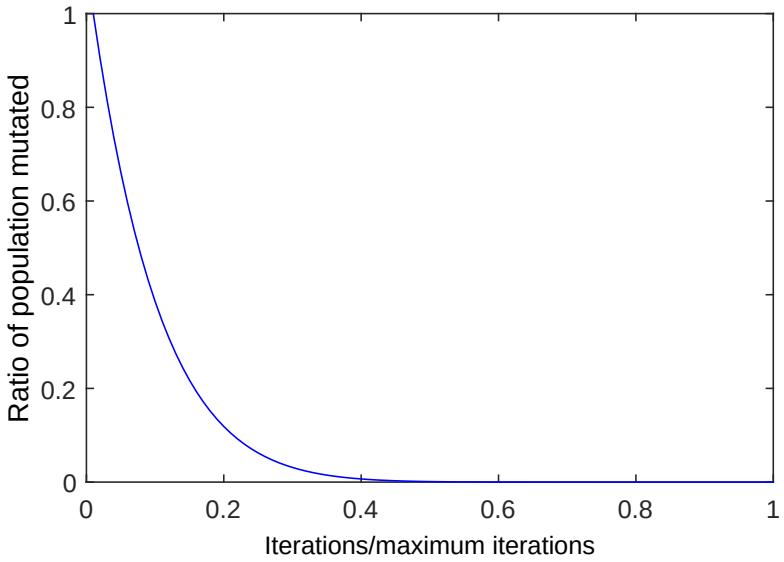


FIGURE 5.9: The ratio of particles in a swarm that are mutated depending on the current iteration.

### 5.4.4 Constraints

Constraints serve the dual purpose in optimisation to impose restrictions resulting from the definition of the problem and to limit the search space to a reasonable area. Eberhart [66] used the metaphor of watching spacecraft explore the Milky Way Galaxy in order to find a target known to be in the Solar System. In this instance, it makes sense to limit the search to be within the Solar System instead of using resources to search a space known to be invalid. The boundary constraint is imposed by setting the particle's position to be on the boundary that it exceeded, and then setting the particle's velocity to be in the opposite direction (multiplied by $-1$), which causes the particle to move back inside of the constrained search space.

The other type of boundary conditions are related to properties; for example, the power of the fan must be less than a specific value. In this case, constrained domination [67]

is used. This is applied by setting a maximum or minimum value and letting the particle with fewer constraint violations dominate. Figure 5.10 shows how constrained domination is applied.

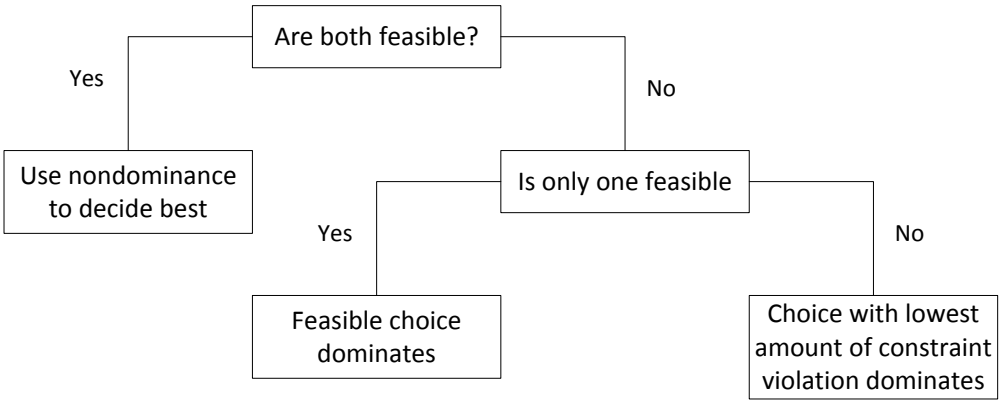


FIGURE 5.10: The scheme used to impose non-boundary constraints in MOPSO.

## 5.5 Constraints

The constraints in this project were dictated by the following performance targets set through consultation with an industry partner:

- Flow rate greater than 680 $m^3/h$
- Less noise than common commercially available pressed aluminium fans
- Minimised manufacturing costs (material and tooling)
- Operational speed of 1800 rpm
- Nominal fan diameter of 200 mm
- Fan is to be manufacturable using injection moulding
- Maximum fan power is 13 W

Although the flow rate, operational speed and diameter constraints are explicit, the other constraints were investigated and are explained in the following sections. The constraints are summarised below in Table 5.2.

### 5.5.1 Noise constraint

It is required that the new optimal fan design generates less noise than common commercially available pressed aluminium fans. A previous investigation into Air Drive pressed aluminium fans at the University of Canterbury [68] provided empirical data

| Constraint | Value |
|---|---|
| Flow rate | >680 $m^3/h$ |
| SWL | <65dBA |
| Operational speed | 1800 rpm |
| Nominal diameter | 200 mm |
| Thickness | $< \|0.25c\|$ |
| Chord | $< \frac{2\pi r_i}{N}$ |

TABLE 5.2: Summary of fan optimisation constraints.

for various speeds and blade angles. At the required operating speed, most blade angles produced between 65 dBA and 70 dBA. To ensure an increase in performance, the lower limit of 65 dBA will be chosen as the constraint for this project.

### 5.5.2 Manufacturing constraints

To limit the complexity of the mould, there should be no undercuts or inserts in the mould tooling. This imposes a constraint on the chord length depending on the radial position and the number of fan blades and is defined in equation 5.14.

$$c_{max,i} = \frac{2\pi r_i}{N}, \tag{5.14}$$

where $c_{max,i}$ is the maximum chord length at the radial position, $r_i$. The other important geometric constraint is the maximum thickness of the blade. This is important both for constraining the problem to a reasonable search space and so that the wall thickness of the blade does not have too high a variability, which can cause manufacturing issues. The blade thickness for this problem is to be constrained arbitrarily to $\pm 0.25c$. This will allow a minimum aspect ratio of 2 which ensured the search space was limited to plausible blade shapes.

### 5.5.3 Initialisation

In typical PSO problems, each particle is initially given a random position and velocity between the constraints. However, due to the complex nature of this project, this approach posed some issues. As there are 18 variables that control the shape of the fan blade, the majority of fan blades had aerofoils that XFOIL could not evaluate, which caused poor convergence. A better method of initialising each fan blade was to place the points randomly within the constraints with additional constraints that enforced an aerofoil shape. If viewing the upper surface of a typical aerofoil only, there is a clear trend for them to be convex. The lower surface is also typically convex although, in the case of a cambered aerofoil, the lower surface also has a concave section.

The top and bottom aerofoil surfaces must be generated separately to enforce the convex property and include camber. Fifty percent of aerofoils were randomly chosen to be cambered. The trailing edge points were fixed, and the leading edge points only had one degree of freedom, as shown in Figure 5.2. The method used to generate random aerofoils started by randomly selecting one of points 2-5 to be the highest point and then randomly selected $x$ and $y$ locations for this point subject to the constraints discussed in section 5.5. Next, the leading edge position was selected subject to the existing constraints with the additional constraint of $y_1 \in [0, y_{peak}]$. This resulted in a set of three random convex points at the leading edge, trailing edge and a point in-between. The remaining points were then each randomly selected and placed subject to the additional constraint of $y_i \in [y_{i-1}, y_{i+1}]$, where $y_{i-1}$ and $y_{i+1}$ were limited to assigned points only. The bottom aerofoil surface followed a similar process to the top surface, except that 50% of the aerofoils had a concave point. If camber were to be applied, point 10 as shown in Figure 5.2 was given a random point with the additional constraint of $y_{10} \in [0, y_{top}]$ where $y_{top}$ is the value of the top surface aligned with $x_{10}$. After this concave point was selected, the peak position was selected. Then, the leading edge position was selected, and finally all remaining points were placed to form a convex surface. All $x$ values were randomly assigned within the standard constraints. For clarity, an example of this process is shown in Figure 5.11.

This process successfully generated a wide range of random aerofoils. A random selection of initialised aerofoils is shown in Figure 5.12 which demonstrates the diversity of this method.

The twist and chord distribution control points were randomly assigned subject to the geometric constraints as this was sufficient to generate a reasonable variety of fan blades. In the case of cambered-plate cross-sections, randomly placed points generated geometries that have a high success rate in XFOIL. Therefore, no process to position the control points for the median camber line was required.

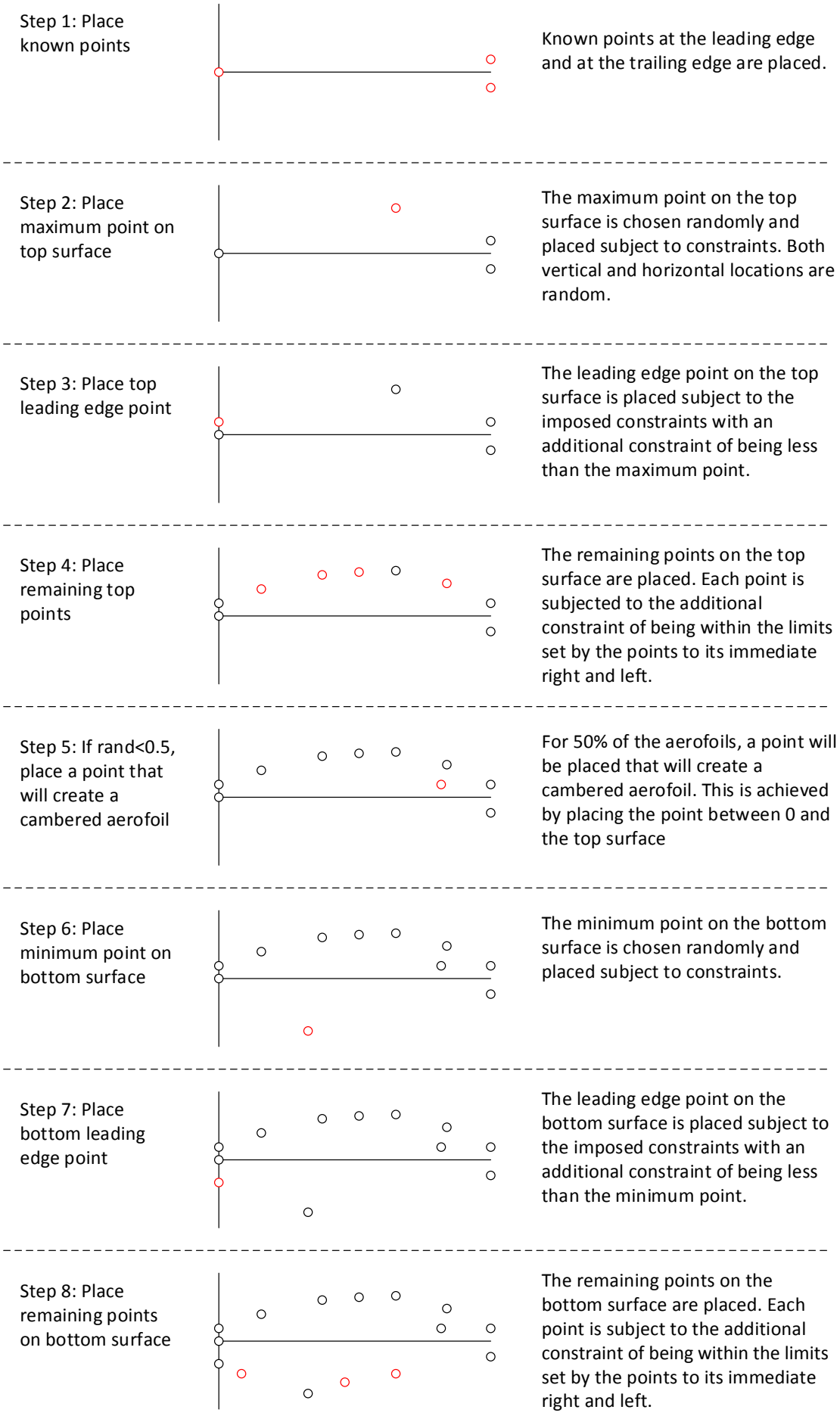


FIGURE 5.11: The process used to initialise fan blades' aerofoil shapes randomly.

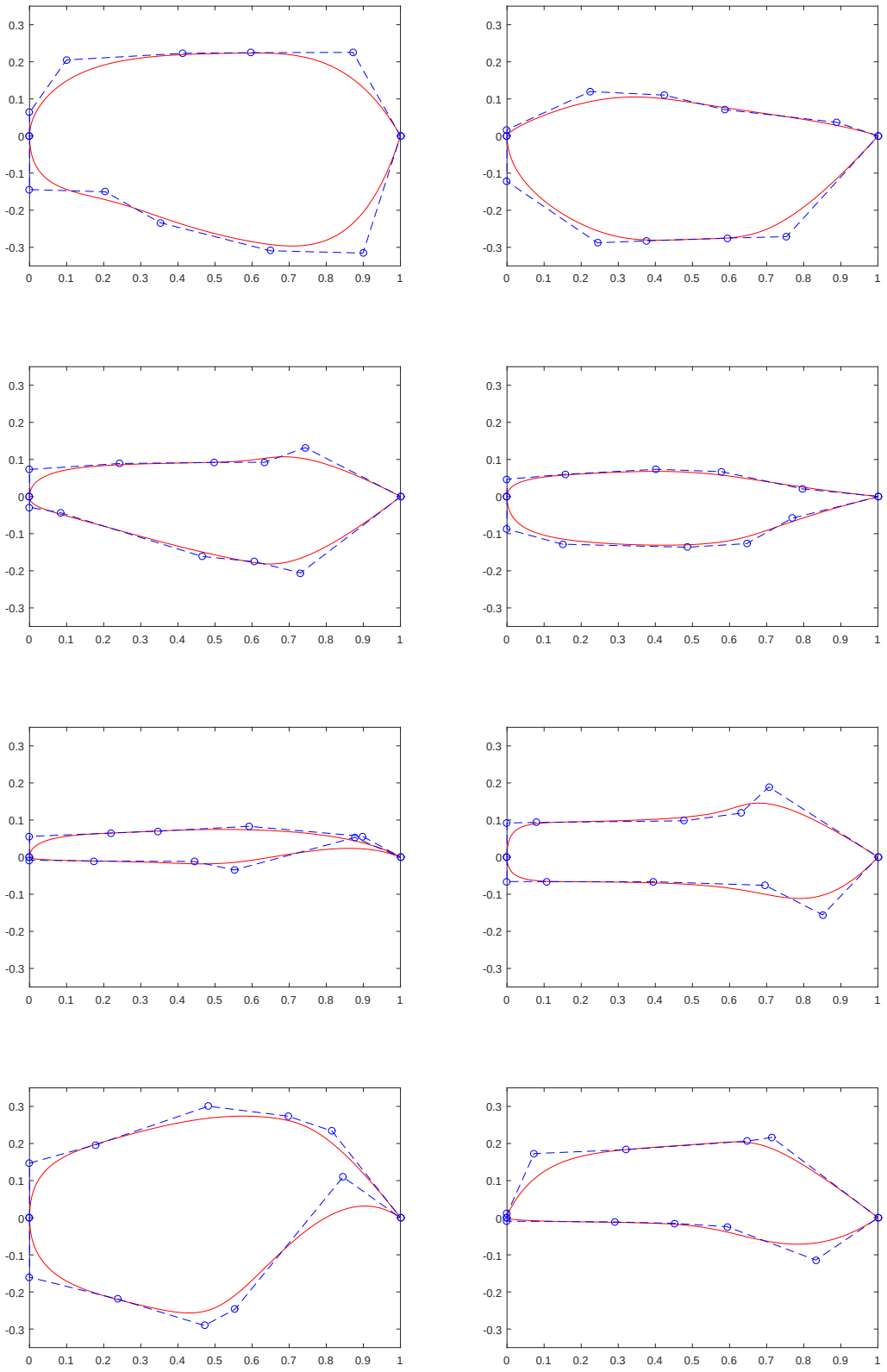

FIGURE 5.12: A variety of randomly generated fan blade cross-sections that show the diversity of this initialisation method.

# Chapter 6

# Optimal Fan Designs

The theory described in Chapters 3 to 5 has been implemented to generate optimal fan designs which are presented in this chapter. The optimal twist and chord distributions for a fan with a NACA0012 aerofoil cross-section blade are presented for validation purposes. Next, the optimal blade shape, twist and chord length for both a cambered-plate blade and aerofoil section blade are presented. All optimisations were performed under the same assumptions and operating conditions (presented in Table 6.1) and with the same geometric properties (presented in Table 6.2).

| Density | Kinematic viscosity | Speed of sound |
|---|---|---|
| 1.2250 kg m$^{-3}$ | $1.5 \times 10^{-5}$ m$^2$ s$^{-1}$ | 340m s$^{-1}$ |

TABLE 6.1: Operating conditions used in optimisation.

| $R_{min}$ | $R_{max}$ | Blades | $a_\infty$ |
|---|---|---|---|
| 30 mm | 100 mm | 5 | 1.25 |

TABLE 6.2: Geometric properties used in optimisation.

## 6.1 Optimisation of blade with NACA0012 cross-section

The twist and chord distributions for a blade with a NACA0012 cross-section was optimised for the purposes of validation. Because the BPM model uses empirical data from NACA0012 aerofoils, experimental tests on the NACA0012 fans were expected to give good correlation to the results predicted by the code developed in this work. Comparisons between the computational results presented here and the empirical results generated are presented in Chapter 8.

The optimisation presented here parameterises both the twist and chord along the length of the fan blade. As the lift coefficients, drag coefficients and the boundary layer parameters are well known and described algebraically in [17], this optimisation

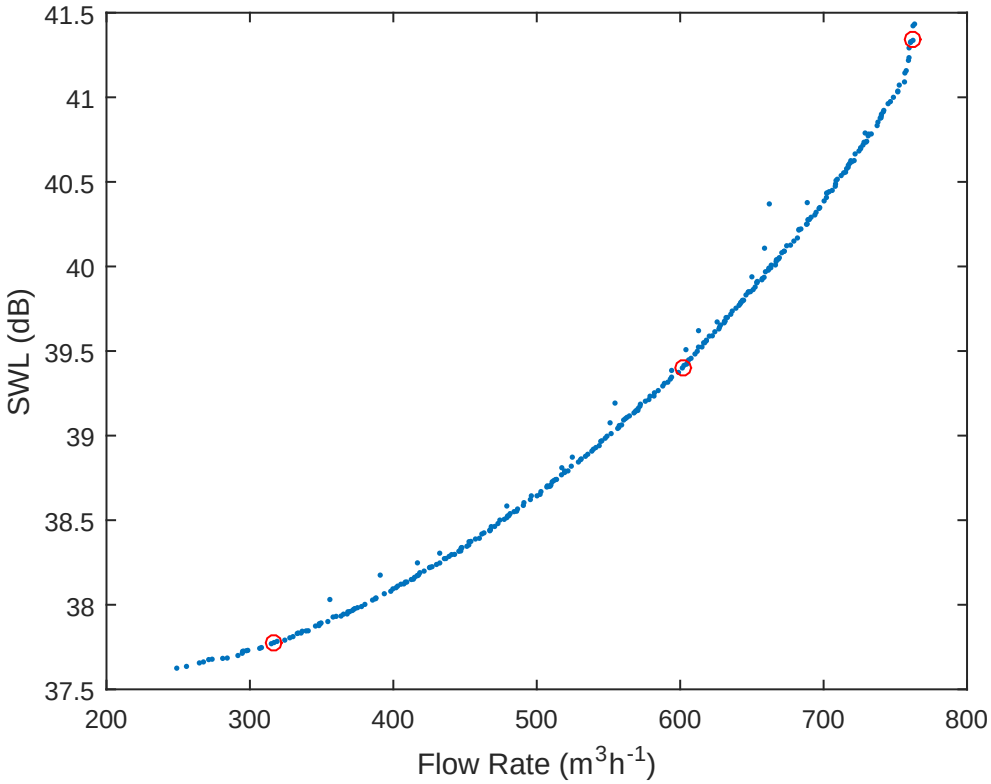


FIGURE 6.1: Pareto front from optimisation of twist and chord distribution for a NACA0012 cross-section blade. Red circles indicate the blades that were selected to be manufactured.

| **Blade** | 1 | 2 | 3 |
|---|---|---|---|
| **Flow rate ($m^3\,h^{-1}$)** | 762 | 602 | 317 |
| **SWL (dB)** | 41.0 | 39.4 | 37.8 |

TABLE 6.3: Predicted performance of NACA0012 blades chosen for experimental validation.

converged rapidly with very few particles failing to solve. The Pareto front for this optimisation is presented in Figure 6.1. For the purposes of validating the code over a wide range of operating conditions, three blade shapes were chosen at different positions on the Pareto front. These blades are shown in Figure 6.1 as red circles and have their shapes described in Figure 6.2 and Table 6.3.

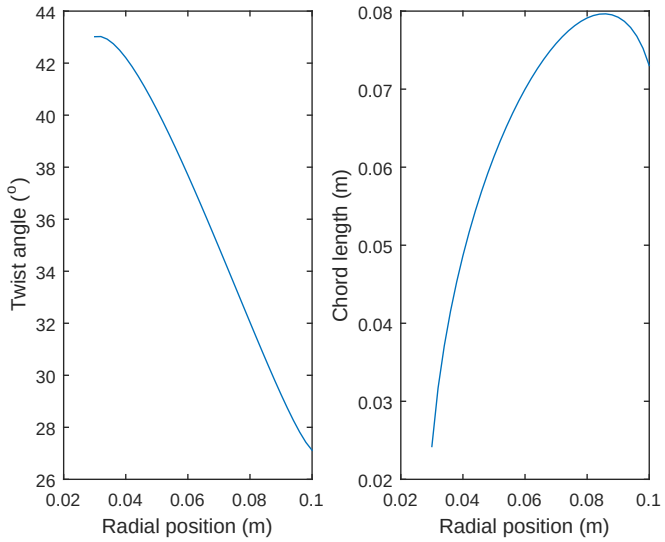


(A) Blade 1

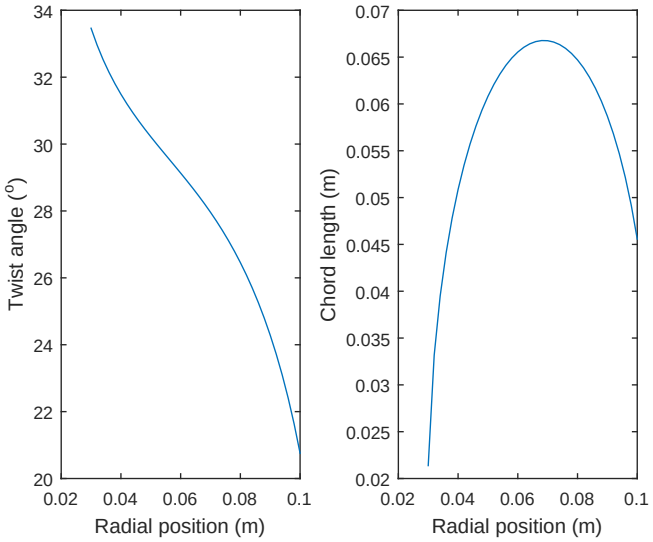


(B) Blade 2

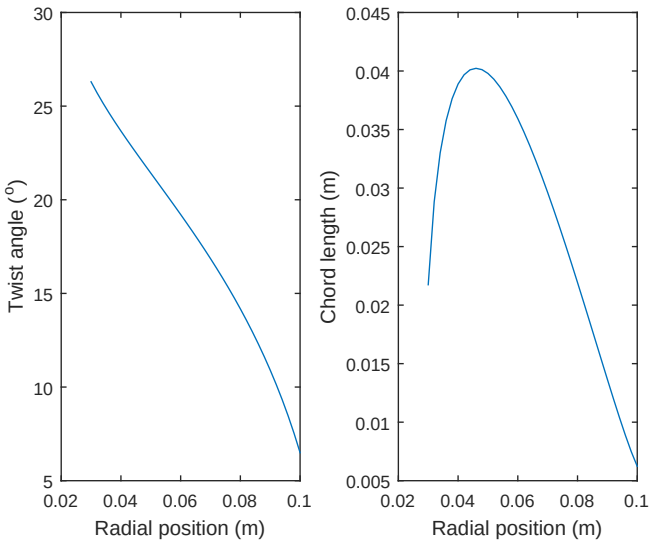


(C) Blade 3

FIGURE 6.2: Twist angle and chord distributions for NACA0012 blades chosen for experimental validation.

## 6.2 Optimisation of a blade with an aerofoil cross-section

The blade shape was optimised in addition to the twist and chord distributions in an attempt to increase the airflow and reduce the noise further. The aerodynamic properties of the blade were evaluated at the Reynolds number at the 75% radial position of the blade as this was considered most representative of the entire blade.

One blade shape was chosen from these results for experimental validation. Because of the dissimilarity between the profiles of the NACA0012 aerofoil used in the BPM model and the blades generated in the optimisation process, it was appreciated that the results may not correlate well. The Pareto front for this optimisation is shown in Figure 6.3 with the blade chosen for testing indicated with a red circle. The predicted performance of the chosen blade is in Table 6.4, the blade shape in Figure 6.4 and the twist and chord distribution in Figure 6.5. The Pareto front in Figure 6.3 shows a very rapid reduction in SWL for very little reduction in flow rate. Although the trend was expected, the slope of the Pareto front is significantly higher than what was expected. Furthermore, a close inspection of the blade shapes represented by each point in the Pareto front showed that there was very little difference between each blade. This indicates that the optimisation algorithm is exploiting a property in either the BPM model or in the prediction of the boundary layer properties in XFOIL.

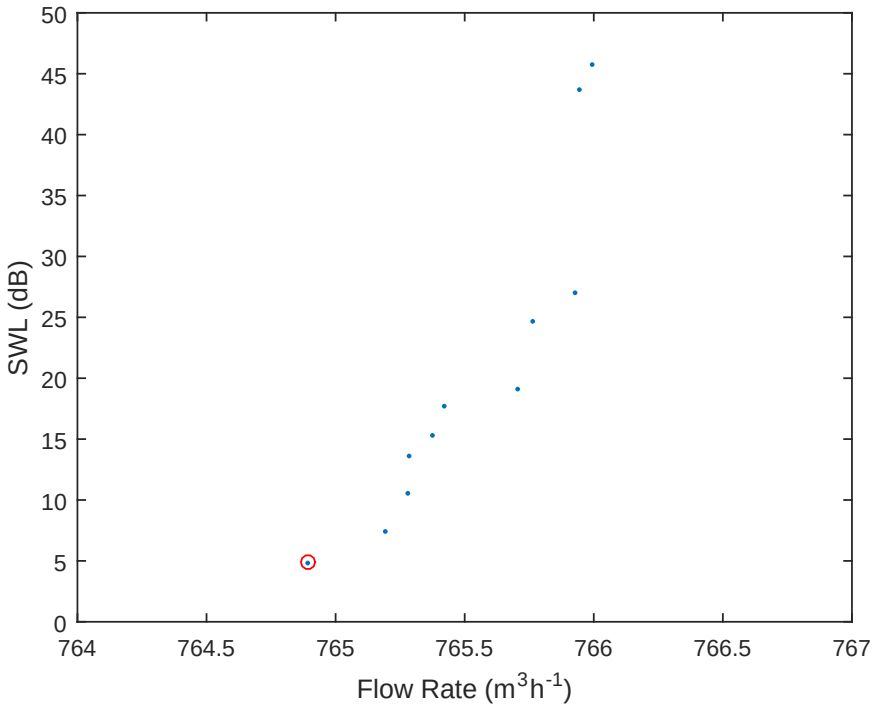


FIGURE 6.3: Pareto front from optimisation of the twist, chord and aerofoil cross-section. The red circle indicates the blade that was selected to be manufactured.

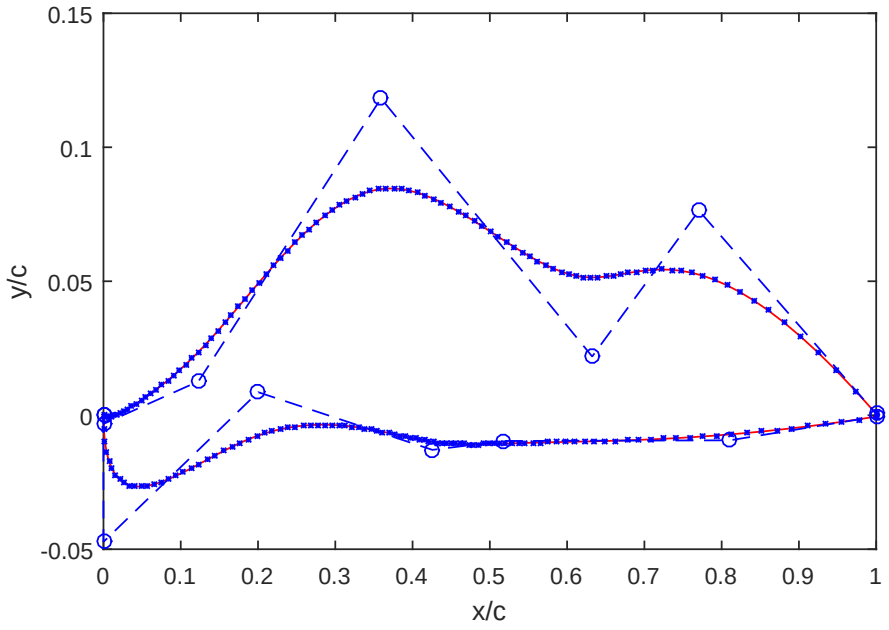


FIGURE 6.4: Shape of aerofoil blade chosen for experimental validation with control points shown by circles.

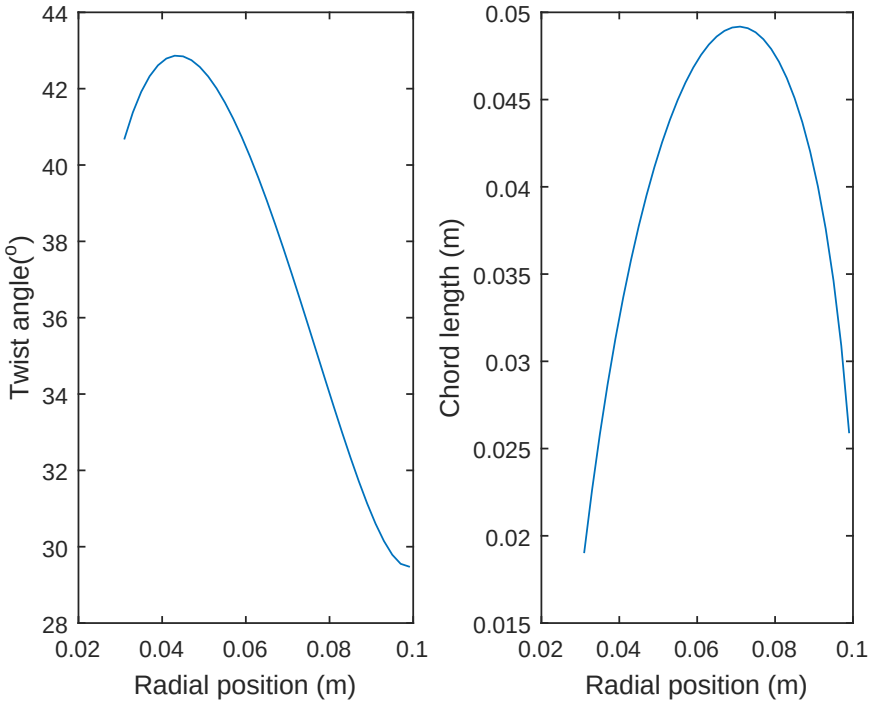


FIGURE 6.5: Twist and chord distribution of aerofoil blade chosen for experimental validation.

| **Blade** | 4 |
|---|---|
| **Flow rate ($m^3\ h^{-1}$)** | 765 |
| **SWL (dB)** | 4.8 |

TABLE 6.4: Predicted performance of the aerofoil blade chosen for experimental validation.

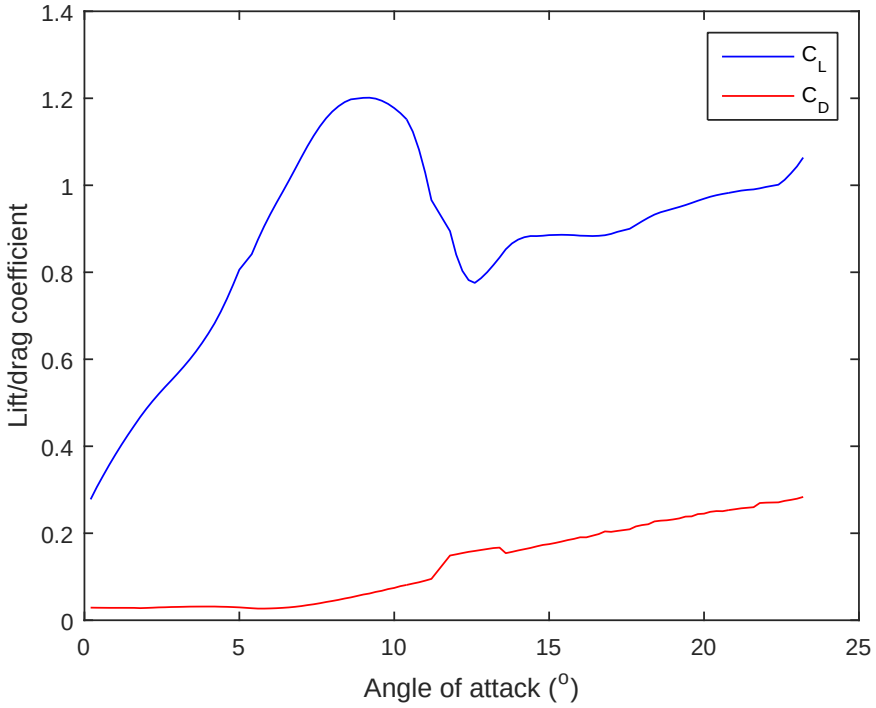


FIGURE 6.6: Lift and drag data for the chosen aerofoil blade profile at a Reynolds number of 50,000.

The lift and drag data for the aerofoil as predicted by XFOIL is in Figure 6.6. This aerofoil generates moderate lift and has a lift-to-drag ratio of 32.5 at stall which is less than that of the NACA0012 aerofoil.

## 6.3 Optimisation of a blade with a cambered-plate cross-section

Although fans with aerofoil cross-sections typically have superior performance to fans with cambered-plate cross-sections, cambered-plates are often favoured due to their lower material cost and less complex tooling. This optimisation used a single shaped cambered-plate with twist and chord distributions to generate an optimal design. There is a large dissimilarity of shape between the NACA0012 aerofoils from the BPM model and cambered-plates, so the BPM model was not expected to compare well to experimental results. Figure 6.7 shows the Pareto front from this optimisation. The point chosen for testing is indicated with a red circle, and the performance at this point is in

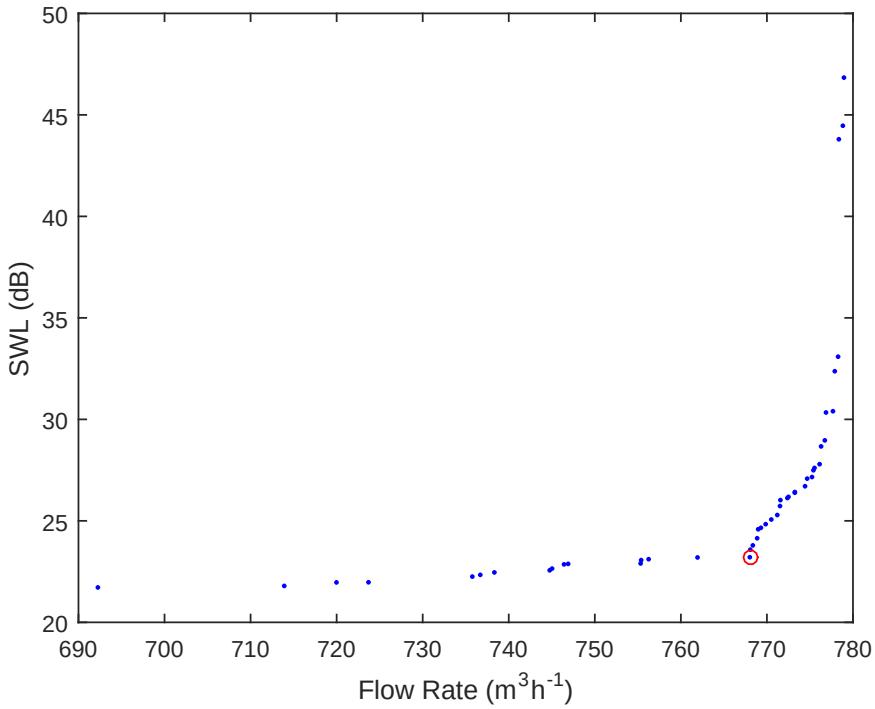


FIGURE 6.7: Pareto front from optimisation of the twist, chord and cambered-plate cross-section. The red circle indicates the blade that was selected to be manufactured.

| **Blade** | 5 |
|---|---|
| **Flow rate ($m^3\ h^{-1}$)** | 768 |
| **SWL (dB)** | 23.2 |

TABLE 6.5: Predicted performance of the cambered-plate blade chosen for experimental validation.

Table 6.5. This blade was chosen as particles in either direction resulted in either a steep reduction in flow rate or a steep increase in sound power. The shape of the optimal blade is shown in Figure 6.8 and the twist and chord distributions are shown in Figure 6.9.

The lift and drag coefficients for the cambered-plate predicted by XFOIL are presented in Figure 6.10. The cambered-plate generates high lift and has a lift-to-drag ratio of 34.7 at stall, which is good for a cambered-plate.

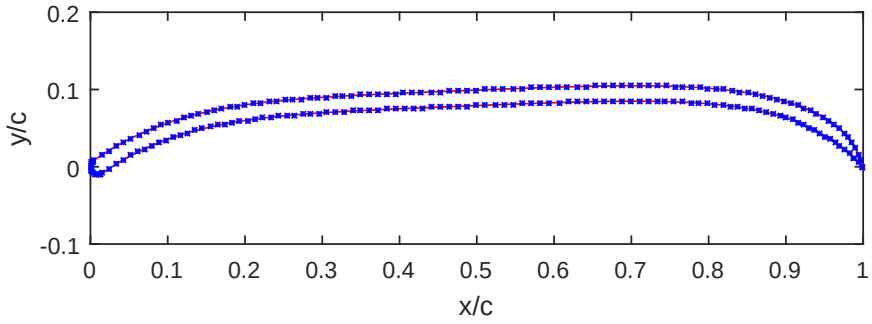


FIGURE 6.8: Shape of cambered-plate blade chosen for experimental validation.

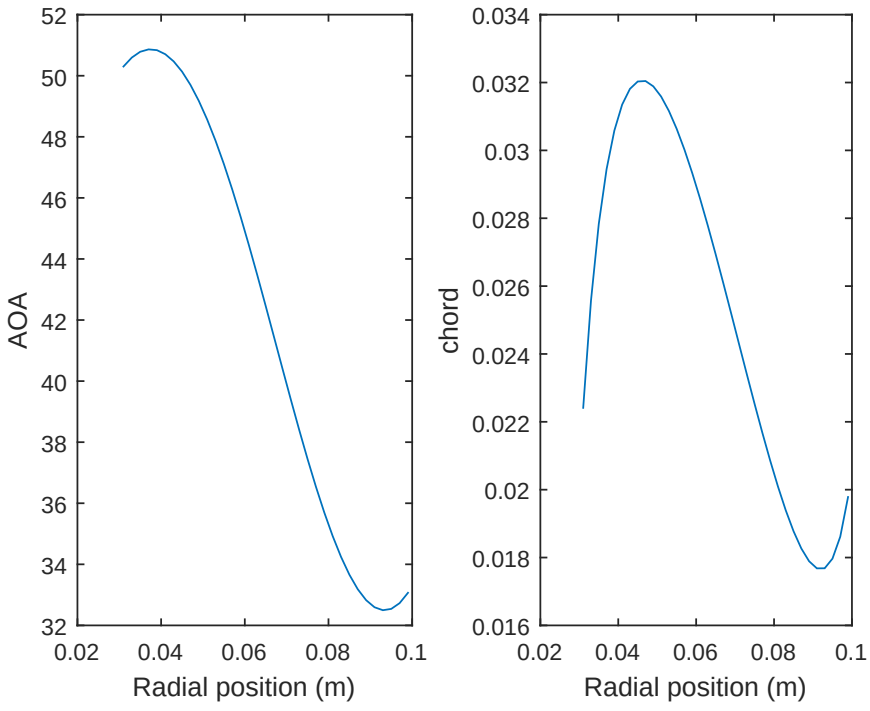


FIGURE 6.9: Twist and chord distribution of cambered-plate blade chosen for experimental validation.

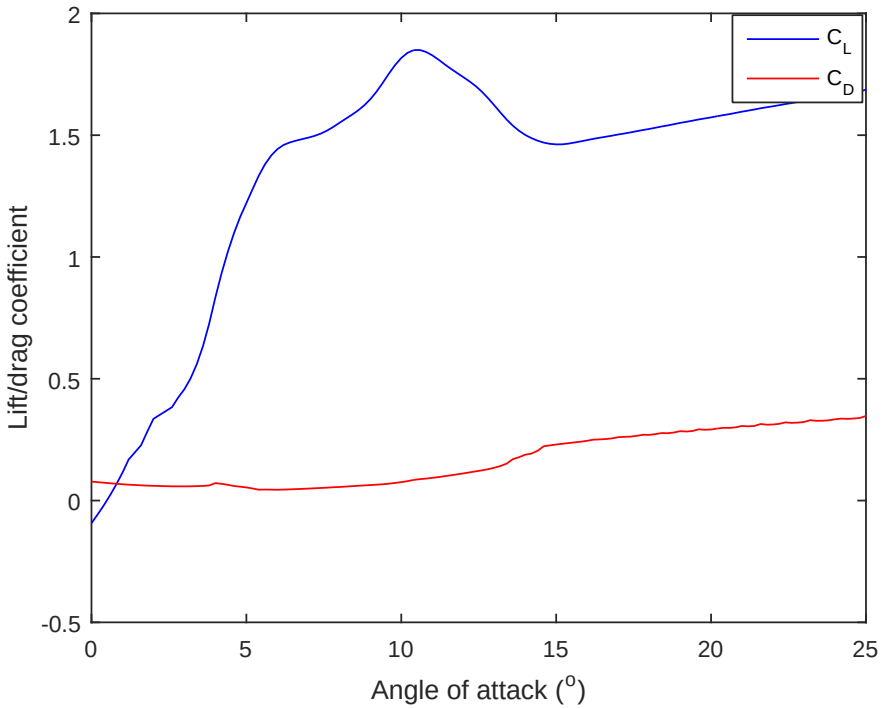


FIGURE 6.10: Lift and drag data for the chosen cambered-plate at a Reynolds number of 50,000.

## 6.4 Discussion on the optimisation

The run time of an optimisation is dictated by both the computational cost of calling the cost function and the number of calls of the cost function. Table 6.6 reports the solution times and total iteration for each of the blades. The times reported are only indicative as all simulations were run to their iteration limits as convergence criteria are difficult to set for MOPSO. The simulations were run on a computer with an Intel Core i7-4790 3.6 GHz processor and 16 GB of ram. The optimisation for blades 1-3 ran for more iterations than required for convergence to ensure a smooth and uniform Pareto front, with a high number of particles. All aerodynamic data used in the NACA0012 optimisations were calculated from curve fitted equations which resulted in fast and smooth evaluation of the cost function. The cambered-plate optimisation required calling XFOIL for each cost function evaluation, adding significant time to the optimisation. Furthermore, a penalty was applied to 34.5% of the cost function calls as

| Optimisation | Time | Total iterations |
|---|---|---|
| Blades 1-3 | 25 minutes | 2000 |
| Blade 4 | 8 days | 650 |
| Blade 5 | 7 days | 1000 |

TABLE 6.6: Optimisation solution times

the solver failed to solve, which negatively impacted convergence. The aerofoil blade optimisation also required calling XFOIL for each cost function evaluation. A penalty was applied to 51.9% of the function calls as the solver failed to solve, slowing convergence more than the cambered-plate optimisation. Furthermore, the time increase was compounded as there were more variables in this optimisation. This high failure rate is attributed to the generation of non-aerofoil shapes for which a solution could not be generated in XFOIL.

The aerofoil blade optimisation appears to have exploited the aeroacoustic prediction method. The predicted SWL is exceptionally low, and the blade shape is not a typical aerofoil shape. The small bump in the aerofoil acts as a boundary layer trip, which alters the boundary layer thickness in a way that exploits the relationships in the BPM model. This is a good indicator that the BPM model does not work well with dissimilar aerofoils although this will be verified in the experimental work in Chapter 8.

The optimisation was initially attempted with three aerofoil cross-sections with interpolation between these aerofoils. In a brief study of 1000 randomly generated aerofoils, it was found that only 40% of the blades generated solutions. This high failure rate resulted in poor convergence, and combined with the additional XFOIL calls, caused a significant increase in the time to run the optimisation. It should be noted that the aerofoils that generated a 40% failure rate were typically more aerofoil-shaped than many of the aerofoils generated by the optimisation process. Hence, if three cross-sections were used in an optimisation process, the failure rate would likely be greater than 60%. Using interpolation between three aerofoils would be more appropriate in a study that was searching for improvements on an existing blade (such as seeding the optimiser with an existing blade) as this would only make small changes and ensure that XFOIL can evaluate most aerofoils.

It was crucial to constrain the power or the torque of the fan as without this constraint the optimisation exploited BEMT's inability to predict the stall pressure. BEMT predicts the performance of a fan operating at 0 Pa where the optimal design for a fan has a very high blade angle. The tangential velocity of the blade is constant (determined by rotational speed), but the axial velocity increases for higher blade angles. Thus, the resulting vector of the airflow is at a high angle, similar to the blade, so stall does not occur. However, with the addition of resistance on the flow, the axial velocity would drop sufficiently, causing the aerodynamic angle of attack to increase; hence, the blade stalls, generating poor airflow and high noise. In addition to having poor stall pressure, fans with high blade angles have high power demands. Consequently the power was constrained in the optimisation.

The acoustic model does not account for the additional turbulence added by high blade angles as it views the acoustic contribution of the blade angle as only being from the aerodynamic angle of attack. Therefore, high blade angles will invalidate the acoustic

model. A better approach to modelling the effect of blade angle may be to use the geometric blade angle rather than the aerodynamic angle in the BPM model; however, this would limit the blade angle to 30 degrees as this is the highest stall angle incorporated in the BPM model.

# Chapter 7

# Experimental Facility

This chapter describes the experimental facility used for testing the axial flow fans developed for this project. The test facility used meets ISO 10302-1 [69] and allows for measurement of the sound power level, total fan pressure, air flow rate, fan power and the fan speed. The chapter also details modifications to the ISO 10302 test rig to assist in the isolation of fan self-noise from other mechanical and aerodynamic noise sources.

## 7.1 Test Environment

At the time of testing, the University of Canterbury's mechanical engineering laboratories were unfortunately being upgraded, therefore, an alternative facility had to be used. A rural 15x20x5 m warehouse was used for all testing which provided a large space with low background noise levels. The acoustic performance of the room was improved by partially lining the lower portion of walls with acoustic absorption. Three 3.6 x 1.2 m sheets of 25 mm medium density fibre board were placed on the floor to create a reflecting plane on which all testing was performed.

The test space was qualified with an absolute comparison test, as described in Annex A.2 of ISO3744 [70]. The one third octave band SWL of an ISO 6926 [71] compliant Acculab RSS350 reference sound source was measured in the test location. The room correction factors (K2) were calculated as the difference between the measured and reference SWL. The absolute value of the K2 factors were less than 4 dB in all frequency bands as required by ISO3744 [70].

The background noise level of the test space was at least 10 dB below the measured SPL of the fans for all measurements; therefore, no correction was made for background noise.

## 7.2 Fan Test Rig

The test rig was developed at the University of Canterbury and conforms to ISO 10302-1: Acoustics – Measurement of airborne noise emitted and structure-borne vibration induced by small air-moving devices [69]. ISO 10302 details a test methodology and test rig that can be used to measure the sound power, flow rate and total fan pressure of an axial flow fan. The test rig has a variable size outlet, which allows for control over the resistance on the fan. For additional details than below, including the qualification of the test rig to ISO10302, see McKinlay (2014) [68].

The main component of the test rig is the chamber, shown in Figure 7.1, which is a 800 x 800 x 600 mm cuboid constructed from aluminium sections and 50 $\mu$m polyester film. The polyester film is used to form an acoustically transparent, air tight chamber. Qualification of the chamber showed that the chamber meets the insertion loss requirements described in ISO 10302 [69].

FIGURE 7.1: Fan test rig chamber.

The test rig has a variable sized outlet to control the aerodynamic load on the fan. This was implemented using a steel sheet slider, as shown in Figure 7.2.

The inlet of the test rig has a mounting panel constructed of rubber sheet to dampen the vibrations from the fan to the frame. Attached to the rubber is a steel sheet with mountings for a 200 mm fan shroud. Inside the chamber, adjacent to the rubber mounting panel, is a 6 mm nylon hose with four 1.5 mm pressure taps. The hose is connected to a pressure transducer to measure the total fan pressure. The mounting panel and pressure ring are shown in Figure 7.3.

FIGURE 7.2: Fan test rig chamber outlet. Figure reproduced from [68].

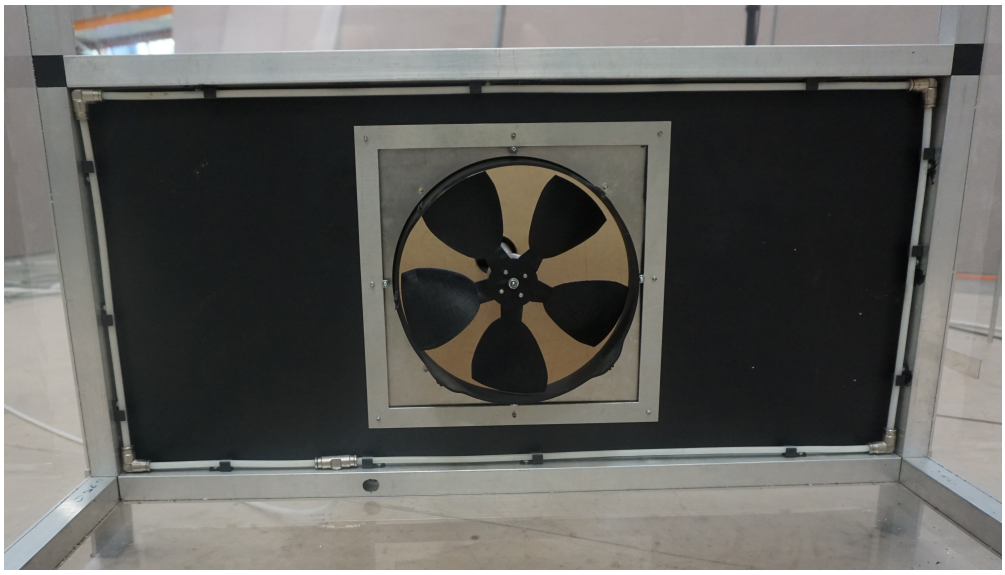

FIGURE 7.3: Fan test rig chamber mounting panel and pressure ring.

## 7.3 Instrumentation

The pressure, speed and torque instrumentation was connected to a National Instruments (NI) USB-6009 data acquisition system and controlled using the NI LabView software.

### 7.3.1 Speed measurement

The fan was powered using a Maxon EC90 flat 90 W brushless DC motor in conjunction with a Maxon ESCON 50/5 motor controller. The Maxon EC90 motor had inbuilt hall sensors which assisted in the accurate control and measurement of the rotational speed of the fan.

### 7.3.2 Pressure and flow rate measurement

The previously discussed pressure ring in the chamber was connected to a Dwyer MS 321 differential pressure transducer to measure the total fan pressure.

The flow rate was correlated with the total fan pressure and the outlet area using a series of hot wire anemometer measurements over the outlet at various sizes. This work showed the correlation to be

$$Q = 1.0233 A \sqrt{p}\ \mathrm{m^3 s^{-1}}, \tag{7.1}$$

where $Q$ is the flow rate, $A$ is the outlet area and $p$ is the total fan pressure. The correlation is shown in Figure 7.4 and has a coefficient of determination of 0.9965.

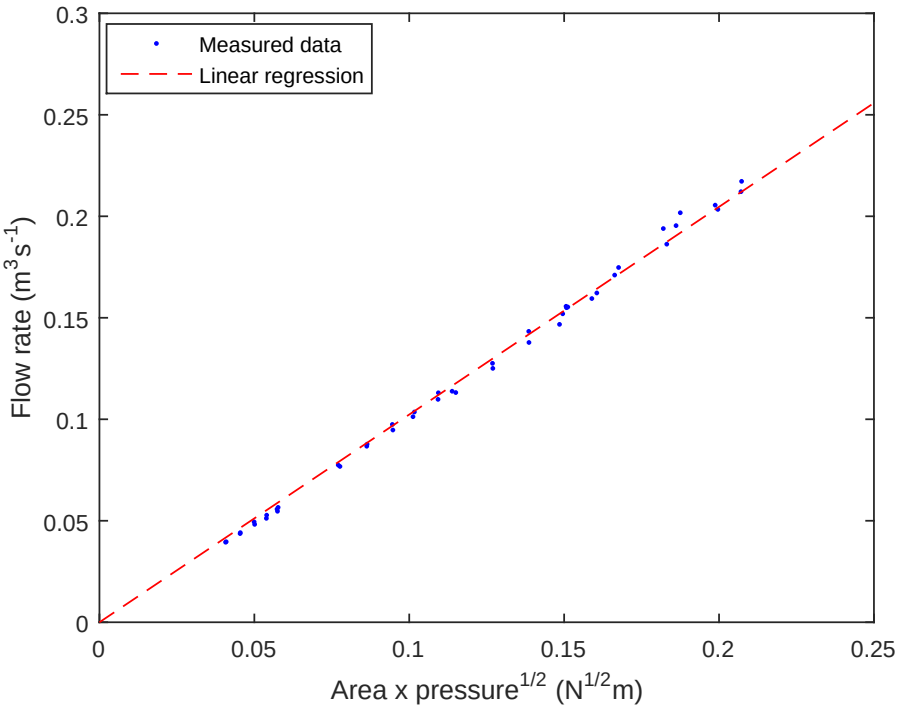


FIGURE 7.4: Flow rate data from measurements taken in [68] showing the regression between flow rate, outlet area and pressure for the ISO 10302 test rig.

### 7.3.3 Torque and power measurement

The shaft torque measurements were made using a strain gauge that was calibrated with a known load. A TorqueTrak 10K telemetry system was mounted to the shaft to allow for contactless transmission of the strain gauge measurements to the NI data acquisition system.

The shaft power was calculated as

$$P_{shaft} = \tau\omega, \tag{7.2}$$

where $P_{shaft}$ is the shaft power, $\tau$ is the measured torque and $\omega$ is the rotational speed of the shaft. Assuming that the flow was incompressible allowed for the efficiency of the fan to be calculated as

$$\eta = \frac{pQ}{P_{shaft}}, \tag{7.3}$$

where $p$ is the measured pressure and $Q$ is the calculated flow rate.

### 7.3.4 Acoustic measurement

The SWL of the fans was measured in accordance with ISO 3744: Acoustics – Determination of sound power levels of noise sources using sound pressure – Engineering method in an essentially free field over a reflecting plane [70]. The SPL was measured simultaneously at 10 microphone locations on a 1.4 m radius hemisphere over a reflecting plane. The location of the reflecting plane, the microphones and the fan test rig are shown in Figure 7.5.

The microphones were mounted in holders attached to 10 mm aluminium rods which were inserted into holes drilled into the reflecting plane. The microphones used were Brüel and Kjær type 4189 $1/2$" microphones with built-in pre-amplifiers. Wind shields were fitted for all measurements and accounted for in the $K2$ correction factor. All of the microphones were connected to a 17 channel Brüel and Kjær Pulse analyser. All SPL measurements were 30 second averages from which the SWL was calculated using

$$L_w = L_p + 20\log r_e + 8dB. \tag{7.4}$$

The reference distance ($r_e$) was 1.4 m, and the 8 dB factor accounts for the measurements being taken over a reflecting plane.

### 7.3.5 Turbulence generation and measurement

Quantification of turbulence at the inlet is important to identify IT noise. In this study, hot wire anemometer measurements were taken at 9 radial positions in front of the fan to measure the velocity of the time variant flow. A Dantec 54N81 multi-channel constant temperature anemometry system with one single wire type 55P11 probe (5 µm diameter, 1.25 mm tungsten wire) was used. The probe measured the flow velocity in the axial direction at 50 kHz from which the turbulence could be calculated. It was assumed that the flow was circumferentially invariant but radially variable; therefore,

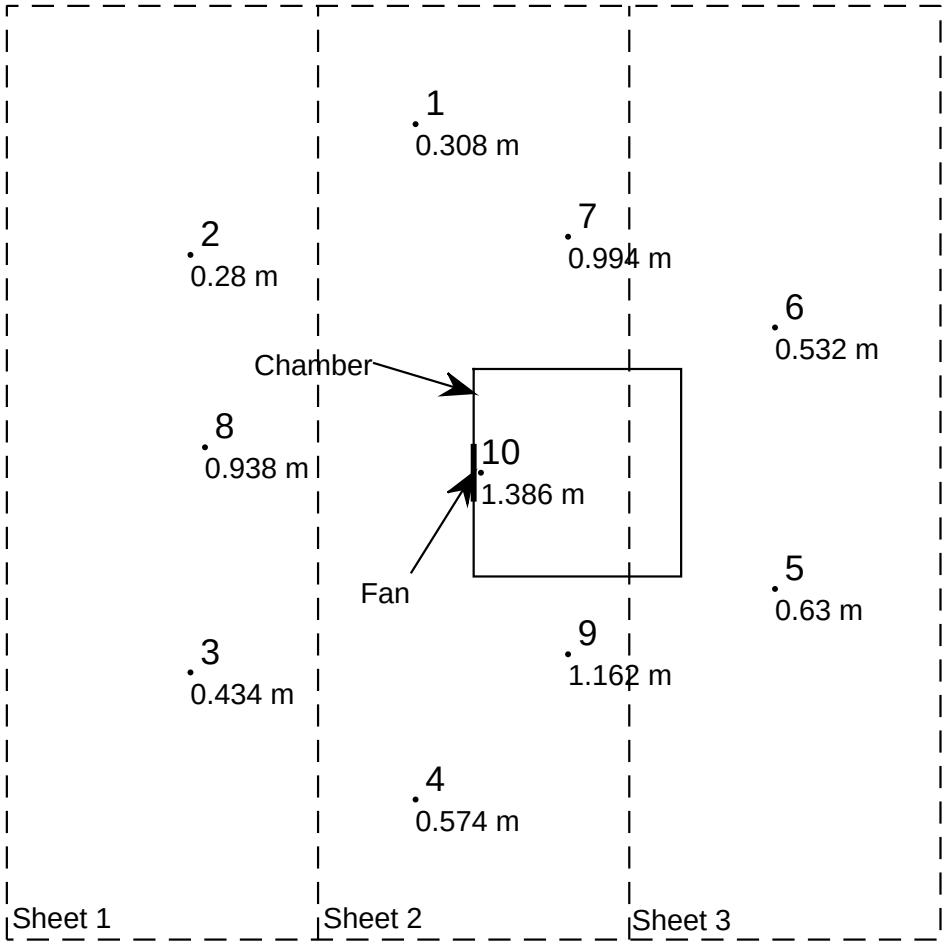


FIGURE 7.5: A plan view of the microphone locations and fan test rig chamber on the reflecting plane to scale. The height of the microphone above the reflecting plane is the value below the microphone number.

the hot wire probe measurements were taken at 9 equispaced locations between the root and the tip 10 mm from the fan.

Once the flow velocities had been measured, they were decomposed into a time averaged velocity ($\bar{v_x}$) and the fluctuating component ($v_x(t)'$). Thus, the turbulence intensity was calculated as

$$I_{turb} = \frac{\sqrt{\bar{v_x'^2}}}{v_x}. \tag{7.5}$$

The turbulence integral length was calculated using the method described in [72] which assumes Taylor's hypothesis ($\frac{\partial}{\partial t} = -\overline{v_x}\frac{\partial}{\partial x}$). As the inlet flow for an axial flow fan is predominantly 1-dimensional, Taylor's hypothesis was considered valid. The autocorrelation function ($R_{xx}$) is given by

$$R_{xx}(\tau) = \frac{\int_0^{\Delta T} v_x(t)' v_x(t+\tau)' dt}{\int_0^{\Delta T} v_x^2(t)' dt}, \tag{7.6}$$

where $\tau$ is the lag time and $\Delta T$ is a large component of the period of the lowest frequency component of the signal with significant amplitude. The integral length scale is then calculated as

$$\Lambda_x = \bar{v_x} \int_0^\infty R_{xx}(\tau) d\tau. \tag{7.7}$$

In practise, the integral is performed from $\tau = 0$ to the value at $\tau$ which $R_{xx}$ first became zero rather than from 0 to $\infty$.

## 7.4 Fan test rig modifications

The original ISO 10302 [69] test rig limits the ability to identify noise sources as the motor and fan-support interaction cannot be removed. This section details the modifications to the ISO 10302 test rig that significantly reduced the motor and fan-support interaction noise below other noise sources.

To reduce the motor noise, the motor must be moved away from the fan and enclosed in a box with acoustic treatment. To prevent the motor enclosure from impeding the airflow to the fan or generate additional turbulence, the enclosure should be located a sufficient distance away from the fan. Additionally, the enclosure should be well outside the microphone hemisphere so that it does not interfere with the sound field. The easiest method of transferring the power from the motor to the fan is through a long shaft. An adequately stiff and well supported shaft can overhang a bearing, which will additionally allow for the removal of fan supports.

### 7.4.1 Shaft design

Long and slender shafts can be dynamically excited. To prevent dynamic excitation, adequate shaft support and stiffness is required. However, a larger shaft will increase the inertia of the system which will possibly require a larger, and potentially, nosier motor. Furthermore, a larger diameter shaft will be more likely to generate turbulence.

The final design, shown in Figure 7.6 uses a 1.5 m long shaft. The shaft is 25.4 mm diameter steel tube of 3 mm wall thickness. Tube was used to increase the moment of inertia of the section without significantly increasing the weight of the shaft. The critical frequencies of this shaft were predicted using the Rayleigh-Ritz method to ensure that the first critical frequency of the shaft was outside of the operational range. The final design, as shown in Figure 7.6, has an overhanging shaft which allowed for the fan supports to be removed. This design balances the natural frequency of the overhanging section of the shaft and the fully supported section of the shaft and limits the the operational speed of the shaft to 2100 rpm. The existing motor had insufficient torque to overcome the additional system resistance and additional rotational inertia and so

the original Maxon EC45 flat 70 W motor was replaced with a Maxon EC90 flat 90 W motor.

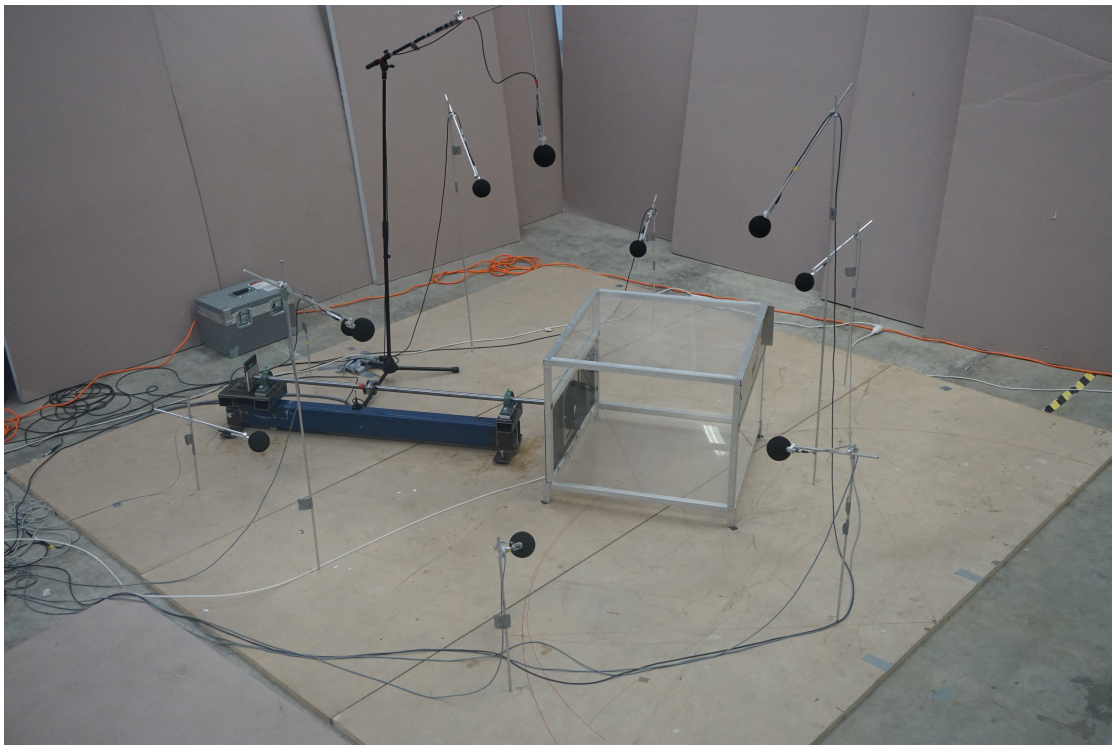

FIGURE 7.6: Modified fan test rig.

### 7.4.2 Shaft power measurement

An additional benefit of using a larger shaft is that it can be strain gauged which allows for accurate measurements of the shaft power, rather than only the motor power. Measuring the shaft power directly means that the total fan power and fan efficiency can be calculated. Previously, the test rig could only calculate the combined efficiency of the fan, which was a limitation of the ISO10302 [69] method. Additionally, using a moderate sized shaft allows for the strain gauge to be connected to a radio telemetry system which allows for easy instrumentation of the shaft. The strain gauge was calibrated to measure torque by applying a known torque to the shaft.

The resistance from the bearings was expected to contribute to the torque in the shaft measured by the strain gauge. To minimise the contribution from the bearings to the measured torque, unsealed bearings with a light oil were used to minimise friction. The torque from the bearings was subtracted from the shaft torque measurements to provide the fan torque. Table 7.1 shows the resistive torque from the bearings.

| Speed (rpm) | Torque (Nm) |
|---|---|
| 1200 | 0.064 |
| 1500 | 0.095 |
| 1800 | 0.138 |
| 2100 | 0.221 |

TABLE 7.1: Resistive torque on the shaft from the bearings.

### 7.4.3 Shaft noise

A Brüel and Kjær type 3599 sound intensity probe was used to take point measurements at various locations over the test rig, which are superimposed in Figure 7.7A, to assist in identification of the noise sources. These measurements show that the strain gauge telemetry system generates significant noise with the motor and bearings also contributing. As the main noise source could not easily be reduced and the noise emitted by the modified test rig was significant (SWL 65 dBA at 1800 rpm), acoustic enclosures were constructed to minimise the noise. Figure 7.7B shows that the acoustic enclosures block a significant amount of fan rig noise; however, there is still some low frequency noise from vibrations being emitted at the base, some noise leaking through the joint between the two boxes, and from the shaft's hole.

The enclosures shown in Figure 7.8 used 18 mm medium-density fibreboard lined with 6 kg m$^{-2}$ mass loaded vinyl barrier and 50 mm acoustic absorption. The acoustic enclosures reduced the noise from the modified test rig to approximately 55 dB at 1800 rpm, which is about 10 dB below the noise emitted by any of the tested fans.

The enclosures around the shaft and motor introduced a large reflective surface close to the fan. To account for this, the reference sound source was measured with the box in position. From these measurements, an updated K2 correction factor was calculated and is shown in Figure 7.9. The updated K2 values show that the enclosure has minimal influence as the K2 values are still within the limits specified in ISO3744 [70].

The modifications to the existing test rig were intended to eliminate any requirement to consider the motor noise as well as allow for the removal of the motor support struts. Motors generate noise proportional to both the rotational speed and loading which makes correcting the recorded sound power difficult. Although the modified rig removes the motor noise, it introduces potential bearing noise; however, the bearing noise is expected to be proportional to the rotational speed only. To verify the performance of the modified test rig, the sound power was measured at 1200, 1500, 1800 and 2100 rpm. A 0.3 N m frictional load (similar to the load applied by a fan) was applied to the shaft inside the enclosure to simulate loading without introducing significant noise. The results from the tests are presented in Figure 7.10 and show that the noise generated by the test rig is low and only dependant on the operational speed. If the noise generated by the rig is within 10 dB of a measured fan, then a correction, $K_3$, was

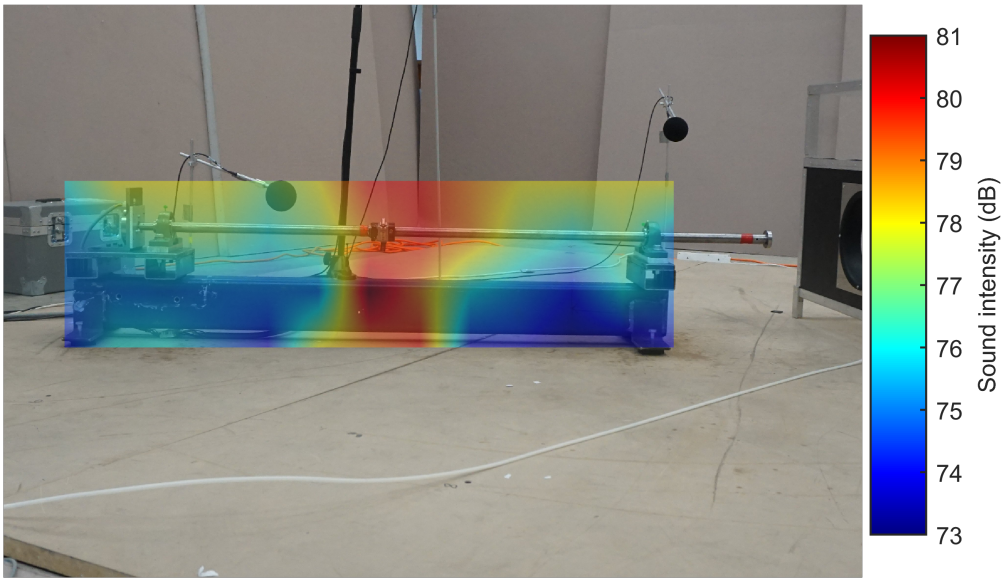


(A) Test rig

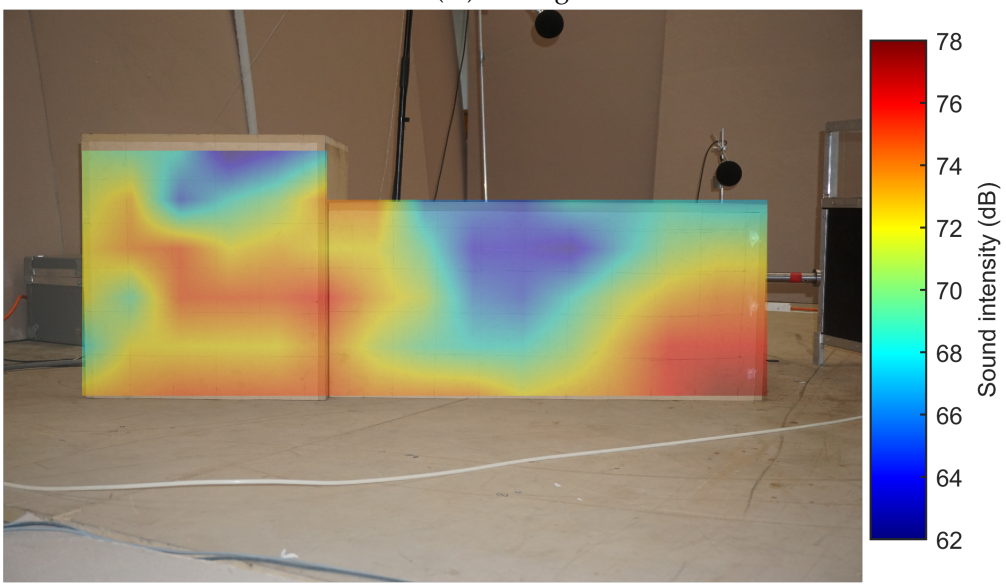


(B) Enclosure

FIGURE 7.7: Sound map of the modified test rig and enclosure.

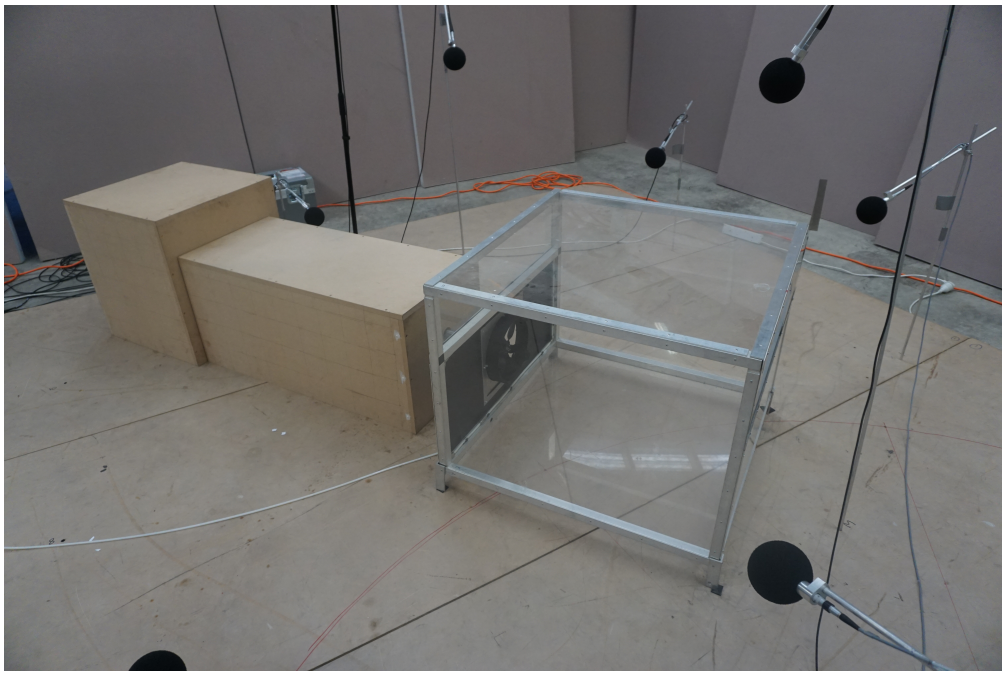

FIGURE 7.8: Modified test rig's acoustic enclosure. The enclosures are constructed from 18 mm medium-density fibreboard lined with 6 kg $m^{-2}$ mass loaded vinyl barrier and 50 mm acoustic absorption.

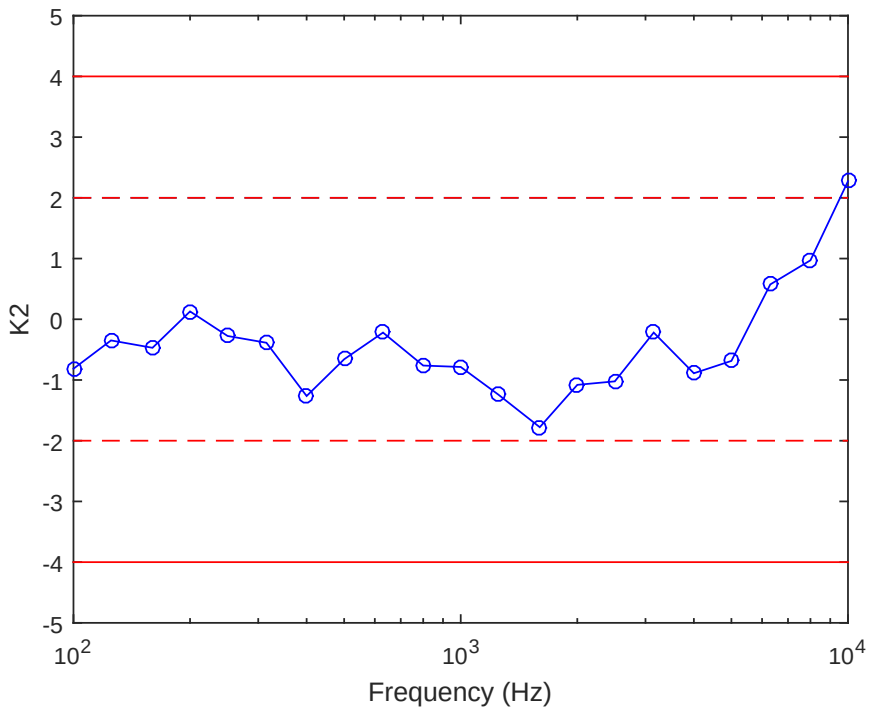


FIGURE 7.9: Correction for the enclosure's influence on the acoustic field and room effects. The red dashed lines indicate the preferred region for K2, and the solid red lines indicate the required limits for K2.

applied as

$$L_{w_{fan}} = L_{w_{measured}} - K_3, \tag{7.8}$$

where $K_3$ is defined as

$$K_3 = -10\log(1 - 10^{\frac{\Delta L}{10}}), \tag{7.9}$$

and $\Delta L$ is the difference in SWL at each frequency band.

The sound power levels in third octave bands for each speed can be found in Appendix B.

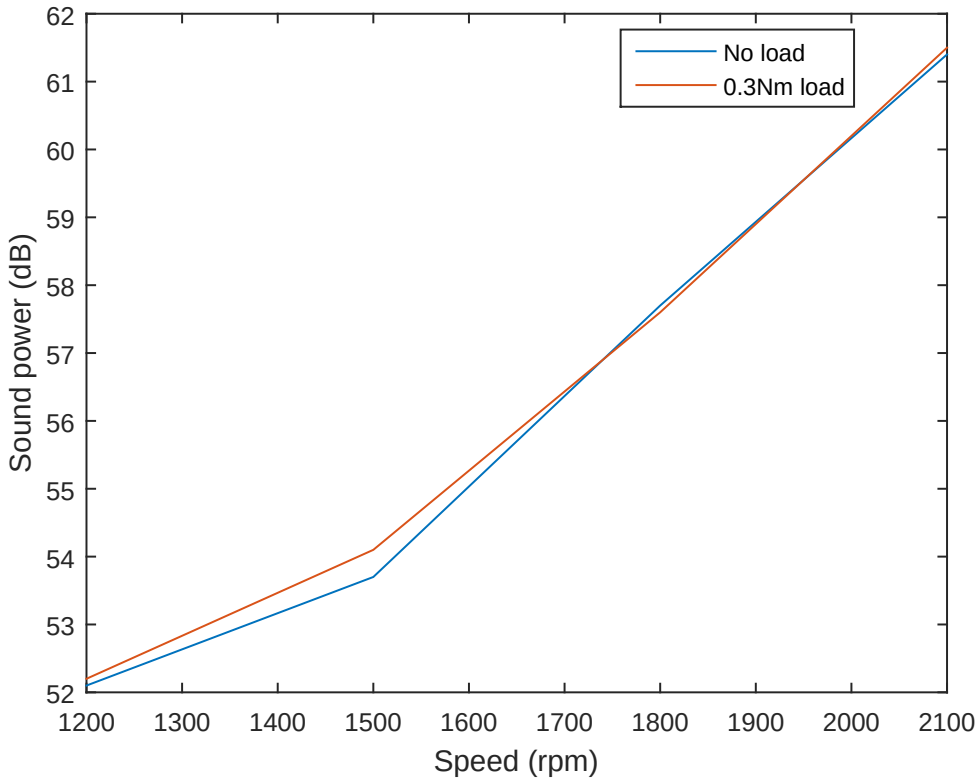


FIGURE 7.10: Acoustic performance of the modified test rig at various speeds and loads.

### 7.4.4 Aerodynamic effects of enclosures

The use of enclosures has potential aerodynamic implications by altering the fan inflow conditions and inducing turbulence incident on the blades. To determine the aerodynamic effect of the enclosure, hot wire measurements were taken over a plane at the height of the shaft from the root to the tip of the fan with and without the enclosures present. The mean axial velocity over the plane is shown in Figure 7.12, and the axial turbulence intensity is shown in Figure 7.11.

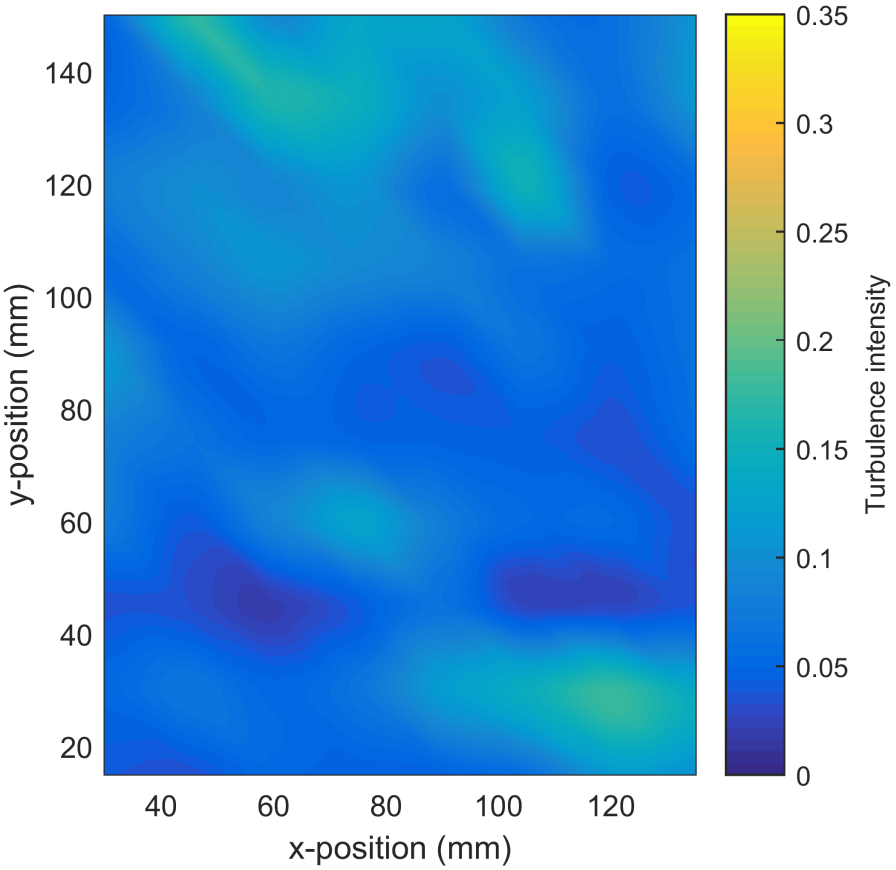


(A) No enclosure

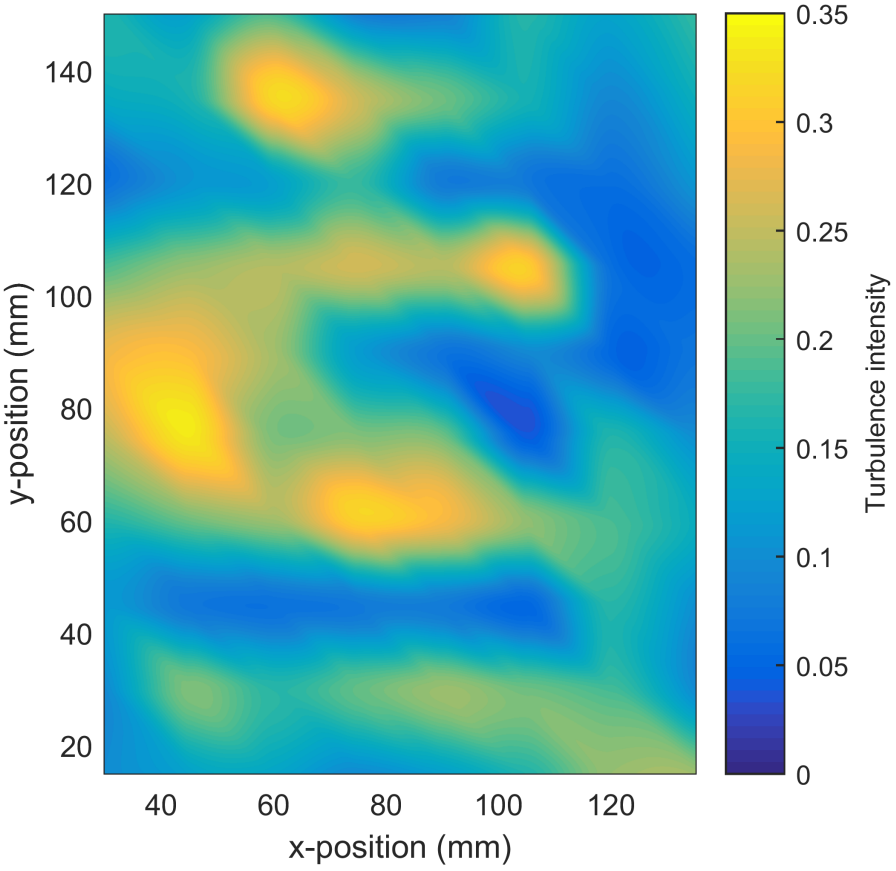


(B) Enclosure

FIGURE 7.11: Effect of the enclosure on the turbulent intensity in a plane parallel to the ground at the height of the shaft. The centre of the fan is located at $x = 0$ mm, and $y = 0$ mm and the fan runs in the x-plane.

Figures 7.11 and 7.12 show that enclosure has an aerodynamic effect on the inflow by both reducing the axial velocity and increasing the turbulence. This effect is expected as the flow now must be drawn more radially into the fan rather than axially, as the path parallel to the fan is now blocked by the enclosure. The increase in radial flow is shown by the decrease in the measured axial flow without a decrease in the total flow rate, by considering the continuity of the inflow. Additionally, as the flow passes over the enclosure, turbulence is induced. This is seen with higher turbulence at locations close to the box through to the fan. The increased turbulence will increase the IT noise; however, the turbulence at the very entrance to the fan is not significantly higher as some of the turbulence from the enclosure appears to have dissipated before it reaches the fan. Additionally, the most intense turbulence is in the $y = 30$ mm to $y = 60$ mm region, which is close to the hub. The noise generated by the hub is minor compared to the noise generated by the tip as the Mach number at the hub is proportionally low.

Interestingly, the tip region has moderate turbulence independent of the box. As the tip of a fan has the highest Mach number, turbulence ingested by this region of the blade could cause significant noise.

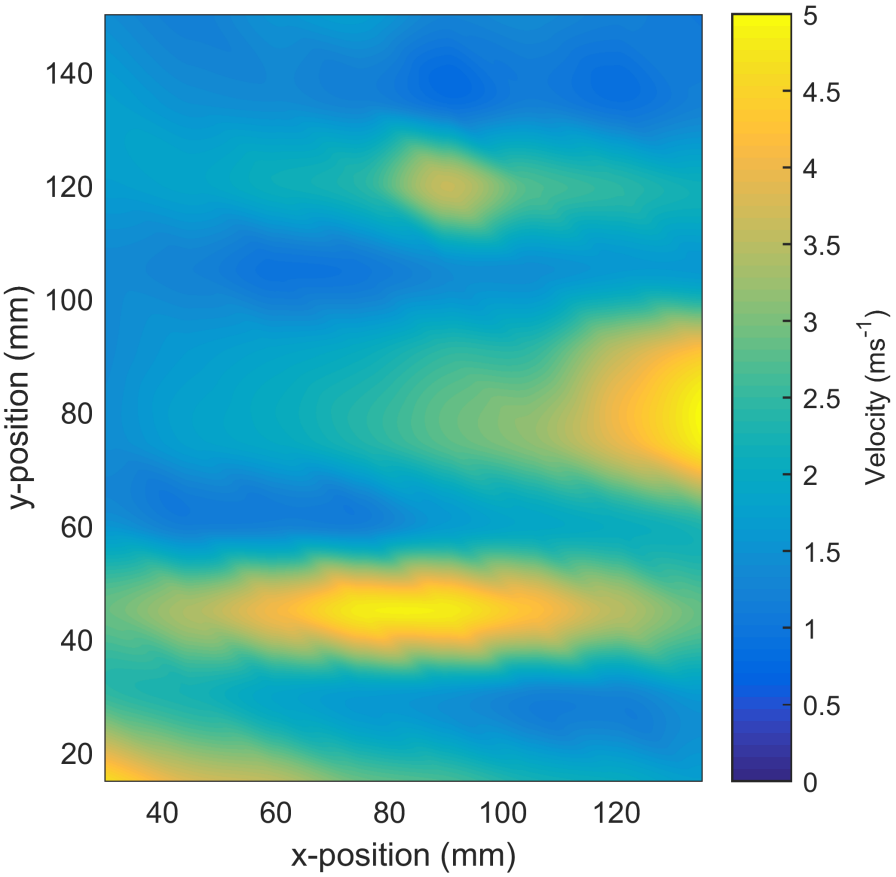


(A) No enclosure

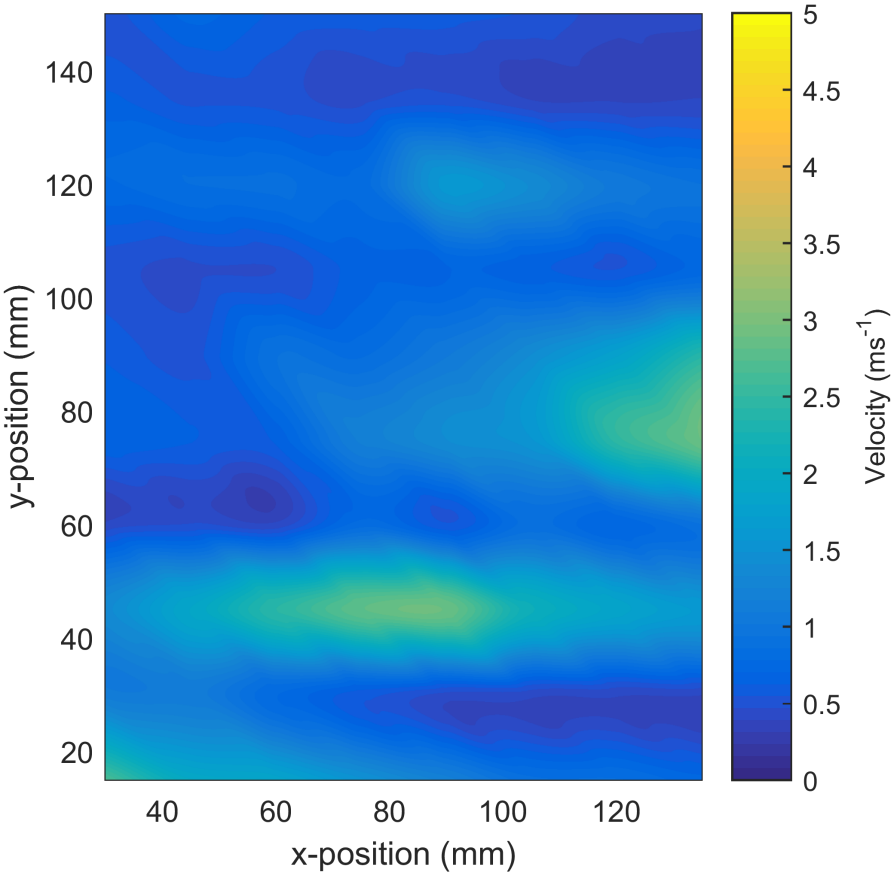


(B) Enclosure

FIGURE 7.12: Effect of the enclosure on the mean velocity in a plane parallel to the ground at the height of the shaft. The centre of the fan is located at $x = 0$ mm, and $y = 0$ mm and the the fan runs in the x-plane.

## 7.5 Prototyping of fans for testing

The optimal fans presented in Chapter 6 were manufactured. The processes used to manufacture the fans included reconstructing a solid model from the parametric representation of a fan, 3D printing of the fans and smoothing the 3D printed parts.

The fans were initially represented parametrically in vector form which was reconstructed into a solid model for 3D printing. The cross-section shape, blade angle and chord length are known at all infinitesimal radial steps; however, this form is very difficult to represent as a solid model. The method chosen for constructing the solid model was to define the cross-section (including the chord and angle) of the blade at 10 equidistant planes and to loft between them to form a solid part. The blade was then circularly patterned to create five blades. The hub was then constructed with identical mountings suitable for the test rig. All of the 3D printed fans were manufactured with a 2 mm tip clearance which is equivalent to a gap of 2% of the fan radius.

Once the fans were modelled, they were 3D printed using fused deposition modelling with an ABS filament. This is a rapid and low cost method of prototyping that creates parts with good dimensional accuracy. The downside of using a filament based 3D printing technique is that the surface roughness is dictated by the thickness of the filament. The 3D printed part can be smoothed using acetone vapour; however, this can reduce the accuracy of thin parts, such as the trailing edge. An alternative method of smoothing a part is to fill the gaps with a filler, which can also strengthen the thin trailing edges. Epoxy was used to fill the gaps and strengthen the trailing edges of all fans. The epoxy coating was polished to ensure a smooth surface.

# Chapter 8

# Experimental Results and Verification

The optimal fan designs presented in Chapter 6 were tested to validate the optimisation method developed in Chapters 3 to 5. All of the tests presented in this chapter were conducted using the method described in Chapter 7.

The results presented in this chapter are separated into three sections: Model validation, noise source identification and complete performance data for each fan. The results are followed with a comprehensive discussion.

## 8.1 Model Validation

The model developed in Chapters 4 and 5 predicted the flow rate and SWL of a fan at 1800 rpm under no load. Therefore, comparative experimental results had a fully open outlet so that the system pressure was as close to 0 Pa as possible while maintaining a rotational speed of 1800 rpm. It is important to note that the model does not include incident turbulence noise or fan-support interaction noise; hence, the experimental tests for model validation attempted to minimise turbulence and did not use supports in an endeavour to capture only self-noise.

Table 8.1 shows that the BEMT model predicted the flow rate well with fans 1 and 2 being slightly underpredicted; whereas, fans 3-5 were slightly overpredicted. Fans 1 and 2 had the highest solidity of the five fans and were expected to be the most affected by interactions between the blades. As the aerodynamic data was not corrected for interaction effects, the flow rates of fans 1 and 2 were expected to be overpredicted; however, the opposite effect was found. This was possibly caused by fans 3-5 having lower chord sizes and, hence, lower Reynolds numbers. This suggests that a different

| Fan | Predicted flow rate ($m^3 h^{-1}$) | Measured flow rate ($m^3 h^{-1}$) | Difference (%) |
|---|---|---|---|
| 1 (NACA0012 high flow) | 762 | 858 | -12.6 |
| 2 (NACA0012 mid flow) | 602 | 693 | -15.1 |
| 3 (NACA0012 low flow) | 317 | 268 | 15.5 |
| 4 (Optimised aerofoil section) | 765 | 677 | 11.5 |
| 5 (Optimised cambered plate) | 768 | 600 | 21.9 |
| Wellington 200/28 | - | 620 | - |

TABLE 8.1: Comparison of predicted and experimental flow rates of each fan blade for model validation. The commercially available Wellington 200/28 fan is presented for comparison.

| Fan | Predicted SWL (dBA) | Measured SWL (dBA) | Difference (%) |
|---|---|---|---|
| 1 | 41.0 | 62.7 | -52.9 |
| 2 | 39.4 | 63.7 | -61.7 |
| 3 | 37.8 | 62.6 | -65.6 |
| 4 | 4.8 | 65.4 | -1260 |
| 5 | 23.2 | 68.7 | -196 |
| Wellington 200/28 | - | 64.5 | - |

TABLE 8.2: Comparison of predicted and experimental SWLs of each fan blade for model validation. The commercially available Wellington 200/28 fan is presented for comparison.

flow regime was present which XFOIL is unable to accurately predict at these lower Reynolds numbers.

Table 8.2 shows that the BPM model did not predict the overall sound power level (OSWL) well. Measurements of fans 1-3 showed that they all had similar SWLs, which is surprising as fan 1 had a higher chord and twist angle than fan 2 which was subsequently higher than fan 3. The similar measured values of SWL indicated that self-noise was not the dominant source as both the chord length and angle impact the self-noise. Hot wire measurements across the face of the fan, in Section 8.2.3, showed moderate turbulence incident on the fan. This confirmed that the turbulent noise is likely the dominant source of noise which caused the discrepancy between the predicted and measured SWL values.

The SWL of fans 4 and 5 was significantly underpredicted which, as discussed in Chapter 6, is probably a result of the dissimilarity between the NACA0012 aerofoils and the sections used in fans 4 and 5.

Figures 8.1 to 8.5 show that the predicted one third octave band results captured the shape of the high frequency region correctly but significantly underpredicted the low frequency region.

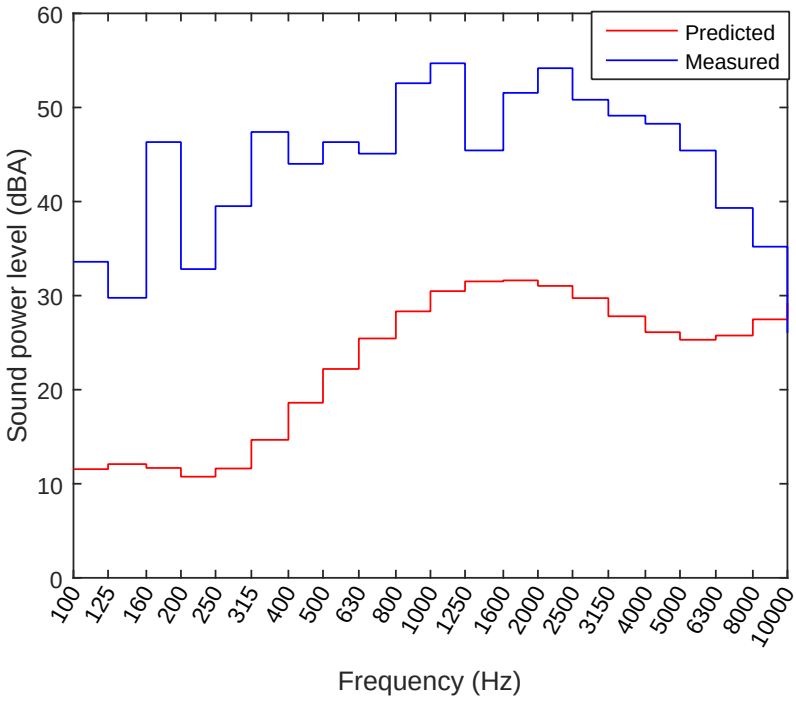


FIGURE 8.1: Comparison of the predicted and experimental one third octave bands of fan 1 for model validation.

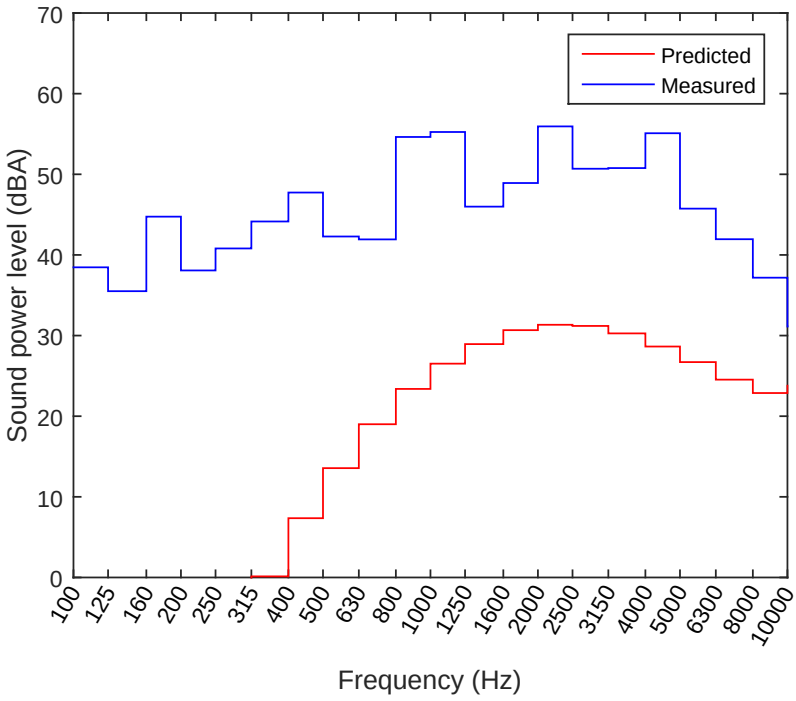


FIGURE 8.2: Comparison of the predicted and experimental one third octave bands of fan 2 for model validation.

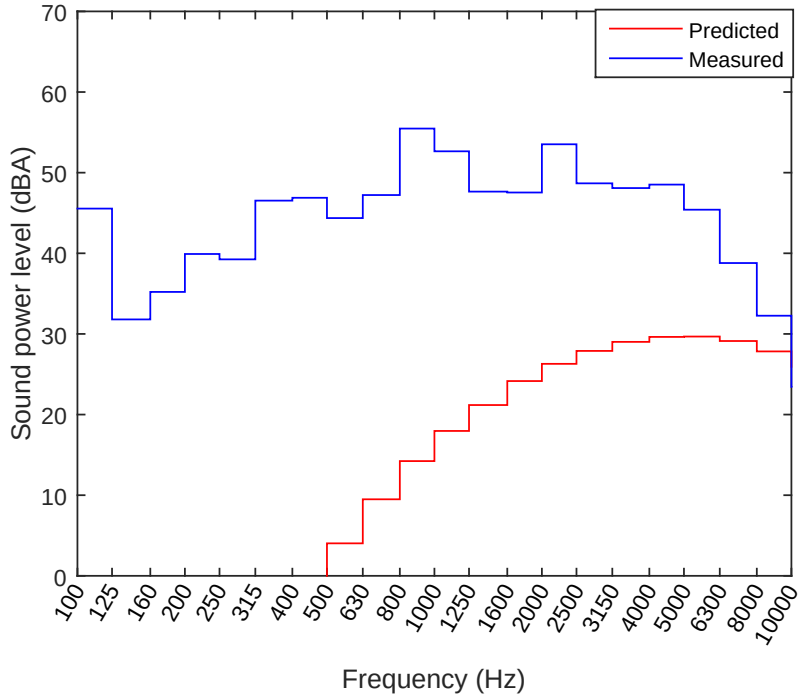


FIGURE 8.3: Comparison of the predicted and experimental one third octave bands of fan 3 for model validation.

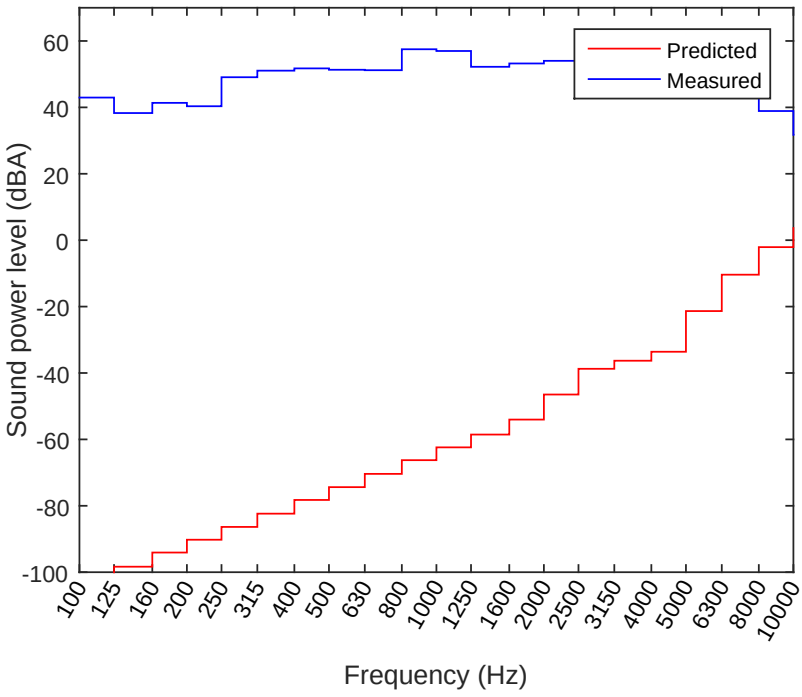


FIGURE 8.4: Comparison of the predicted and experimental one third octave bands of fan 4 for model validation. Note: The axes do not conform to all other comparison graphs.

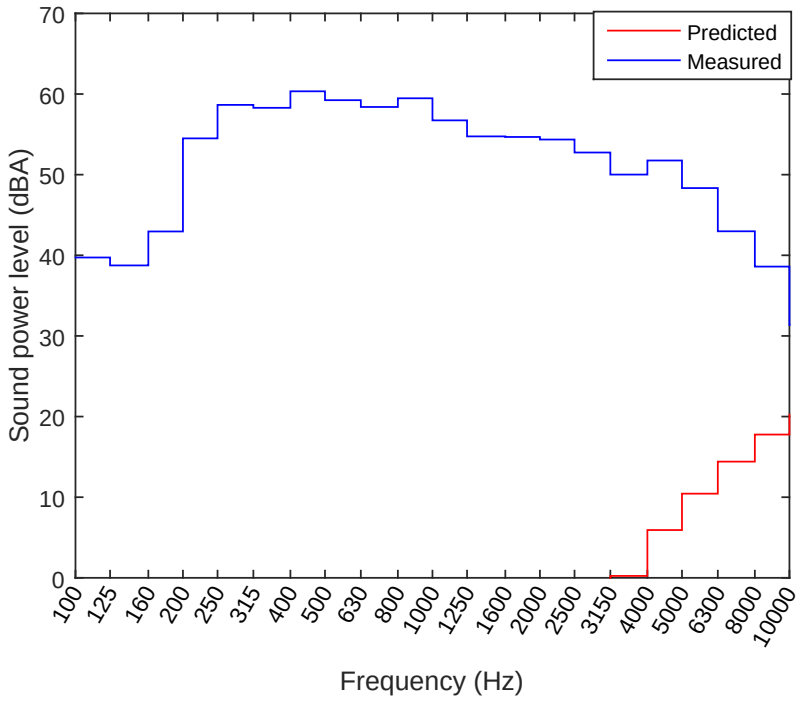


FIGURE 8.5: Comparison of the predicted and experimental one third octave bands of fan 5 for model validation.

## 8.2 Noise source identification

Noise source identification is important when modelling or testing fans. It is important to know what the dominant noise sources are so that models or experiments can account for them. This section describes how a 3D printed prototype of fan 1 was used to quantify the effects of surface roughness, incident turbulence and fan-support interaction noise at 1800 rpm.

### 8.2.1 Surface roughness

Most commercial 3D printers generate parts with high surface roughness. Fan 1 was tested both before and after being polished to quantify the effects of surface roughness. The process used to smooth the fan started with filling any cavities with epoxy and then polishing the blades to a smooth finish, as discussed in Section 7.5.

The tests for surface roughness were conducted with no supports or additional induced turbulence at 1800 rpm with fan 1 at all outlet sizes. The results from these tests are presented in Figures 8.6 and 8.7 for comparison.

Figure 8.6 shows little difference in the acoustic performance of the fan at low flow rates. At higher flow rates, the rough fan has a minor increase in noise; however,

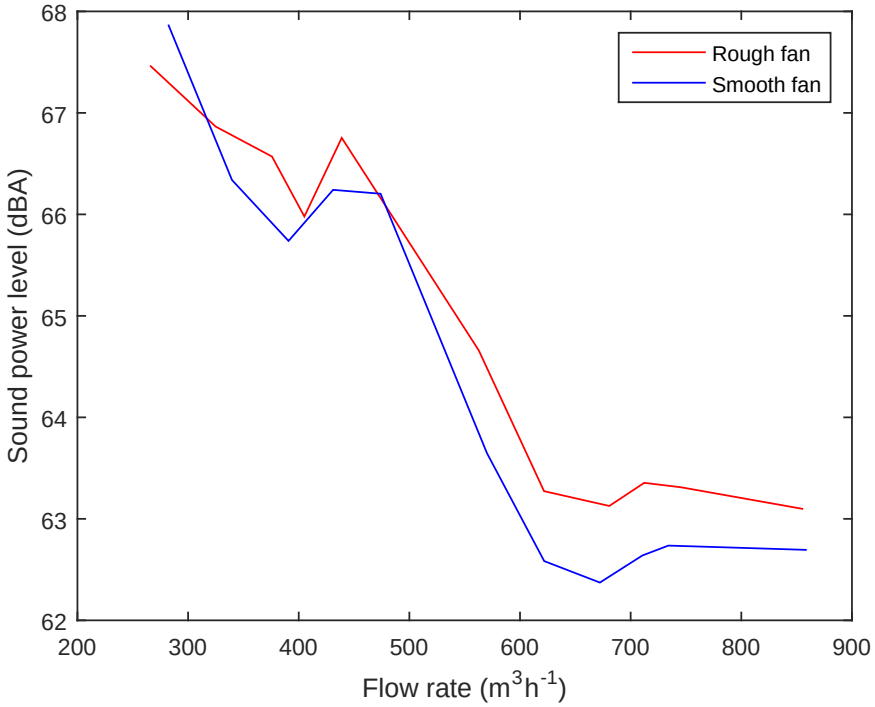


FIGURE 8.6: Comparison between the OSWL of fan 1 with original rough finish and polished finish.

the difference is not significant compared to the experimental error of ±1.5 dBA. Although not significant compared to the error, the small increase in SWL suggests that 3D printed fans should be smoothed before testing.

Figure 8.7 shows that there is little difference between the narrowband spectra for the rough fan and that no additional tones are introduced or exacerbated by the rough fan.

### 8.2.2 Fan-support interaction noise

Fan-motor assemblies commonly used in refrigerators have supports that attach the motor to the shroud to support both the motor and the fan as shown in Figure 8.8.

To determine the noise generated by the fan-support interaction, the supports were removed from a shroud, and the motor operated without any end support. Measurements were performed using fan 1 at 1800 rpm at all outlet sizes. The results from these tests are presented in Figures 8.9 and 8.10.

Figure 8.9 shows a large difference in the OSWL between the measurements with and without supports. However, Figure 8.10 shows that despite both measurements having peaks at the BPF and subsequent harmonics, the measurements with supports have an additional peak at 105 Hz and a harmonic at 210 Hz. The 105 and 210 Hz tones are likely from the vibration of the test rig chamber. The vibration of the chamber occurs because

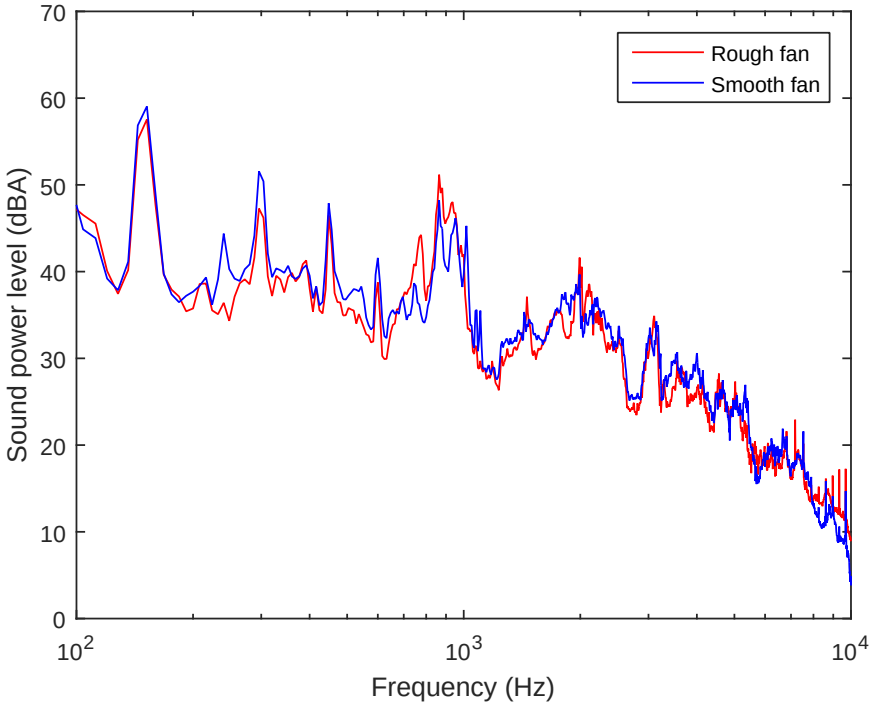


FIGURE 8.7: Comparison between the narrowband spectra of fan 1 at 1800 rpm with a fully open outlet with original rough finish and polished finish.

of the rigid connection to the fan, which excites the chamber. Review of McKinlay's measurements [68], which conformed to ISO10302 and had a rigid connection between the fan and the chamber, showed similar peaks in all narrowband measurements. This indicates that it is the chamber vibrating, a limitation of ISO10302. The frequencies of the tones vary slightly depending on the outlet size and fan speed. This likely occurs because smaller outlet sizes and higher speeds increase the pressure in the chamber which consequently increases the tension in the chamber walls, thus, raising the natural frequency of the chamber walls.

To determine the aeroacoustic effect of the supports, the tests were repeated with the fan unsupported by the test rig but with a shroud with the supports still attached behind the fan. Figure 8.11 shows that without the rigid connection between the fan and the chamber, there is no significant difference in the overall SWL results. Figure 8.12 supports this with no increase in tonal noise at the BPF, which is typical of fan-support interaction noise. Furthermore, these results highlight that the additional noise shown in Figure 8.9 is likely from vibration of the chamber.

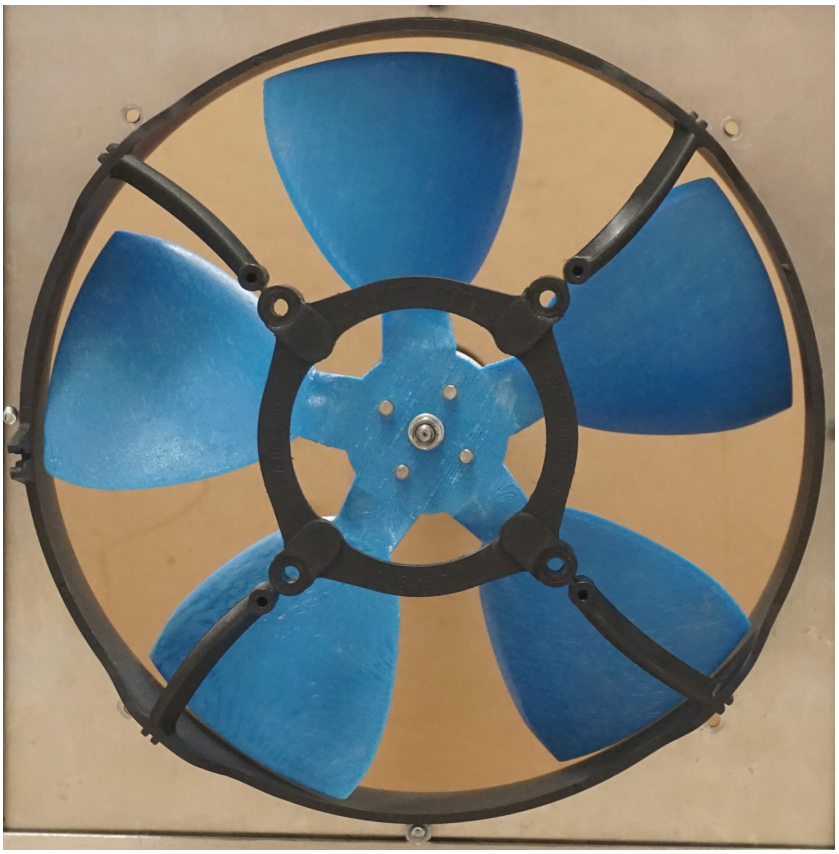

FIGURE 8.8: Mounting supports to connect the fan and motor to the shroud. This image shows the non-connected configuration. Note that the camera angle makes the fan appear off-centre.

### 8.2.3 Incident turbulence noise

Turbulence incident on a fan is known to generate noise, as previously discussed in Chapters 2 and 4. To quantify the effect of IT noise, a grid was introduced upstream of the fan to generate turbulence subsequently incident on the fan. The measurements were performed using fan 1 at 1800 rpm over all outlet sizes.

The turbulence grid used in this experiment had 10 mm square bars with 40mm spacing, as shown in Figure 8.13. The axial inlet flow was measured using a 1D hotwire so that the turbulence intensity and integral length could be calculated to compare the difference in turbulence generated by the grid. The results are presented in Figures 8.14 and 8.15.

Initially, the grid was installed 90 mm from the fan; however, this did not increase the turbulence incident on the fan as shown in Figure 8.14. Moving the grid to 40 mm away from the fan increased the turbulence intensity sufficiently that a small increase in SWL could be expected. The grid did not alter the integral length of the turbulence except near the hub of the fan. The acoustic tests were performed with the grid at 40 mm.

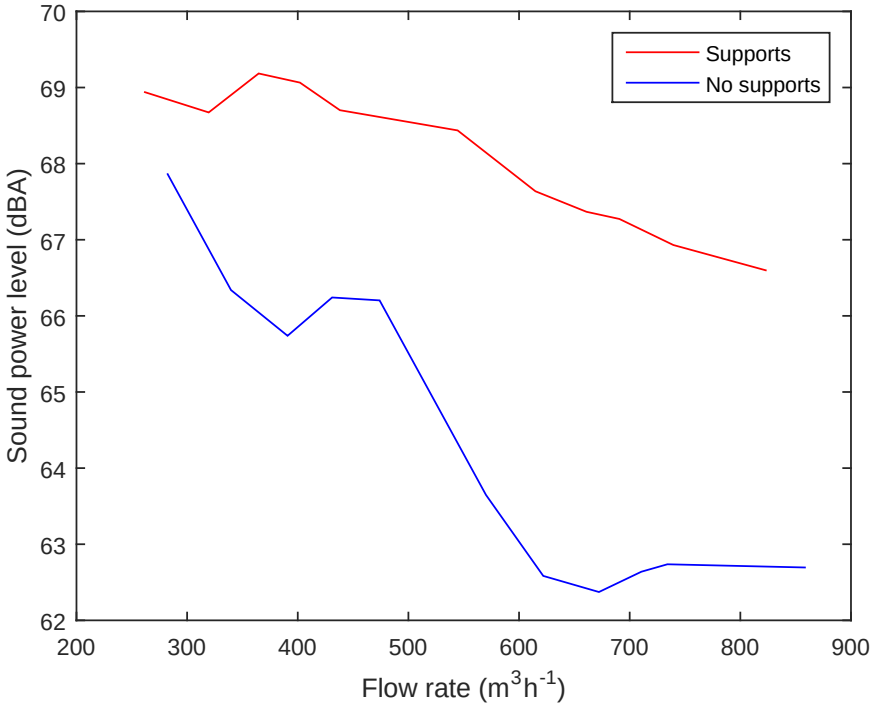


FIGURE 8.9: Comparison between the OSWL of fan 1 with fan-supports and without fan-supports. The rest rig was rigidly connected to the chamber in this test.

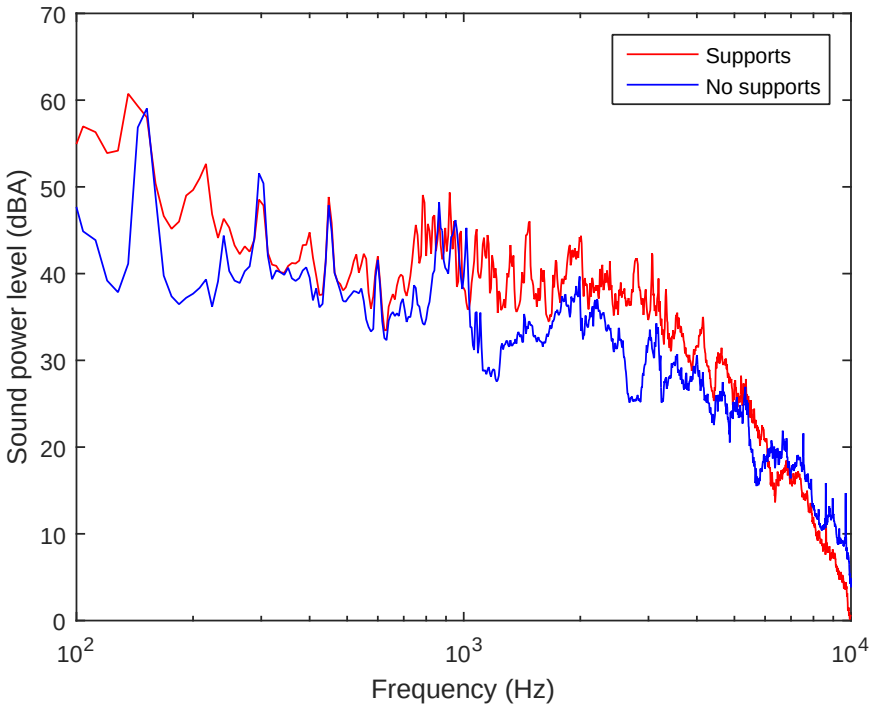


FIGURE 8.10: Comparison between the narrowband spectra fan 1 with fan-supports and without fan-supports. The test rig was rigidly connected to the chamber in this test. The outlet for this test was fully open.

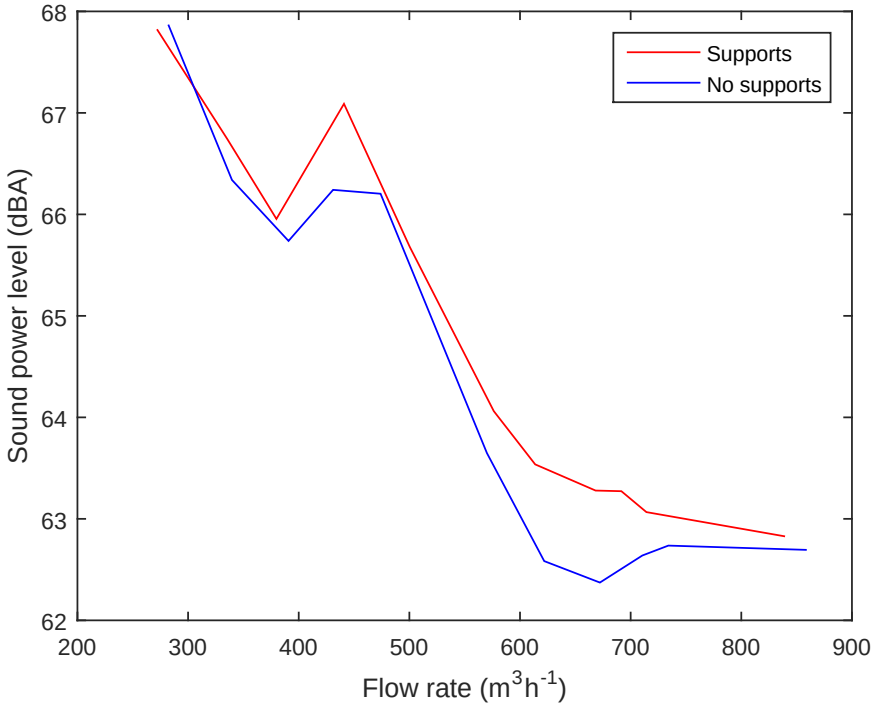


FIGURE 8.11: Comparison between the OSWL of fan 1 with fan-supports and without fan-supports with no connection to the chamber.

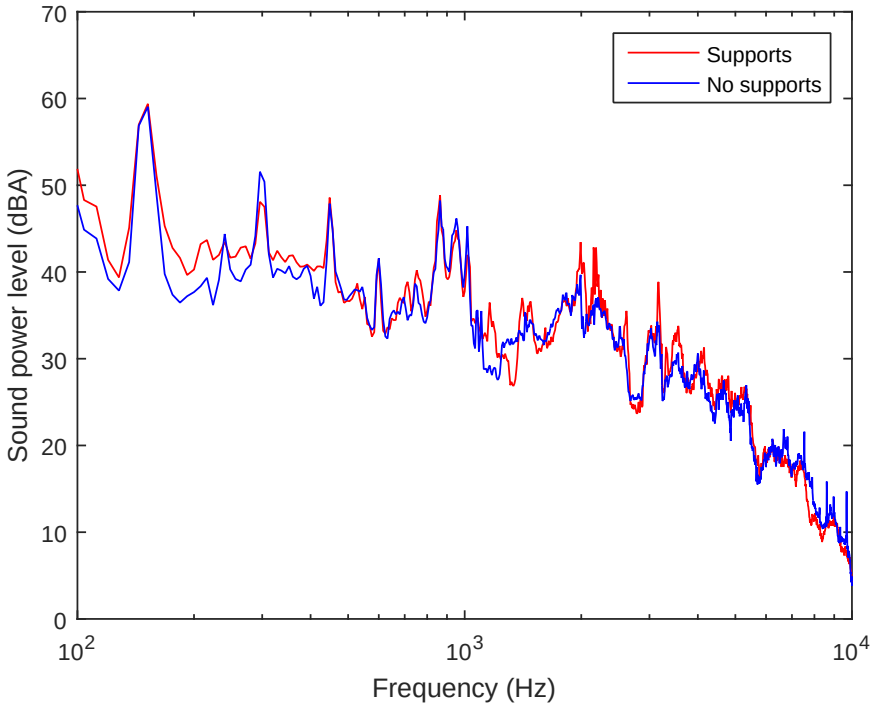


FIGURE 8.12: Comparison between the narrowband spectra fan 1 with fan-supports and without fan-supports with no connection to the chamber. The outlet for this test was fully open.

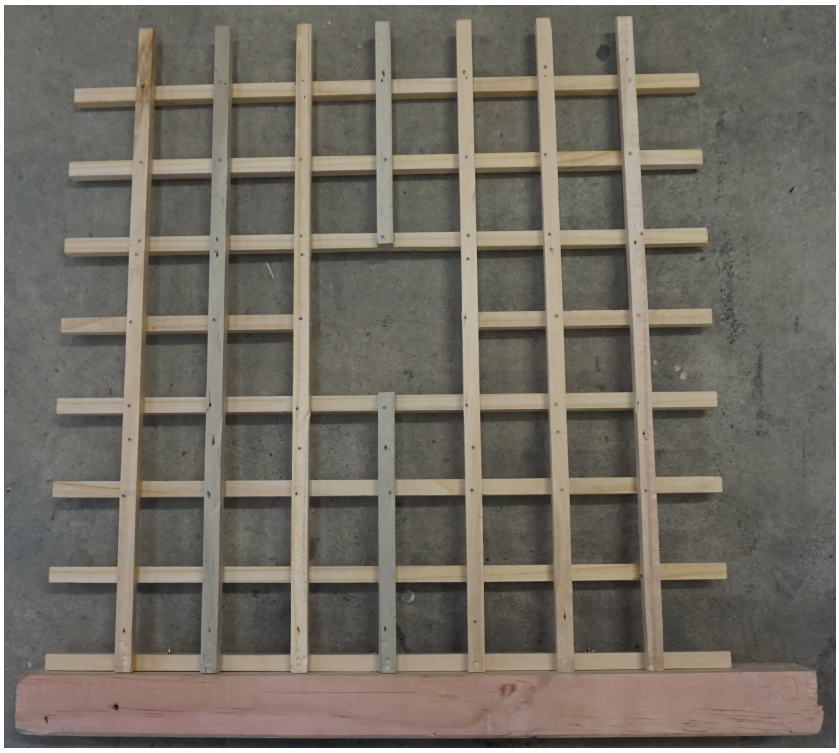

FIGURE 8.13: Turbulence grid used to generate IT noise. The grid has 10 mm square sections with 40 mm spacing between each bar.

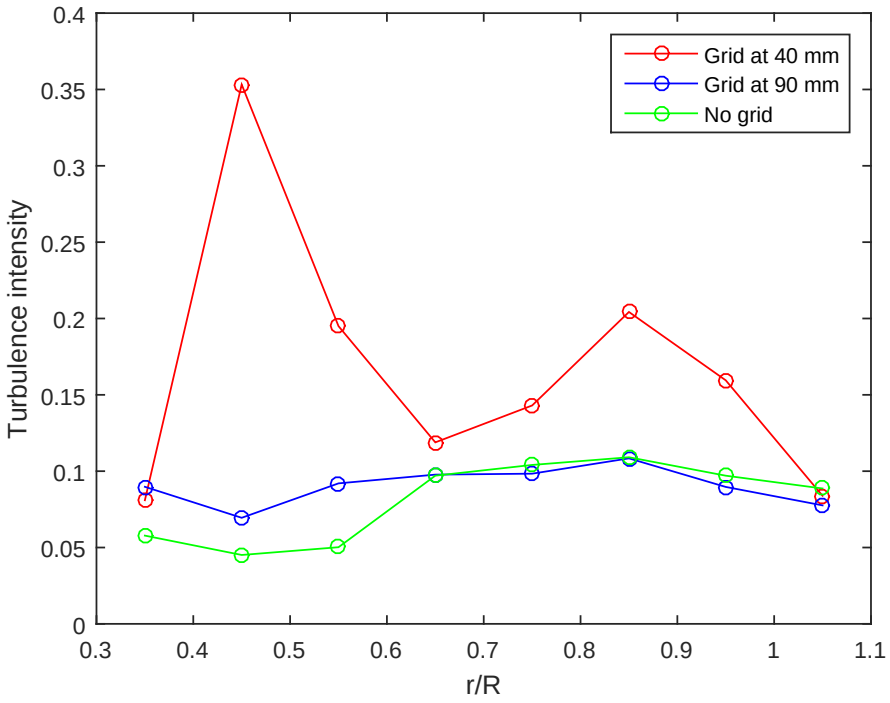


FIGURE 8.14: Comparison between the turbulence intensity incident on fan 1 at 1800 rpm with and without a grid.

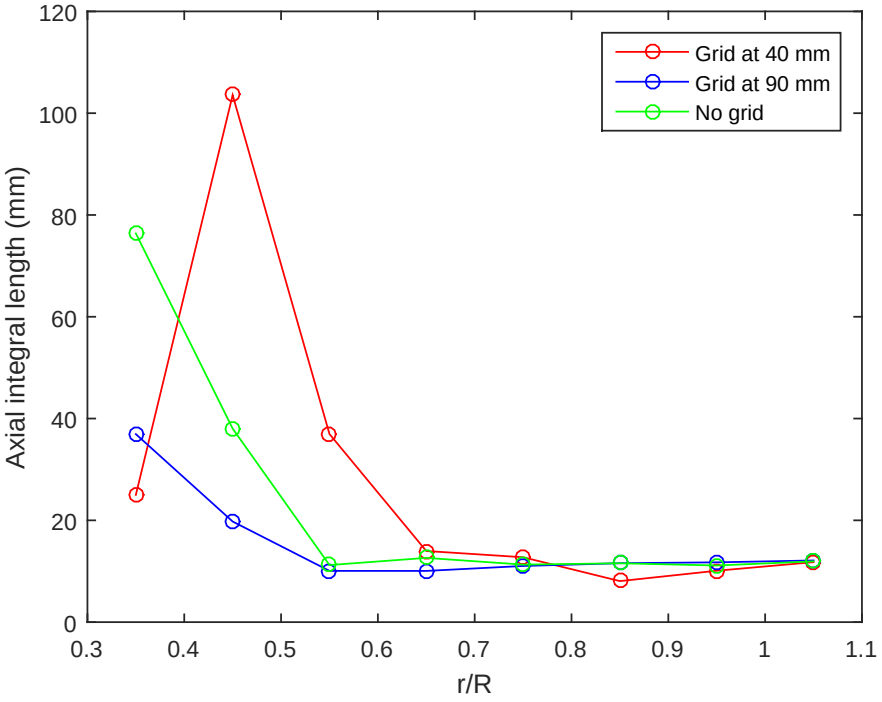


FIGURE 8.15: Comparison between the turbulence integral length of the turbulence incident on fan 1 at 1800 rpm with and without a grid.

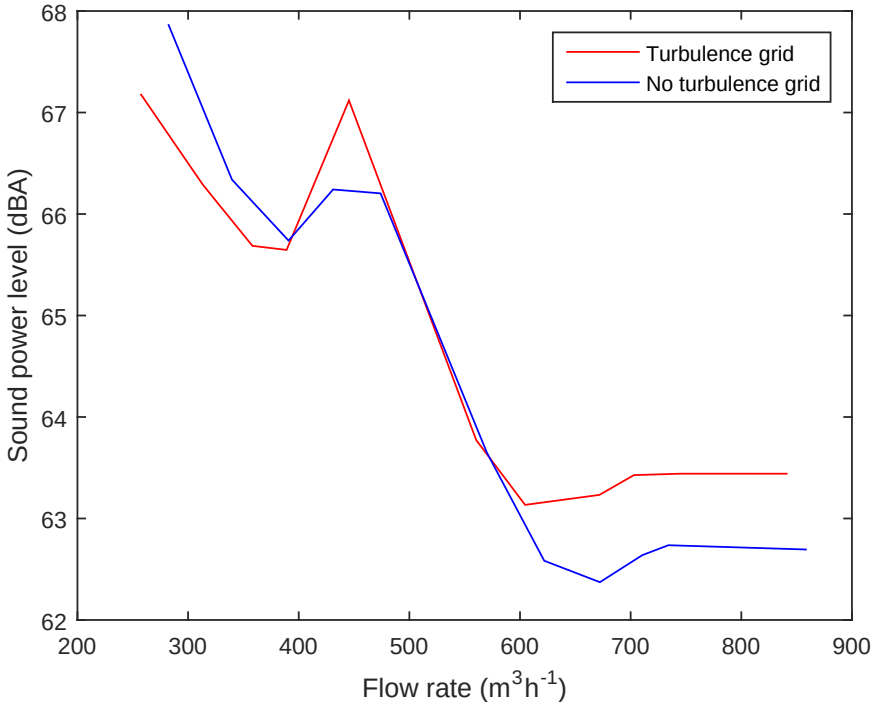


FIGURE 8.16: Comparison between the OSWL of fan 1 with a turbulence grid and without a turbulence grid at 1800 rpm.

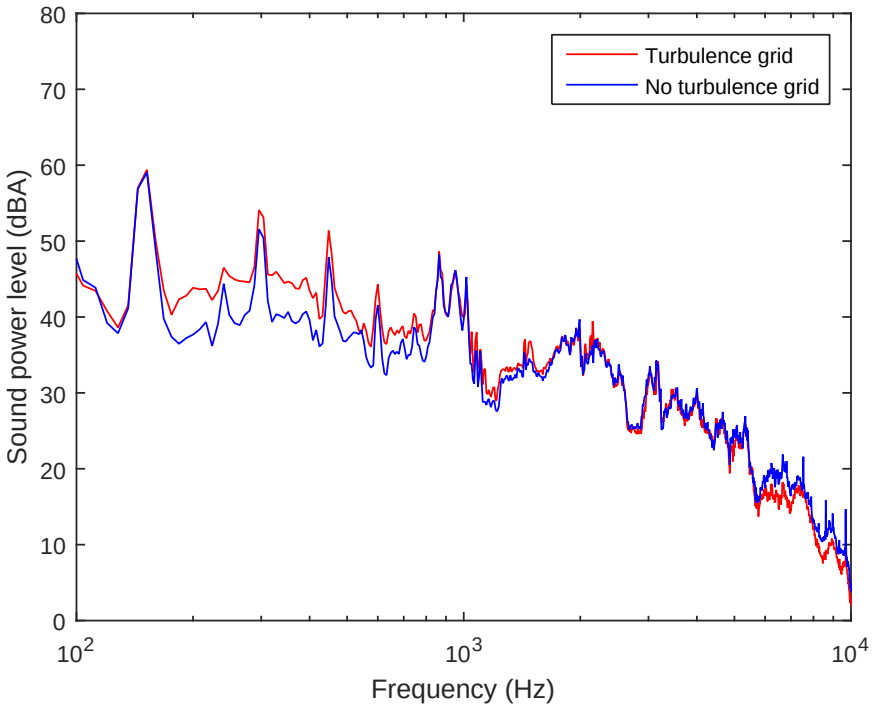


FIGURE 8.17: Comparison between the narrowband spectra of fan 1 with a turbulence grid and without a turbulence grid at 1800 rpm.

Figure 8.16 shows at higher flow rates that the turbulence grid had a minor effect on the SWL. However, similar to the roughness measurements, this is within the experimental error of $\pm 1.5$ dBA. As the IT without the grid present is moderately high, it is expected that IT noise is the major contributor to the OSWL of the tested fans.

The IT noise can be approximated from the turbulence integral length and intensity as discussed in Section 4.4.1. Using the measured turbulence values at the inlet of fan 1, the turbulence was included in the acoustic model. This gave an OSWL of 71.9 dBA, which had an error of 12.8% compared to the measured value. The one third octave bands are shown in Figure 8.18. This is a significantly better approximation than originally used; hence, IT noise should be included in future modelling. The simple IT noise model appears to have the correct shape when compared to the measured values. Furthermore, Figure 8.17 shows a moderate broadband difference in the 200-800 Hz region, which is where the IT model predicts the highest noise to be. The downside of requiring an IT model is that simple IT noise models do not consider the shape of the blade; hence, they are not suitable for optimisation.

### 8.2.4 Dominant noise source

The previous results identifying the noise sources of the fan showed very little difference. This is likely because the turbulence from the enclosure generated significant IT

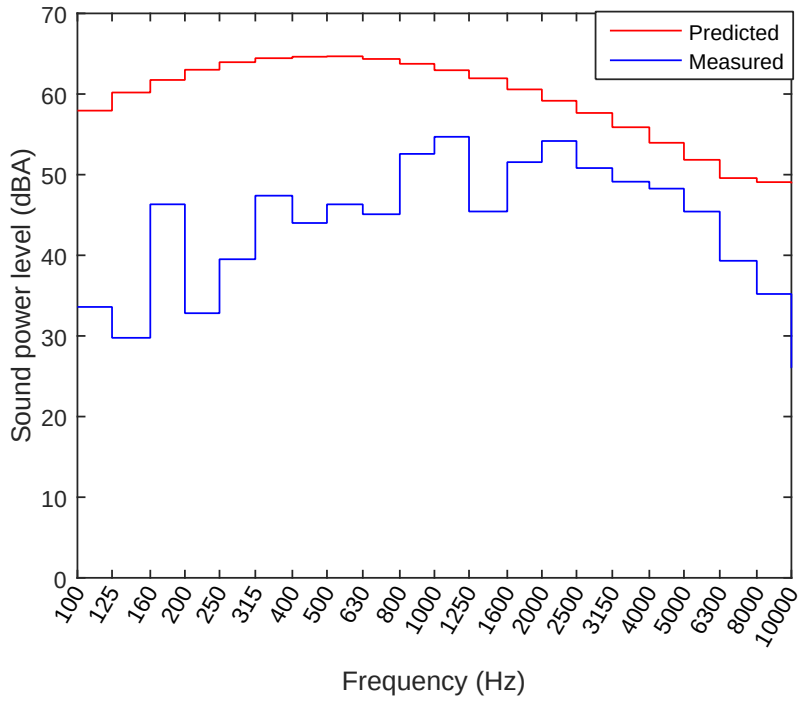


FIGURE 8.18: Prediction of fan 1 at 1800 rpm with turbulence compared to the measured results.

noise. Figure 8.19 contains the A-weighted one-third octave bands overlain on the narrowband spectra to assist identification of the major contributor to the OSWL. This is not apparent from the unweighted narrowband data alone.

Figure 8.19 can be broken into three regions; the first in the 100-800 Hz range where tonal noise at the BPF dominates, the second in the 800-1250 Hz range where tonal noise not at the BPF dominates and the third beyond 1250 Hz where broadband noise dominates.

The 100-800 Hz region of Figure 8.19 shows that the tonal peaks in the data predominantly occur at the BPF. The cause of the tones at the BPF could be due to the fan not being centered correctly resulting in a periodic variation in the tip clearance at the BPF. Alternatively, these tones could be a result of a periodic variation of the inlet flow of the fan. Figure 7.12A shows a periodic variation of the inflow, which provides some evidence for this hypothesis. Regardless of the cause of these tones, the A-weighting renders them minor contributors to the OSWL.

The 800-1250 Hz region is, perhaps, the most interesting region of Figure 8.19 as there are three distinct tones that contribute strongly to the 1000 Hz one-third octave band, the largest contributor to the OSWL. The cause of these tones was somewhat perplexing as they are not at a harmonic of the BPF or where an aeroacoustic tone would typically be. In this frequency range, the test rig noise is at least 10 dB below the measured fan

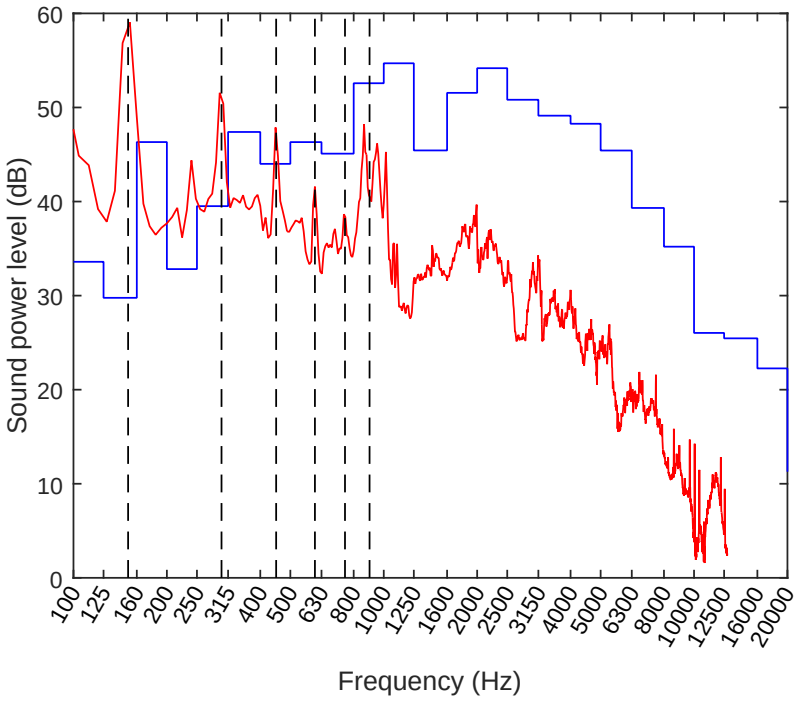


FIGURE 8.19: Comparison between the unweighted narrowband results and the A-weighted 1/3 octave band results. The blade passing frequency and subsequent harmonics are overlain in dashed lines. The results are for fan 1 at 1800 rpm with a fully open outlet size.

noise; hence, it is unlikely the test rig is causing any interference. It was, however, noted that each of the peaks in Figure 8.19 aligned with a peak in measurements of the test rig noise. These tones are, perhaps, a result of the shaft resonating as this frequency is approximately twice the resonant frequency of the overhanging shaft. In the case of the fan, the vibrations may be being transmitted through the fan and manifest as noise. Prediction of the first natural frequency of the fan is difficult as mechanical properties of 3D printed parts are highly variable; however, a very conservative estimate of the first mode of the fan places it above 1200 Hz making this an unlikely cause of the noise. Interestingly, the 864 Hz tone, which was the strongest tone in the 850-1000 Hz region, appear across all of the fans. This provides additional evidence that it is a property of the test rig, rather than of aerodynamic origins.

The region beyond 1250 Hz contributes as much to the OSWL as the 800-1250 Hz region does. The broadband nature of this region indicates that it is caused by IT noise, which has already been shown to be one of the dominant noise sources.

FIGURE 8.20: Commercial Wellington Drive 200/28 refrigerator fan used for comparison.

## 8.3 Fan performance data

Each of the five 3D printed fans were tested to generate full performance data which is presented in Figures 8.21 to 8.25. A commercially available 200 mm refrigerator fan was also tested for comparison (See Figure 8.26). The commercial fan used for comparison was a Wellington Drive 200/28 injection-moulded, cambered-plate fan with solidity of approximately 1, shown in Figure 8.20.

The plots used to convey the performance data of the fans have contour plots of the SWL, efficiency and power usage of the fan at specific pressures and flow rates. Each of these is presented in a different colour with each isoline labelled with its respective value. The iso-speed lines show the actual pressure at a specific flow rate. The data in these plots is not very smooth as no averaging of measurements was performed. Some outliers in the power and efficiency were removed as a result of spurious torque measurements not being detected at the time of measurement. Typically, these spurious measurements gave efficiencies over 100% so could easily be detected.

The results in Figures 8.21 to 8.25 support the evaluation of the validation measurements. The SWL of the five fans does not change significantly with values typically ranging from 58 to 72 dBA with the exception of fan 3 which ranges from 54 to 65 dBA. This is likely because the IT noise is the dominant source, and the turbulence properties are similar for all of the fans except fan 3. As fan 3 has approximately one half of the flow rate of the other fans, it likely had less intense turbulence incident on the fan which resulted in less noise generated.

In all of the figures, there is an inflection in the SWL, power and speed curves that indicates the stall point. At this point, the fans performance typically becomes degraded with low flow rates, a plateau in the total fan pressure and a rapid increase in the SWL and power usage.

The overall trends were increasing SWL and power usage for higher rotational speeds and higher pressures, which is typical for axial fans. The efficiency contours are more interesting as they show a region of high efficiency before and after the stall point but low efficiency around the region where stall first occurs. Additionally, the efficiencies are higher than expected. There were some issues with spurious torque measurements which were corrected by zeroing the strain gauge voltage; however, there is a possibility that the torque measurements contain some errors. Furthermore, due to a fault with the motor, higher currents were been drawn which invalidated the torque constant. Therefore, the torque measurements cannot be compared to the torque calculated from the motor's torque constant. Further testing is required to determine the accuracy of the efficiencies reported in Figures 8.21 to 8.25.

At the modelled 1800 rpm, the fans typically require around 20 W of power to operate. This is a slight underprediction of the 13 W predicted by the BEMT model. Again, fan 3 does not follow this trend using about 15 W at 1800 rpm, which was also underpredicted by the model.

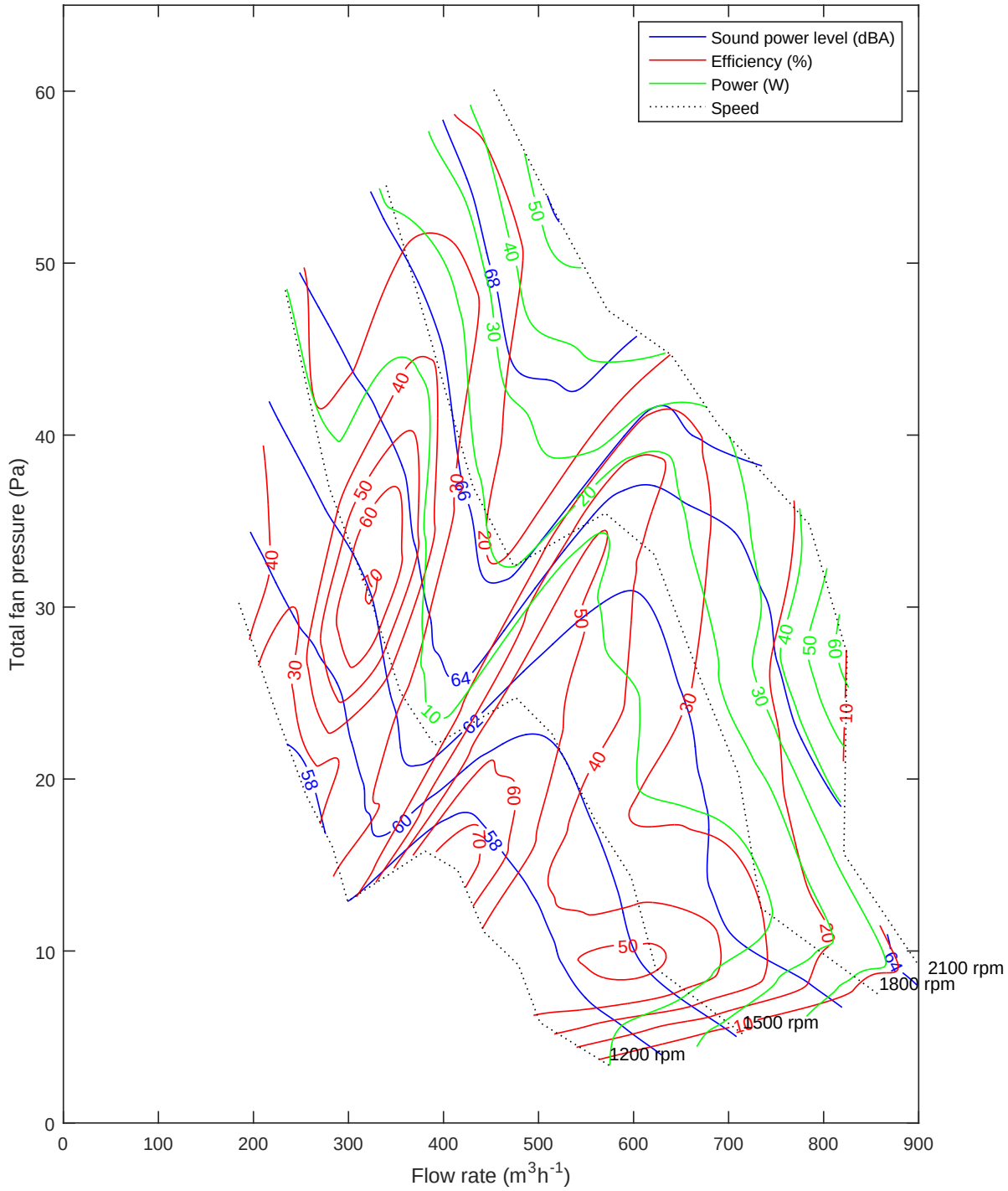


FIGURE 8.21: Complete performance data of fan 1.

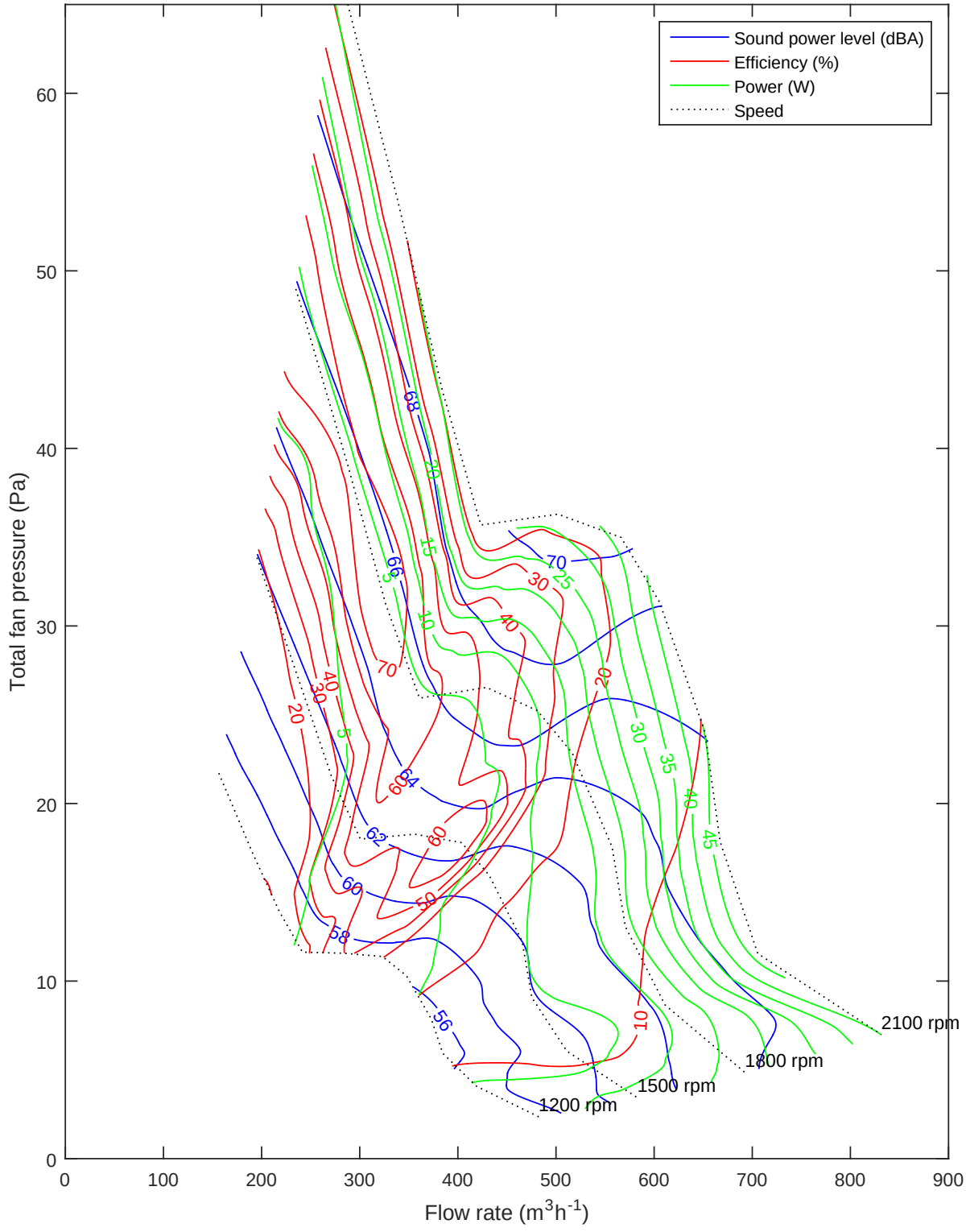


FIGURE 8.22: Complete performance data of fan 2.

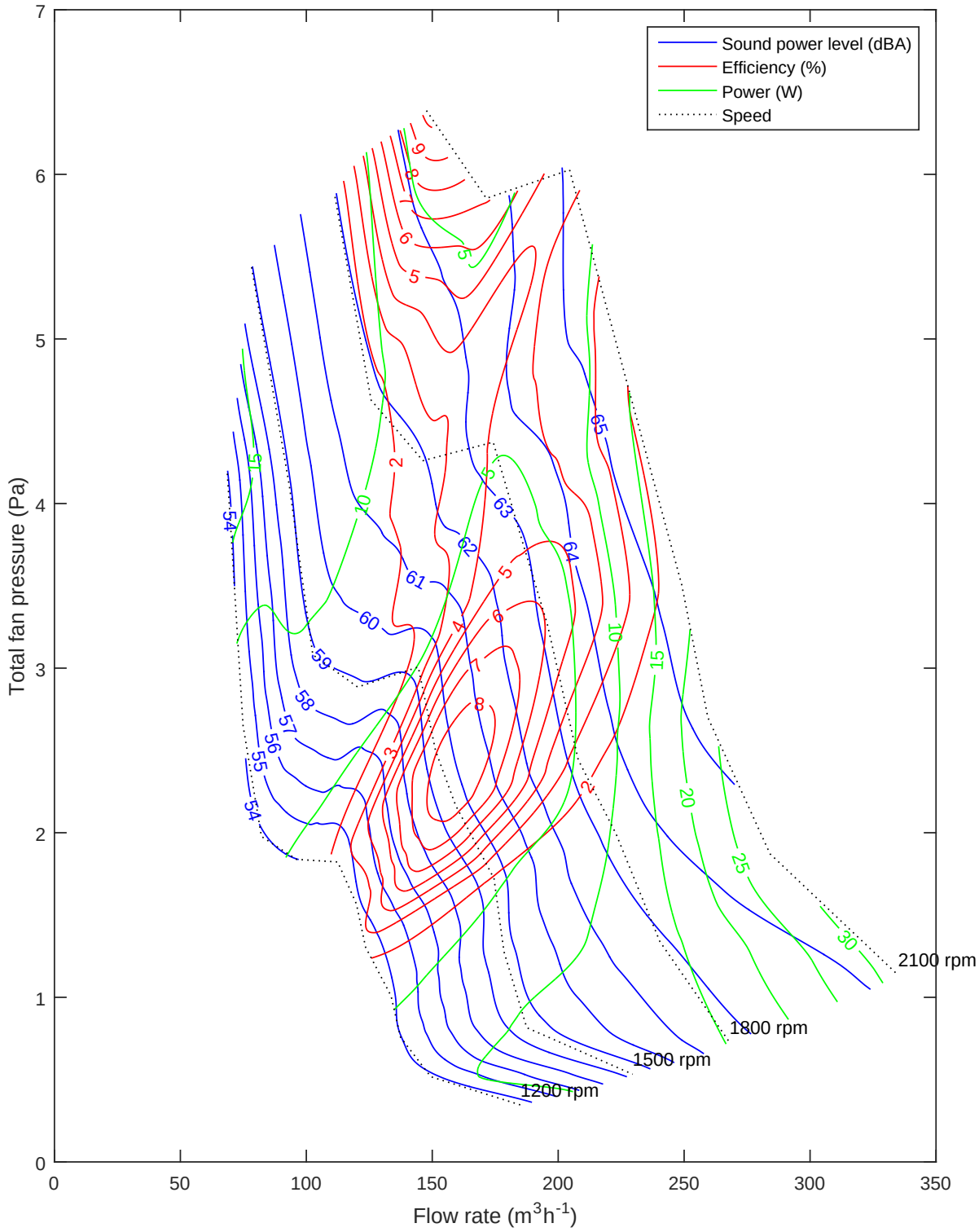


FIGURE 8.23: Complete performance data of fan 3. Note: The axes do not conform to all other performance data graphs.

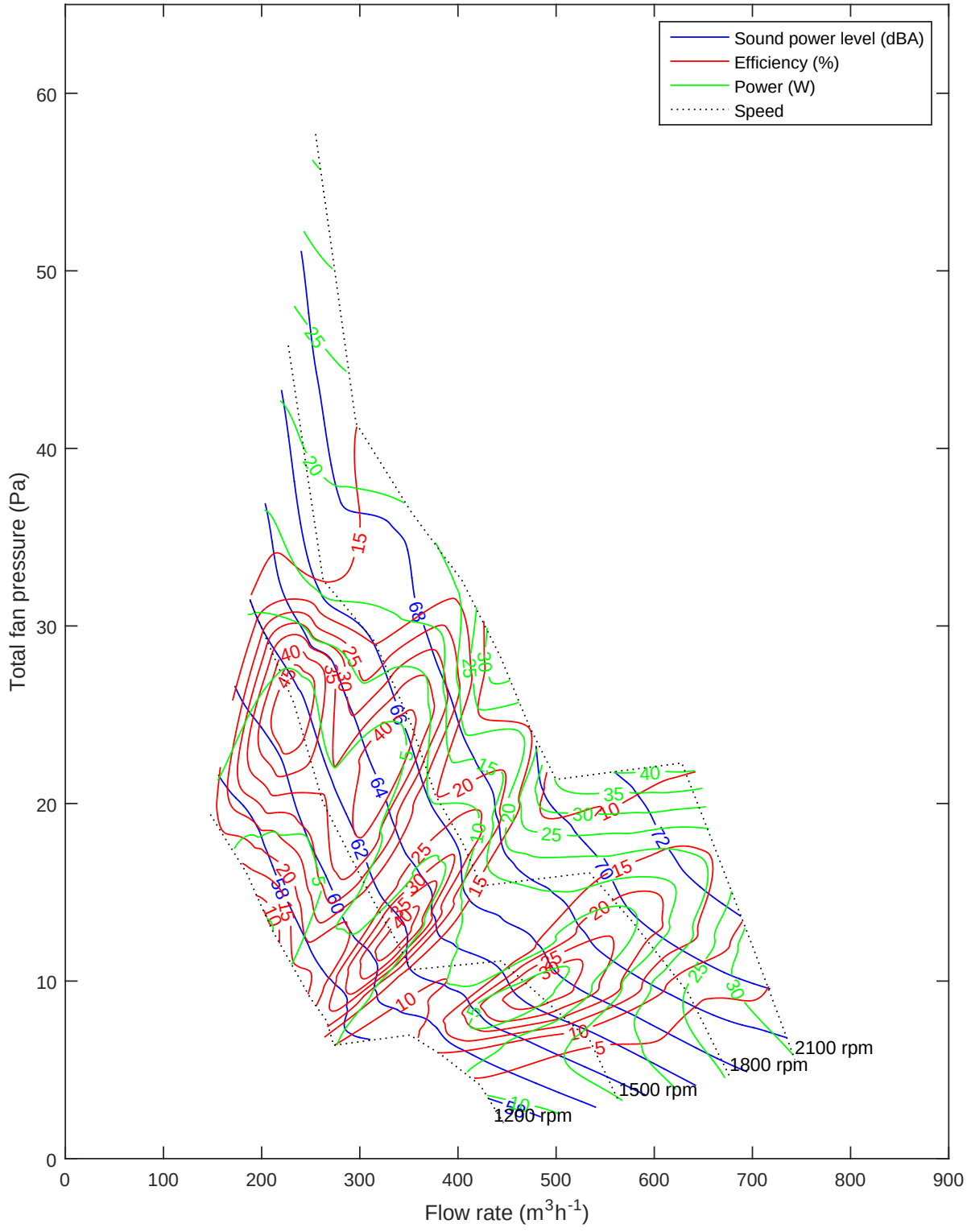


FIGURE 8.24: Complete performance data of fan 4.

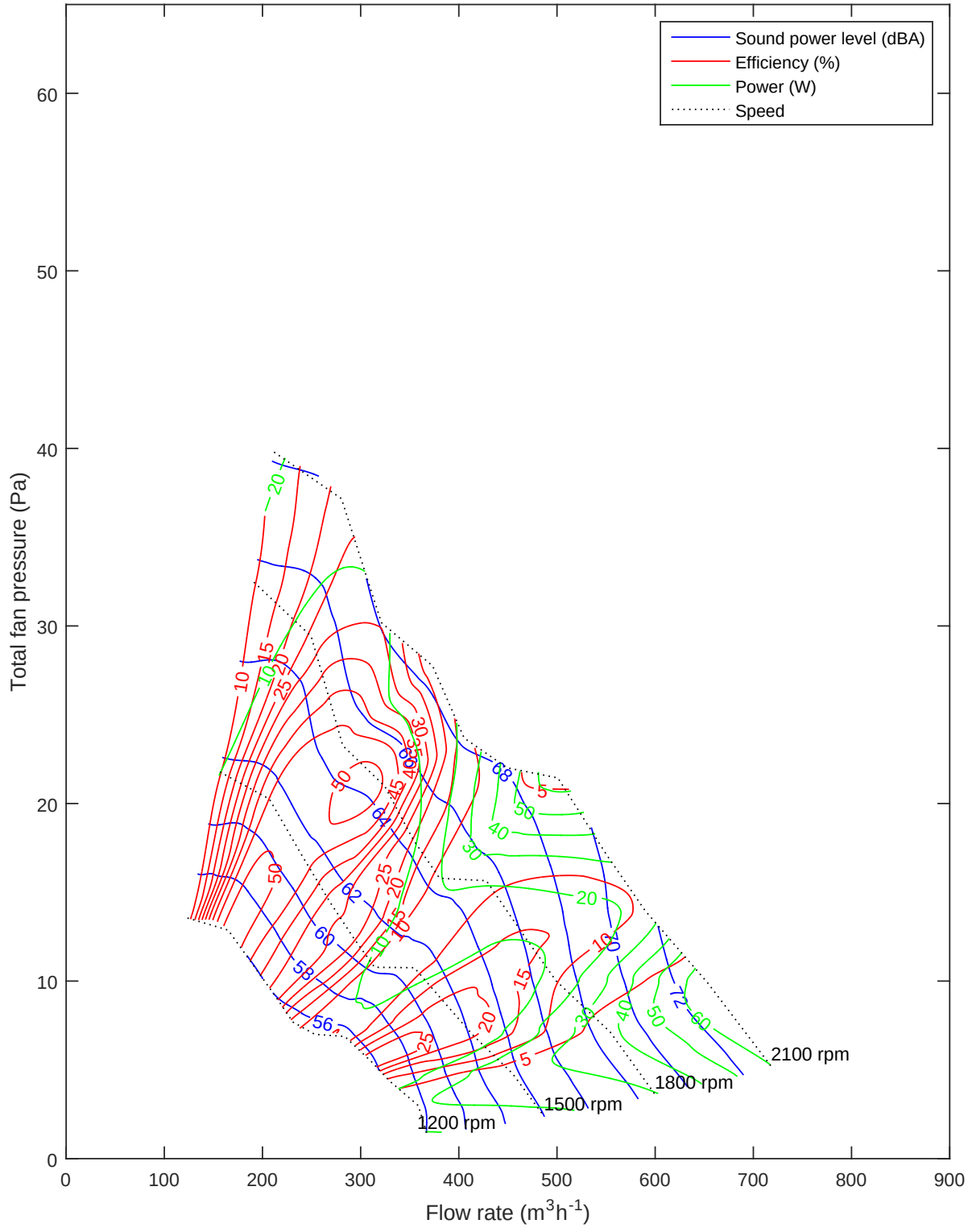


FIGURE 8.25: Complete performance data of fan 5.

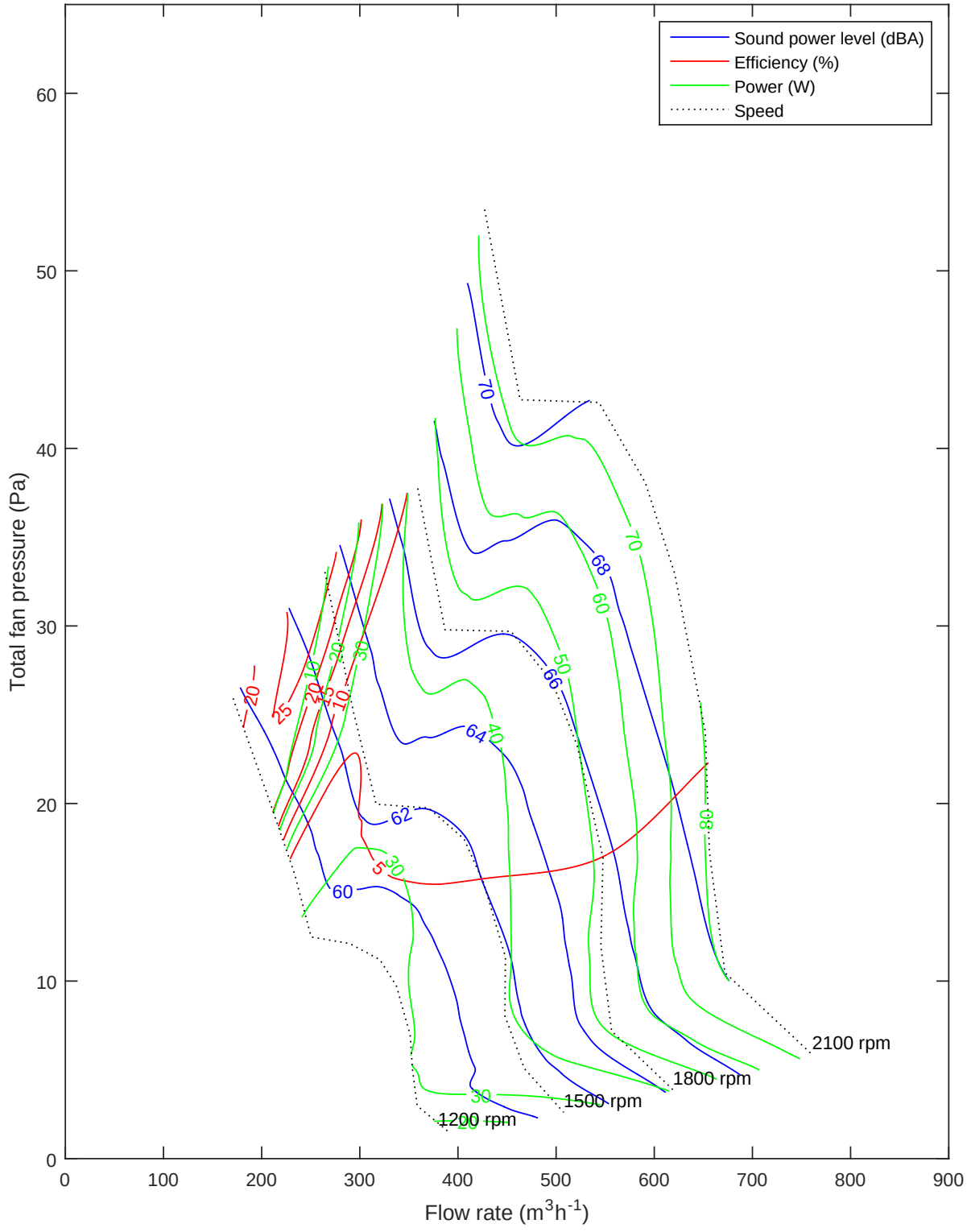


FIGURE 8.26: Complete performance data of a Wellington Drive 200/28 refrigerator fan for comparison.

## 8.4 Summary

The BEMT model predicted the flow rates of the fans well; however, the BPM model did not predict the SWL well. For fans 1-3, the BPM model may have had a reasonable prediction of the self-noise of the fan, but the IT noise generated by the fan was significantly higher than the self-noise. Modelling of the turbulence noise using the measured values of the inlet turbulence intensity and integral length provided better results for the predicted SWL. Fans 4 and 5 were very poorly predicted by the BPM model which supports the hypothesis that the dissimilarity between the NACA0012 aerofoil used in the scaling of the semi-empirical BPM model and the cross-sections of fans 4 and 5 would cause a poor prediction of the fan self-noise.

Attempts to identify the noise sources were more successful with both the high surface roughness fan and the fan with a grid generating approximately 1 dB higher SWLs. The attempts to quantify the fan-support interaction noise demonstrated that the ISO10302 test method is potentially flawed in that the chamber is easily excited, and any vibrations by the fan or motor can cause the entire structure to act as a noise source. Repeats of the fan-support interaction tests without a rigid connection were more fruitful, showing that the interaction noise was not a significant contributor to the OSWL.

Overall, fan 1 had superior performance as compared to the commercial refrigerator fan tested with higher flow rate, total fan pressure and efficiency. Both fans generated similar SWLs; however, fan 1 could generate equivalent performance to the commercial refrigerator at lower speeds, which would reduce the SWL. Although fan 1 required more material than the commercial refrigerator fan, which had a cambered-plate design, the performance is significantly better.

# Chapter 9

# Conclusions and Future Work

This project set out to develop and validate a method to create axial flow fans with improved aerodynamic and aeroacoustic properties to meet the growing demand for quiet, high performance refrigerator fans. The method was then applied to develop a fan with superior performance than common commercial axial flow refrigerator fans. This section summaries the work performed and discusses future work.

## 9.1 Modelling and optimisation

The performance of axial flow fans was predicted using BEMT and the BPM aeroacoustic model. These models were implemented into a MOPSO which was used to generate optimal blade shapes with the objective of maximising the flow rate and minimising the SWL. The blades were successfully parameterised using B-splines and Bézier curves which allowed the optimisation algorithm to vary the blade shape, twist angle and chord angle.

The predicted values of flow rate proved to be successful with errors between 10-15% for all fans except the cambered-plate fan which had an error of 20%. The BPM model did not predict the SWL as accurately with under-predictions greater than 50% for all fans. The poor acoustic predictions are primarily attributed to IT noise being neglected in the modelling; however, the fans that were generated using shape optimisation also exploited the BPM model. The BPM model is based on empirical measurements of the symmetric NACA0012 aerofoil and does not predict noise from fans with cross-sections too dissimilar to the NACA0012 aerofoil. This excludes cambered or asymmetric aerofoil shaped blades which typically have superior performance to symmetric aerofoils.

Inclusion of the IT noise in the modelling greatly improved the acoustic prediction resulting in an error of about 13%. However, simple IT noise models do not consider geometric properties of the blade other than the rotational speed which makes them

unsuitable for rapid modelling. Future work of axial fan optimisation should utilise more computationally demanding IT noise models to gain better results. Alternatively, future work could utilise a similar model to this work and include the rotational speed as a variable since speed is one of the most critical factors in aeroacoustic noise. This would assist in finding an optimal fan operational point that meets prescribed performance requirements by varying simple variables such as speed, diameter and twist and chord distributions.

## 9.2 Experimental method

Modifications were made to an ISO10302 test rig to aid in noise source identification. The modifications utilised a long shaft with a cantilevered end to which fans were mounted. This successfully allowed the motor noise to be neglected because the motor could be enclosed in a soundproof enclosure. Additionally, cantilevering the shaft allowed for the supports behind the fan to be removed, which eliminated the possibility of fan support interaction noise.

The use of a long shaft with a moderate diameter allowed for a strain gauge to be fitted to the shaft with a telemetry system allowing for the direct measurement of the shaft torque. Measurement of the shaft torque provided a more accurate value of the shaft power, and hence, of the fan efficiency.

The modified test rig generated significantly more bearing and structure borne noise than expected, which required a soundproof enclosure to reduce the noise sufficiently below the noise generated by the fans. The modified test rig enclosure created turbulence, which resulted in additional IT noise. This problem, combined with the noise originating from vibrations of the chamber when rigidly connected to the fan or motor, suggests that a ducted method of testing fans would be better. Ducted methods allow for superior control over the turbulence through the use of bellmouths and turbulence control screens. Additionally, if the fan supports were required to be removed to test for fan-support interaction noise, a shaft could be run through the entire duct with supports at each end. This would reduce the need for a cantilevered shaft prone to dynamic excitation.

In the event that a similar test rig is constructed in the future, it would be beneficial to use a larger and stiffer shaft so that the fan could overhang the bearing by a sufficient distance that any enclosure is well removed from the fan inflow. Additionally, the enclosure would benefit from being a more aerodynamic shape as the sharp edges of the enclosure in this project probably exacerbated the turbulence present.

The torque measurements proved to be problematic as the fans generated small values of torque which resulted in small strains because of the proportionally large shaft.

Additionally, the bearings provided a similar or sometimes higher torque than the fans did which resulted in very noisy data with some spurious measurements.

A potential issue with the ISO10302 test rig that was not investigated in this project is the noise caused by the outlet. The turbulent flow from the fan is ejected from the chamber through a rectangular outlet with sharp edges. This has the potential to generate broadband noise as the turbulence passes over the sharp edge. Additionally, if the chamber were to be placed in the location suggested by ISO10302, the outlet flow would be directed over a microphone. Although windscreens were present on all of the microphones, pressure variations in the outlet flow increased the measured SPL of the microphones in the flow. This measurement of pseudo-sound would give a false measurement of the SWL. This study used an alternative position of the test chamber compared to ISO10302 to prevent any flow being directed over the microphones.

## 9.3 Experimental results

This section summaries the experimental results, see Section 9.1 for comparisons between the experimental results and predicted results.

The noise source identification measurements showed a minor negative effect of high surface roughness on the fan noise. However, the differences of approximately 1 dBA were less than the experimental error of $\pm$ 1.5 dBA. Repetition of these measurements in an acoustic laboratory would allow for a higher precision method to be used which would identify if this small increase is an actual effect. The noise source identification measurements showed no significant trend that the fan supports were causing fan support noise.

Hot wire anemometer measurements were taken across the fan to describe the turbulence properties. It was found that the turbulence intensity was 10% and the axial integral length was 15 mm. The high turbulence levels combined with the noise spectra showed that the main noise source of the axial flow fans tested is IT noise.

| **Property** | **Specifications** | **Fan 1** | **Commercial fan** |
|---|---|---|---|
| Flow rate at 25 Pa ($m^3\,h^{-1}$) | >550 | 680 | 530 |
| Flow rate at 0 Pa ($m^3\,h^{-1}$) | >680 | 858 | 620 |
| Minimum stall pressure (Pa) | >40 | 35 | 30 |
| SWL at 550 $m^3\,h^{-1}$ and 1800 rpm (dBA) | <65 | 63 | 65 |

TABLE 9.1: Comparison of fan 1 to the project objectives and a commercial refrigerator fan.

## 9.4 Final remarks

Fan 1 was shown to have superior performance to the commercially available Wellington 200/28 axial flow fan used for comparison. Fan 1 had a NACA0012 cross-section and had a solidity of approximately 0.8. Table 9.1 compares fan 1 to the Wellington fan and the original performance specifications and shows that fan 1 had superior performance to the Wellington fan for all properties. Additionally, fan 1 significantly exceeded both the flow rate requirements and SWL requirements. Fan 1 did not meet the pressure requirements; however, the fan continued to operate reasonably well beyond stall and can generate pressures greater than 40 Pa with only a minor increase in noise.

Similarly high turbulence to that in this study could be expected in a refrigerator. Future work on axial flow refrigerator fans could investigate the benefit of forward swept blades and their potential reduction of turbulent noise. Additionally, other avenues of increasing performance, such as serrated trailing edges, could be investigated.

The drive for quieter refrigerator fans results in potential for development in the mature field of fan design. Although not emphasised throughout this work, the fans with aerofoil-shaped blades significantly outperformed cambered-plate fans. Although this result was expected, switching from a cambered-plate fan blade to an aerofoil fan blade would significantly increase fan performance, efficiency and reduce the noise. Is this increase in materials really not worth the relatively large performance gains?

# Appendix A

# Aeroacoustic Self-Noise Equations

Below are additional equations for the BPM model [17] described in Chapter 4.

## A.1 Turbulent boundary layer - trailing edge noise and separeted flow noise

The Strouhal definitions are

$$St_p = \frac{f\delta_p^\star}{U} St_s = \frac{f\delta_s^\star}{U}, \tag{A.1}$$

$$St_1 = 0.02Ma^{-0.6}, \tag{A.2}$$

and

$$St_2 = St_1 \times \begin{cases} 1 & a_\star < 1.33^\circ \\ 10^{0.0054(\alpha_\star - 1.33)^2} & 1.33^\circ \leq a_\star \leq 12.5^\circ \\ 4.72 & 12.5^\circ < a_\star. \end{cases} \tag{A.3}$$

The spectral shape functions are given by

$$A_{min}(a) = \begin{cases} \sqrt{67.552 - 886.788a^2} - 8.219 & a < 0.204 \\ -32.665a + 3.981 & 0.204 \leq a \leq 0.244 \\ -142.795a^3 + 103.656a^2 - 57.757a + 6.006 & 0.244 < a, \end{cases} \tag{A.4}$$

and

$$A_{max}(a) = \begin{cases} \sqrt{67.552 - 886.788a^2} - 8.219 & a < 0.13 \\ -15.901a + 1.098 & 0.13 \leq a \leq 0.321 \\ -4.669a^3 + 3.491a^2 - 16.699a + 1.149 & 0.321 < a, \end{cases} \tag{A.5}$$

where $a$ is the absolute value of the logarithm of the ratio of Strouhal number, $St = St_p$ or $St_s$, to the peak Strouhal number, $St_{peak} = St_1$ or $St_2$, and is given by

$$a = |\log\left(\frac{St}{St_{peak}}\right)| \tag{A.6}$$

and

$$a_0(Re) = \begin{cases} 0.57 & Re < 9.52 \times 10^4 \\ (-9.57 \times 10^{-13})(Re - 8.57 \times 10^5)^2 + 1.13 & 9.52 \times 10^4 \leq Re \leq 8.57 \times 10^5 \\ 0.13 & 8.57 \times 10^5 < Re. \end{cases} \tag{A.7}$$

An interpolation factor $A_R(a_0)$ is determined from

$$A_R(a_0) = \frac{-20 - A_{min}(a_0)}{A_{max}(a_0) - A_{min}(a_0)}, \tag{A.8}$$

where $A_{min}(a_0)$ and $A_{max}(a_0)$ are the $A_{min}$ and $A_{max}$ spectra evaluated at $a_0$. This allows for $A$ to be calculated as

$$A(a) = A_{min}(a) + A_R(a_0)[A_{max}(a_0) - A_{min}(a_0)]. \tag{A.9}$$

Similarly for $B$,

$$B_{min}(b) = \begin{cases} \sqrt{16.888 - 886.788b^2} - 4.109 & b < 0.13 \\ -83.607b + 8.138 & 0.13 \leq b \leq 0.145 \\ -817.810b^3 + 355.210b^2 - 135.024b + 10.619 & 0.145 < b, \end{cases} \tag{A.10}$$

and

$$B_{max}(b) = \begin{cases} \sqrt{16.888 - 886.788b^2} - 4.109 & b < 0.10 \\ -31.330b + 1.854 & 0.10 \leq b \leq 0.187 \\ -80.541b^3 + 44.174b^2 - 39.381b + 2.344 & 0.187 < b, \end{cases} \tag{A.11}$$

where

$$b = |\log\left(\frac{St_s}{St_2}\right)|, \tag{A.12}$$

and

$$b_0(Re) = \begin{cases} 0.30 & Re < 9.52 \times 10^4 \\ (-4.48 \times 10^{-13})(Re - 8.57 \times 10^5)^2 + 0.56 & 9.52 \times 10^4 \leq Re \leq 8.57 \times 10^5 \\ 0.56 & 8.57 \times 10^5 < Re. \end{cases} \tag{A.13}$$

An interpolation factor $B_R(b_0)$ is determined from

$$B_R(b_0) = \frac{-20 - B_{min}(b_0)}{B_{max}(b_0) - B_{min}(b_0)}, \tag{A.14}$$

$$K_1 = \begin{cases} -4.31\log(Re) + 156.3 & Re < 2.47 \times 10^5 \\ -9.0\log(Re) + 181.6 & 2.47 \times 10^5 \leq Re \leq 8.0 \times 10^5 \\ 128.5 & 8.0 \times 10^5 < Re, \end{cases} \tag{A.15}$$

and

$$\Delta K_1 = \begin{cases} \alpha_\star[1.43\log(R_{\delta_p^\star}) - 5.29] & R_{\delta_p^\star} \leq 5000 \\ 0 & 5000 < R_{\delta_p^\star}, \end{cases} \tag{A.16}$$

where $R_{\delta_p^\star}$ is the Reynolds number based on pressure-side displacement thickness.

$$K_2 = K_1 + \begin{cases} -1000 & a_\star < \gamma_0 - \gamma \\ \sqrt{\beta^2 - (\frac{\beta}{\gamma})^2(\alpha_\star - \gamma_0)^2} + \beta_0 & \gamma_0 - \gamma \leq a_\star \leq \gamma_0 + \gamma \\ -12 & \gamma_0 + \gamma < a_\star, \end{cases} \tag{A.17}$$

where

$$\gamma = 27.094Ma + 3.31, \tag{A.18}$$

$$\gamma_0 = 23.43Ma + 4.651, \tag{A.19}$$

$$\beta = 72.65Ma + 10.74, \tag{A.20}$$

and

$$\beta_0 = -34.19Ma - 13.82. \tag{A.21}$$

## A.2 Laminar boundary layer - vortex shedding noise

The Strouhal definitions are

$$St_1' = \begin{cases} 0.18 & Re \leq 1.3 \times 10^5 \\ 0.001756Re^0.3931 & 1.3 \times 10^5 < Re \leq 4.0 \times 10^5 \\ 0.28 & 4.0 \times 10^5 < Re, \end{cases} \tag{A.22}$$

and

$$St_{peak}' = St_1' \times 10^{0.04\alpha^\star}. \tag{A.23}$$

$G1$ defines the spectral shape in terms of the ratio of Strouhal number to its peak as

$$G_1(e) = \begin{cases} 39.8\log(e) - 11.12 & e \leq 0.5974 \\ 98.409\log(e) + 2.0 & 0.5974 < e \leq 0.8545 \\ -5.076 + \sqrt{2.484 - 506.25[\log(e)]^2} & 0.8545 < e \leq 1.17 \\ -98.409\log(e) + 2.0 & 1.17 < e \leq 1.674 \\ -39.8\log(e) - 11.12 & 1.674 < e, \end{cases} \tag{A.24}$$

where $e = \frac{St'}{St'_{peak}}$ and

$$G_2(d) = \begin{cases} 77.852\log(d) + 15.328 & d \leq 0.3237 \\ 65.188\log(d) + 9.125 & 0.3237 < d \leq 0.5689 \\ -114.052\sqrt{[\log(d)]^2} & 0.5689 < d \leq 1.7579 \\ -65.188\log(d) + 9.15 & 1.7579 < d \leq 3.0889 \\ -77.8552\log(d) + 15.328 & 3.0889 < d, \end{cases} \tag{A.25}$$

where $d = \frac{Re}{(Re)_0}$ and

$$(Re)_0 = \begin{cases} 10^{0.215\alpha_\star + 4.978} & \alpha_\star \leq 3.0 \\ 10^{0.120\alpha_\star + 5.263} & 3.0 < \alpha_\star, \end{cases} \tag{A.26}$$

and the angle dependant level for the shape curve is

$$G_3(\alpha_\star) = 171.04 - 3.03\alpha_\star. \tag{A.27}$$

## A.3 Trailing edge bluntness - vortex shedding noise

The Strouhal definitions are

$$St''' = \frac{fh}{U}, \tag{A.28}$$

and

$$St'''_{peak} = \begin{cases} \frac{0.212 - 0.0045\psi}{1 + 0.325\frac{h}{\delta^\star_{avg}}^{-1} - 0.0132\frac{h}{\delta^\star_{avg}}^{-2}} & 0.2 \leq \frac{h}{\delta^\star_{avg}} \\ 0.1\frac{h}{\delta^\star_{avg}} + 0.095 - 0.00243\psi & \frac{h}{\delta^\star_{avg}} < 0.2, \end{cases} \tag{A.29}$$

where $\psi$ is the angle between the sloping surfaces upstream of the training edge and

$$\delta^\star_{avg} = \frac{\delta^\star_p + \delta^\star_s}{2}. \tag{A.30}$$

The peak level of the spectrum is determined from

$$G_4(\delta^\star_{avg}) = \begin{cases} 17.5\log(\delta^\star_{avg}) + 157.5 - 1.114\psi & \delta^\star_{avg} \leq 5 \\ 169.7 - 1.111\psi & 5 < \delta^\star_{avg}, \end{cases} \tag{A.31}$$

and the shape of the spectrum is defined by

$$G_5(\delta^\star_{avg}, \psi, \frac{St'''}{St'''_{peak}}) = (G_5)_{\psi=0^\circ} + 0.0715\psi[(G_5)_{\psi=14^\circ} - (G_5)_{\psi=0^\circ}], \tag{A.32}$$

where

$$(G_5)_{\psi=14^\circ} = \begin{cases} m\eta + k & \eta < \eta_0 \\ 2.5\sqrt{1-(\frac{\eta}{\mu})^2} - 2.5 & \eta_0 \leq \eta < 0 \\ \sqrt{1.5625 - 11194.99\eta^2} - 1.25 & 0 \leq \eta < 0 \\ -155.543\eta + 4.375 & 0.03616 \leq \eta, \end{cases} \tag{A.33}$$

$$\eta = \log\Big(\frac{St'''}{St'''_{peak}}\Big), \tag{A.34}$$

$$\mu = \begin{cases} 0.1221 & \frac{h}{\delta^\star_{avg}} < 0.25 \\ -0.21755(\frac{h}{\delta^\star_{avg}}) & 0.25 \leq \frac{h}{\delta^\star_{avg}} < 0.62 \\ -0.0308(\frac{h}{\delta^\star_{avg}}) + 0.0596 & 0.62 \leq \frac{h}{\delta^\star_{avg}} < 1.15 \\ 0.0242 & 1.15 \leq \frac{h}{\delta^\star_{avg}}, \end{cases} \tag{A.35}$$

$$m = \begin{cases} 0 & \frac{h}{\delta^\star_{a}vg} < 0.02 \\ 68.724(\frac{h}{\delta^\star_{avg}}) - 1.35 & 0.02 \leq \frac{h}{\delta^\star_{avg}} < 0.5 \\ 308.475(\frac{h}{\delta^\star_{avg}}) - 121.23 & 0.5 \leq \frac{h}{\delta^\star_{avg}} < 0.62 \\ 224.811(\frac{h}{\delta^\star_{avg}}) - 69.35 & 0.62 \leq \frac{h}{\delta^\star_{avg}} < 1.15 \\ 1583.28(\frac{h}{\delta^\star_{avg}}) - 1631.59 & 1.15 \leq \frac{h}{\delta^\star_{avg}} < 1.2 \\ 268.344 & 1.2 \leq \frac{h}{\delta^\star_{avg}}, \end{cases} \tag{A.36}$$

$$\eta_0 = -\sqrt{\frac{m^2\mu^4}{6.25 + m^2\mu^2}}, \tag{A.37}$$

and

$$k = 2.5\sqrt{1-\Big(\frac{\eta_0}{\mu}\Big)^2} - 2.5 - m\eta_0. \tag{A.38}$$

The spectrum $(G_5)_{\psi=0^\circ}$ is obtained by computing equations A.33 through to A.38 but replacing $(\frac{h}{\delta^\star_{avg}})$ by $(\frac{h}{\delta^\star_{avg}})'$ where

$$\Big(\frac{h}{\delta^\star_{avg}}\Big)' = 6.724\Big(\frac{h}{\delta^\star_{avg}}\Big)^2 - 4.019\Big(\frac{h}{\delta^\star_{avg}}\Big) + 1.107. \tag{A.39}$$

# Appendix B

# Sound Power Level of the Enclosed Test Rig

The SWL of the enclosed test rig was measured and used to correct the measurements of fans. The SWL of the test rig is presented below in Table B.1.

| Frequency Band (Hz) | SWL at 1200 rpm | SWL at 1500 rpm | SWL at 1800 rpm | SWL at 2100 rpm |
|---|---|---|---|---|
| 100 | 60.94 | 56.29 | 71.06 | 60.39 |
| 125 | 55.50 | 49.01 | 58.68 | 58.19 |
| 160 | 43.94 | 46.32 | 51.24 | 47.88 |
| 200 | 41.64 | 43.39 | 48.2 | 51.01 |
| 250 | 38.60 | 39.94 | 44.45 | 50.83 |
| 315 | 35.86 | 36.86 | 41.3 | 43.19 |
| 400 | 40.85 | 42.09 | 48.73 | 49.81 |
| 500 | 42.38 | 45.85 | 47.24 | 50.15 |
| 630 | 41.46 | 43.61 | 44.60 | 48.31 |
| 800 | 37.19 | 38.67 | 43.17 | 43.36 |
| 1000 | 42.42 | 46.77 | 48.79 | 58.56 |
| 1250 | 42.06 | 40.17 | 45.62 | 47.79 |
| 1600 | 38.45 | 45.09 | 41.00 | 42.92 |
| 2000 | 38.29 | 39.68 | 48.01 | 45.29 |
| 2500 | 43.31 | 42.96 | 44.08 | 52.45 |
| 3150 | 41.30 | 41.19 | 42.67 | 43.63 |
| 4000 | 36.55 | 39.33 | 41.58 | 42.65 |
| 5000 | 34.30 | 36.90 | 39.98 | 42.16 |
| 6300 | 28.06 | 30.82 | 34.13 | 37.08 |
| 8000 | 22.70 | 23.97 | 26.85 | 29.79 |
| 10000 | 20.43 | 21.45 | 22.99 | 25.76 |

TABLE B.1: SWL (dB) of the fan test rig at the four operational speeds. These values were used for correcting the measured fan values.

# References


[1] M. J. Lighthill, "On Sound Generated Aerodynamically 1. General Theory", *Proc. R. Soc. Lond. A, Math. Phys. Sci.*, vol. 211, no. 1107, pp. 564–587, Mar. 1952.

[2] M. De Gennaro and H. Kuehnelt, "Broadband Noise Modelling and Prediction for Axial Fans", in *Proc. Int. Con. on Fan Noise, Tech., & Num. Meth.*, Senlis, France, 2012.

[3] S. S. Rodrigues, "Aeroacoustic Optimization of Wind Turbine Blades", Master's thesis, Aerospace Engineering Dept., Instituto Superior Técnico, Lisbon, Portugal, 2012.

[4] M. J. Lighthill, "On Sound Generated Aerodynamically 2. Turbulence as a Source of Sound", *Proc. R. Soc. Lond. A, Math. Phys. Sci.*, vol. 222, no. 1148, pp. 1–32, Feb. 1954.

[5] N. Curle, "The Influence of Solid Boundaries Upon Aerodynamic Sound", *Proc. R. Soc. Lond. A, Math. Phys. Sci.*, vol. 231, no. 1187, pp. 505–514, Sep. 1955.

[6] M. V. Lowson, "The Sound Field for Singularities in Motion", *Proc. R. Soc. Lond. A, Math. Phys. Sci.*, vol. 286, no. 1407, pp. 559–572, Aug. 1965.

[7] J. E. Ffowcs Williams and D. L. Hawkings, "Sound Generation by Turbulence and Surfaces in Arbitrary Motion", *Philos. Trans. R. Soc. Lond. A, Math. Phys. Sci.*, vol. 264, no. 1151, pp. 321–342, May 1969. DOI: 10.1098/rsta.1969.0031.

[8] I. J. Sharland, "Sources of Noise in Axial Flow Fans", *J. Sound Vib.*, vol. 1, no. 3, pp. 302–322, Jul. 1964. DOI: 10.1016/0022-460x(64)90068-9.

[9] B. B. Daly, *Woods Practical Guide to Fan Engineering*, 3rd ed. Colchester: Woods of Colchester ltd., 1978.

[10] L. Gutin, "Uber das Schallfeld einer rotierenden Luftschraube [On the Sound Field of a Rotating Propeller]", trans. by . NACA Technical Memorandum No. 1995, *Physikalische Zeitschrift der Sowjetunion*, vol. 9, no. 1, pp. 57–71, 1936.

[11] B. D. Mugridge and C. L. Morfey, "Sources of Noise in Axial-Flow Fans", *J. Acoust. Soc. Am.*, vol. 51, no. 5, pp. 1411–1426, May 1972. DOI: 10.1121/1.1912992.

[12] R. E. Longhouse, "Control of Tip-Vortex Noise of Axial-Flow Fans by Rotating Shrouds", *J. Sound Vib.*, vol. 58, no. 2, pp. 201–214, May 1978. DOI: 10.1016/S0022-460x(78)80075-3.

[13] T. Fukano and C. M. Jang, "Tip clearance noise of axial flow fans operating at design and off-design condition", *J. Sound Vib.*, vol. 275, no. 3-5, pp. 1027–1050, Aug. 2004. DOI: 10.1016/S0022-460x(03)00815-0.

[14] R. E. Longhouse, "Vortex Shedding Noise of Low Tip Speed, Axial-Flow Fans", *J. Sound Vib.*, vol. 53, no. 1, pp. 25–46, Jul. 1977. DOI: 10.1016/0022-460x(77)90092-X.

[15] J. E. Ffowcs Williams and L. H. Hall, "Aerodynamic Sound Generation by Turbulent Flow in the Vicinity of a Scattering Half Plane", *J. Fluid Mech.*, vol. 40, no. 4, pp. 657–670, Mar. 1970.

[16] T. F. Brooks and T. H. Hodgson, "Trailing Edge Noise Prediction from Measured Surface Pressures", *J. Sound Vib.*, vol. 78, no. 1, pp. 69–117, Sep. 1981. DOI: 10.1016/S0022-460x(81)80158-7.

[17] T. F. Brooks, D. S. Pope, and M. A. Marcolini, "Airfoil self-noise and prediction", *NASA Reference Publication*, no. 1218, Jul. 1989.

[18] M. J. Lighthill, "Sound Generated Aerodynamically", *Proc. R. Soc. Lond. A, Math. Phys. Sci.*, vol. 267, no. 1329, pp. 147–182, May 1962. DOI: 10.1098/rspa.1962.0090.

[19] T. Wright and W. E. Simmons, "Blade Sweep for Low-Speed Axial Fans", *J. Turbomachinery*, vol. 112, pp. 151–158, Jun. 1990. DOI: 10.1115/89-GT-53.

[20] T. Fukano, Y. Kodama, and Y. Takamatsu, "Noise Generated by Low Pressure Axial Flow Fans, III: Effects of Rotational Frequency, Blade Thickness and Outer Blade Profile", *J. Sound Vib.*, vol. 56, no. 2, pp. 261–277, Jan. 1978.

[21] J. M. Fitzgerald and G. C. Lauchle, "Reduction of Discrete Frequency Noise in Small, Subsonic Axial-Flow Fans", *J. Acoust. Soc. Am.*, vol. 76, no. 1, pp. 158–166, Jul. 1984. DOI: 10.1121/1.391112.

[22] M. S. Howe, "Aerodynamic Noise of a Serrated Trailing Edge", *J. Fluids Struct.*, vol. 5, no. 1, pp. 33–45, Jan. 1991. DOI: 10.1016/0889-9746(91)80010-B.

[23] ——, "Noise Produced by a Sawtooth Trailing Edge", *J. Acoust. Soc. Am.*, vol. 90, no. 1, pp. 482–487, Jul. 1991. DOI: 10.1121/1.401273.

[24] A. Cattanei, R. Ghio, and A. Bongiovi, "Reduction of the tonal noise annoyance of axial flow fans by means of optimal blade spacing", *Appl. Acoust.*, vol. 68, no. 11-12, pp. 1323–1345, Nov. 2007. DOI: 10.1016/j.apacoust.2006.07.012.

[25] R. C. Mellin and G. Sovran, "Controlling Tonal Characteristics of Aerodynamic Noise Generated by Fan Rotors", *Journal of Basic Engineering*, vol. 92, no. 1, pp. 143–154, Mar. 1970.

[26] T. Fukano, Y. Takamatsu, and Y. Kodama, "The Effects of Tip Clearance on the Noise of Low-Pressure Axial and Mixed Flow Fans", *J. Sound Vib.*, vol. 105, no. 2, pp. 291–308, Mar. 1986. DOI: 10.1016/0022-460x(86)90158-6.

[27] L. X. Huang, "Characterizing computer cooling fan noise", *J. Acoust. Soc. Am.*, vol. 114, no. 6, pp. 3189–3200, Dec. 2003. DOI: 10.1121/1.1624074.

[28] A. Oyama, M. S. Liou, and S. Obayashi, "Transonic Axial-Flow Blade Optimization: Evolutionary Algorithms/Three-Dimensional Navier-Stokes Solver", *AIAA J. Prop. Power*, vol. 20, no. 4, pp. 612–619, Jul. 2004.

[29] J. G. Leishman, *Principles of helicopter aerodynamics*, 2nd, ser. Cambridge aerospace series 18. New York: CUP, 2006.

[30] W. Johnson, *Helicopter theory*. Princeton: PUP, 1980.

[31] P. Moriarty and A. C Hansen, "AeroDyn Theory Manual", NREL, Golden, CO, TP 500-36881, Jan. 2005.

[32] W. J. M. Rankine, "On the Mechanical Principles of the Action of Propellers", *Trans. Inst. Naval Architects*, vol. 6, pp. 90–98, 1865.

[33] H. Glauert, "Airplane Propellers", in *Aerodynamic Theory*, W. F. Durand, Ed., Berlin, Germany: Springer Berlin Heidelberg, 1935, pp. 169–360.

[34] S. Goldstein, "On the Vortex Theory of Screw Propellers", *Proc. R. Soc. Lon.*, vol. 123, no. 792, pp. 29–38, Apr. 1929.

[35] H. V. Borst, "A New Blade Element Method for Calculating the Performance of High and Intermediate Solidity Axial Flow Fans", NASA, Mountain View, CA, Contractor Rep. 3063, 1978.

[36] M. Drela, "Xfoil: An Analysis and Design System for Low Reynolds Number Airfoils", in *Low Reynolds Number Aerodynamics*, ser. Lecture Notes in Engineering, T. Mueller, Ed., vol. 54, Berlin, Germany: Springer Berlin Heidelberg, 1989, pp. 1–12. DOI: 10.1007/978-3-642-84010-4_1.

[37] M. Drela and M. B. Giless, "Viscous-Inviscid Analysis of Transonic and Low Reynolds Number Airfoils", *AIAA*, vol. 25, no. 10, pp. 1347–1355, Oct. 1987.

[38] "Theoretical and Experimental Power From Large Horizontal-Axis Wind Turbines", Tech. Rep.

[39] W. Timmer, "Aerodynamic characteristics of wind turbine blade airfoils at high angles-of-attack", TORQUE2010, Crete, Greece, 2010.

[40] M. Lowson and S. Fiddes, "Assessment and prediction of wind turbine noise", Flow Solutions Ltd., Bristol, UK, Report ETSU-W – 13/00284/REP, 1993, pp. 1–46.

[41] *Numerical Prediction of the Aeroacoustic Sound Sources in a Low Pressure Axial Fan with Inflow Distortion*, Fan Noise, Lyon, France, 2007.

[42] C. K. W. Tam, "Computational Aeroacoustics: An Overview of Computational Challenges and Applications", *Int. J. Comput. Fluid Dyn.*, vol. 18, no. 6, pp. 547–567, Aug. 2004.

[43] E. Envia, A. G. Wilson, and D. L. Huff, "Fan Noise: A Challenge to CAA", *Int. J. Comput. Fluid Dyn.*, vol. 18, no. 6, pp. 471–480, Aug. 2008.

[44] T. Carolus, M. Schneider, and H. Reese, "Axial flow fan broad-band noise and prediction", *J. Sound Vib.*, vol. 300, no. 1, pp. 50–70, Feb. 2007.

[45] R. K. Amiet, "Acoustic Radiation From an Airfoil In a Turbulent Stream", *J. Sound Vib.*, vol. 41, no. 4, pp. 407–420, Aug. 1975.

[46] L. Yang, D. Z. Hui, and O. Hua, "Optimization Design and Experimental Study of Low-Pressure Axial Fan with Forward-Skewed Blades", *Int. J. Rotary Machinery*, vol. 2007, pp. 1–10, Aug. 2007. DOI: 10.115/2007/85275.

[47] E. N. Jacobs, K. E. Ward, and R. M. Pinkerton, "The characteristics of 78 related airfoil sections from tests in the variable-density wind tunnel", NACA, Washington DC, Rep 460, 1933.

[48] H. Sobieczky, "Parametric Airfoils and Wings", in *Notes on Numerical Fluid Mechanics*, G. S. Fujii K.and Dulkikravich, Ed., vol. 68, Vieweg, 1998, pp. 71–88.

[49] U. K. Wickramasinghe, R. Carrese, and X. Li, "Designing Airfoils using a Reference Point based Evolutionary Many-objective Particle Swarm Optimization Algorithm", IEEE CEC, Barcelona, Spain, 2010.

[50] W. Song and A. Keane, "A Study of Shape Parameterisation Methods for Airfoil Optimisation", in *Proc. 10th AIAA/ISSMO Multi-Discip. Analysis and Optimization Conf.*, ser. Multidisciplinary Analysis Optimization Conferences, Albany, NY: American Institute of Aeronautics and Astronautics, 2004. DOI: 10.2514/6.2004-4482.

[51] P. V. Gamboa and M. A. R. Silvestre, "Airfoil optimization with transition curve as objective function", VI Int. Conf. on Adaptive Modeling & Simulation, Lisbon, Portugal, 2013.

[52] K.-H. Brakhage, "Spline techniques for generating airplane wings with practical applications", 13th ICGG, Dresden, Germany, 2008.

[53] M. Drela, "Pros and Cons of airfoil optimization", in *Frontiers of Computational Fluid Dynamics*, D. A. H. Caughey M. M.; Ed., Singapore: World Scientific Publishing Co., 1998, pp. 363–381.

[54] L. A. Piegl and W. Tiller, *The NURBS book*, 2 ed. New York: Springer, 1997.

[55] C. De Boor, *A Practical Guide to Splines*, rev. ed., ser. Applied mathematical sciences. Berlin: Springer, 2001.

[56] A. Pelletier and T. J. Mueller, "Low Reynolds Number Aerodynamics of Low-Axpect-Ratio, Thin/Flat/Cambered-Plate Wings", *J. Air.*, vol. 37, no. 5, pp. 825–832, Sep. 2000.

[57] M. R. Reid, "Thin/Cambered/Reflexed Airfoil Development for Micro-Air Vehicles at Reynolds Numbers of 60,000 to 150,000", Master's thesis, Mech. Eng. Dept. RIT, Rochester, NY, 2006.

[58] E.-G. Talbi, *Metaheuristics: FROM Design to Implementation*. Hoboken, NJ: Wiley, 2009.

[59] R. Hassan, B. Cohanim, and O. de Weck, "A comparison of particle swarm optimization and the genetic algorithm", Proc. 1st AIAA Multidisciplinary Design Optimization Specialist Conf, Austin, TX, 2005.

[60] E. Elbeltagi, T. Hegazy, and D. Grierson, "Comparison among five evolutionary-based optimization algorithms", *Advanced Engineering Infomatics*, vol. 19, no. 1, pp. 43–53, Jan. 2005.

[61] J. Kennedy and R. Eberhart, "Particle Swarm Optimisation", in *IEEE Int. Conf. on Neural Networks*, Perth, Australia: IEEE, 1995. DOI: 10.1109/ICNN.1995.488968.

[62] J. C. Bansal, P. K. Singh, M. Saraswat, A. Verma, S. S. Jadon, and A. Abraham, "Inertia Weight Strategies on Particle Swarm Optimization", in *3rd World Congr. NaBIC*, Salamanca, Spain: IEEE, 2011. DOI: 10.1109NaBIC.2011.6089659.

[63] G. Yue-lin, A. Xiao-hui, and L. Jun-min, "A Particle Swarm Optimization Algorithm with Logarithm Decreasing Inertia Weight and Chaos Mutation", in *Int. Conf. CIS*, Suzhou, China: Int. Conf. CIS, 2008, pp. 61–65. DOI: 10.1109/CIS.2008.183.

[64] M. Reyes-Sierra and C. A. Coello Coello, "Multi-objective Particle Swarm Optimizers: A Survey of the State-of-the-Art", *Int. J. Computational Intelligence Research*, vol. 2, no. 3, pp. 287–308, Mar. 2006.

[65] C. A. Coello Coello, G. T. Pulido, and M. S. Lechuga, "Handling Multiple Objectives With Particle Swarm Optimization", *IEEE Trans. Evol. Comput.*, vol. 8, no. 3, pp. 256–279, Jun. 2004.

[66] R. C. Eberhart and Y. Shi, "Comparing Inertia Weights and Constriction Factors in Particle Swarm Optimization", in *Proc. 2000 Congr. Evolutionary Computation*, La Jolla, CA, 2000, pp. 84–88.

[67] K. Deb, A. Pratap, and S. Moitra, "Mechanical Component Design for Multiple Objectives Using Elitist Non-dominated Sorting GA", in *Proc. PPSN*, Paris, France, 2000.

[68] R. McKinlay, "An Investigation into the Performance of Axial Flow Refrigerator Fans", Master's thesis, Dept. Mech. Eng, UC, Christchurch, NZ, 2014.

[69] "Acoustics – measurement of airborne noise emitted and structure-borne vibration induced by small air-moving devices – part 1: Airborne noise measurement", International Organization for Standardization, ISO 10302-1:2011, Jan. 2011.

[70] "Acoustics – determination of sound power levels of noise sources using sound pressure – Engineering method in an essentially free field over a reflecting plane", International Organization for Standardization, ISO 3744:1994, May 1994.

[71] "Acoustics – requirements for the performance and calibration of reference sound sources used for the determination of sound power levels", International Organization for Standardization, ISO 6946:1999, Dec. 1999.

[72] T. R. Camp and H. W. Shin, "Turbulence Intensity and Length Scale Measurements in Multistage Compressors", *J. Turbomach*, vol. 117, no. 1, pp. 38–46, Jan. 1995. DOI: 10.1115/1.2835642.